DI-JET CROSS SECTION AND DOUBLE SPIN ASYMMETRY AT MID-RAPIDITY FROM POLARIZED P+P COLLISIONS AT $\sqrt{s} = 200$ GEV AT RHIC

Brian S. Page

Submitted to the faculty of the University Graduate School
in partial fulfillment of the requirements for the degree
Doctor of Philosophy
in the Department of Physics,
Indiana University
December 2013

Accepted by the Graduate Faculty, Indiana University, in partial fulfillment of the requirements of the degree of Doctor of Philosophy.

Doctoral Committee	Scott W. Wissink(Chair)
	Anselm Vossen
	J. Timothy Londergan
December 5, 2013	W. Michael Snow

Acknowledgements

The work presented in this dissertation is the culmination of seven years of effort and would not have been possible without the help and support of many people. To my adviser, Scott Wissink, thank you for your insight and guidance, and for showing me what it means to be an experimental physicist. To Will Jacobs, thank you for teaching me the nuts and bolts of detector operation and for giving me someone to vent to when the need arose. To Anselm Vossen, thank you for your many thoughtful questions and observations. I must also thank Jim Sowinski for being an excellent adviser during the first stage of my graduate career. I would also like to acknowledge Mike Snow and Timothy Londergan for serving on my dissertation committee.

The STAR jet-finding group played an especially large role in the success of this analysis and I would like to thank Pibero Djawotho, Renee Fatemi, Carl Gagliardi, Steven Trentalange, and all the other members of the group. This would not have been possible without your help and it was an honor and pleasure to work with all of you. I would also like to thank the remaining members of the IU STAR group both past and present: Jan Balewski, Seema Dhamija, Ilya Selyuzhenkov, Justin Stevens, Mike Skoby, and Emily Zarndt. Thank you all for your support.

To my parents, thank you for showing me the values of hard work and perseverance which were so necessary for the completion of this task. Finally, to my wife Evelyn, thank you for your love and support throughout this process, and over the last 10 years. You have made this journey so much more enjoyable and I don't know what I would do without you.

Brian S. Page

DI-JET CROSS SECTION AND DOUBLE SPIN ASYMMETRY AT MID-RAPIDITY FROM POLARIZED P+P COLLISIONS AT $\sqrt{s} = 200$ GEV AT RHIC

Spin, like mass and electric charge, is a fundamental property of all particles. The spin of composite particles such as the proton must be generated from the intrinsic spins and orbital motions of its constituents, and the question of how the quarks and gluons inside the proton contribute to its total spin remains one of the most important unresolved questions in nuclear physics. While the contribution from the quark spins is well known, the gluon and angular momentum components are poorly constrained. Measurements of di-jet asymmetries arising from longitudinally polarized proton-proton collisions at the Relativistic Heavy Ion Collider (RHIC) offer a unique way to probe the intrinsic gluon spin contribution to the spin of the proton.

The measurements of the di-jet cross section, as well as the longitudinal double-spin asymmetry, A_{LL}, are presented. The cross section and A_{LL} results are based on 17.1 pb^{-1} and 19.5 pb^{-1}, respectively, of data taken by the STAR detector during the 2009 proton-proton run at $\sqrt{s} = 200$ GeV. The measured cross section is in good agreement with perturbative QCD theoretical predictions using the CTEQ6M parton distribution functions and the A_{LL} is consistent with previous inclusive jet results obtained from the 2009 data.

Scott W. Wissink

Anselm Vossen

J. Timothy Londergan

W. Michael Snow

Contents

List of Figures

List of Tables

Chapter 1

Introduction and Theoretical Motivation

In 1917, Ernst Rutherford performed a series of experiments in which he passed an alpha particle beam through nitrogen gas and observed the creation of hydrogen. The only way this would be possible was if the hydrogen nucleus was already present in the nuclei of other elements. With the realization that the hydrogen nucleus was a fundamental building block for all heavier nuclei, Rutherford gave it a new name: the proton.

In the near century since its discovery, the proton has been the subject of intense experimental and theoretical scrutiny. This work has culminated in the discovery of the basic constituents of all observed hadrons, the quarks and gluons, as well as the theory which describes their dynamics, Quantum Chromodynamics (QCD). Despite these successes, our knowledge of the inner structure of the proton remains incomplete. One particularly vexing issue is the question of how the constituents of the proton contribute to its spin. The measurements described below are designed to shed light on what role the intrinsic spin of the gluon plays in this puzzle.

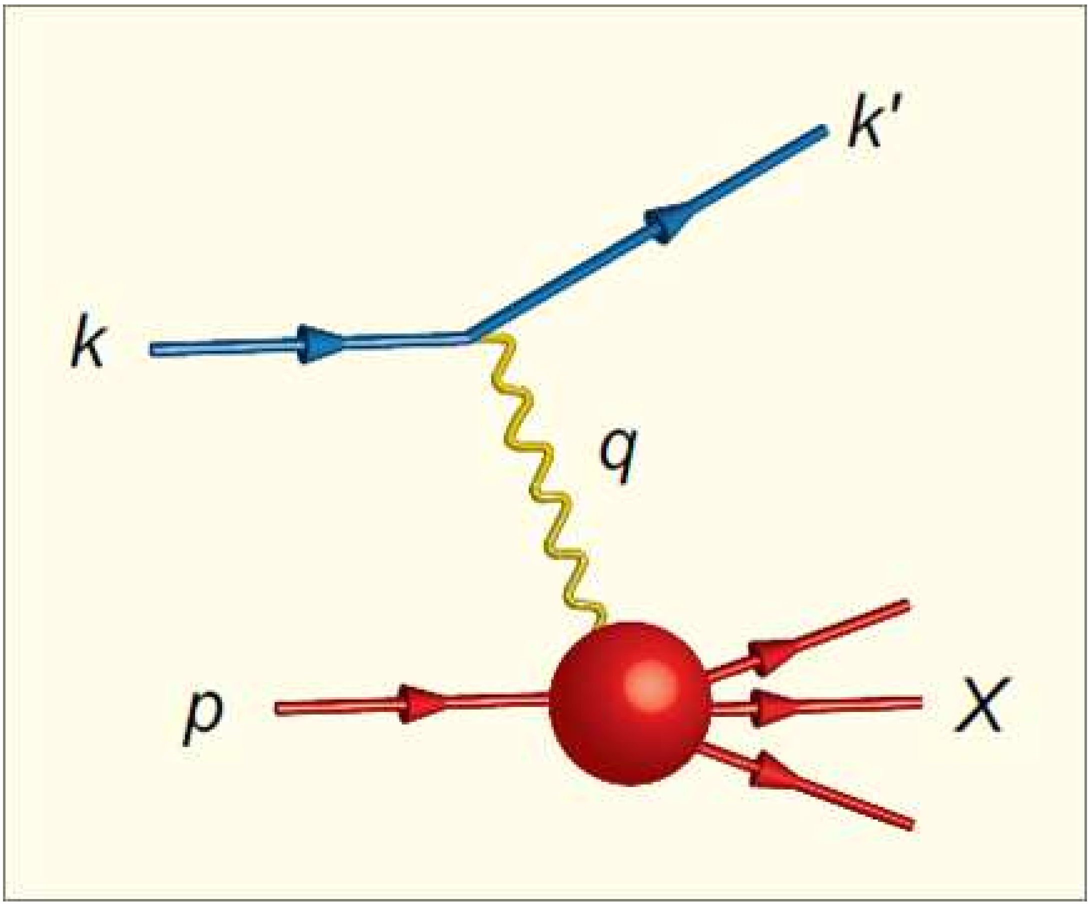

Figure 1.1: Schematic of the Deep Inelastic Scattering process, in which a lepton exchanges a virtual photon with a quark, leading to the breakup of the parent proton.

1.1 Deep Inelastic Scattering and Proton Structure

Before discussing the question of how the proton's constituents contribute to its spin, it will be useful to give a brief overview of what those constituents are, and the processes studied to learn about them. Most of our knowledge about the internal structure of the proton comes from lepton scattering. Early experiments focused on elastic scattering with electrons, in which the electron transferred a small amount of momentum to the proton and the proton stayed intact. These measurements gave information about bulk properties of the proton, such as its charge radius, but details on the small-scale structure of the proton would only come with studies of the Deep Inelastic Scattering (DIS) process (see figure 1.1). Overviews of DIS can be found in most particle physics text books and the discussion below closely follows [1] and [2]. A good historical overview can be found in [3], [4], and [5].

DIS refers to lepton nucleon scattering in which the lepton transfers a large amount of momentum (the momentum transferred is denoted as Q^2) to the nucleon, and the nucleon breaks into a number of hadrons whose combined mass is large compared to the nucleon mass. The DIS cross section can be written as shown in equation 1.1, where Ω is a phase space term, α is the fine structure constant, E' is the energy of the scattered lepton, θ is the lepton scattering angle, and W_1 and W_2 are the inelastic structure functions. The structure functions associated with elastic scattering (and thus the elastic cross section) were found to drop rapidly with Q^2 [[6]]. On the other hand, the inelastic structure functions were seen to be mostly independent of Q^2 [[4], [7]] which is a feature of point-like interactions, indicating that the proton had a granular substructure.

$$\frac{\mathrm{d}^2\sigma}{\mathrm{d}\Omega\mathrm{d}E'} = \frac{4\alpha^2(E')^2}{Q^4}\left(2W_1\sin^2\frac{\theta}{2} + W_2\cos^2\frac{\theta}{2}\right) \tag{1.1}$$

The structure functions $W_{1,2}$ are nominally functions of two variables, x (or ν) and Q^2, where $x = Q^2/2M\nu$ and $\nu = E - E'$. The observation that the structure functions depend strongly on only one variable, x, instead of two, is known as Bjorken scaling after, James Bjorken who predicted this behavior while studying the structure functions in the limit where $Q^2 \to \infty$ and $\nu \to \infty$ while x remains fixed [[8]]. In the so-called Bjorken limit, the inelastic structure functions can be written as:

$$MW_1(\nu, Q^2) = F_1(x) \tag{1.2a}$$

$$\nu W_2(\nu, Q^2) = F_2(x) \tag{1.2b}$$

Shortly after the observation that the inelastic structure functions had the scaling behavior predicted by Bjorken, indicating the existence of point-like constituents inside the proton, Feynman developed the parton model to describe the DIS observations [9]. The parton model represents the DIS cross section as the incoherent sum of elastic lepton scattering off of a number of effectively free constituents dubbed partons. One aspect of the parton model is the introduction of parton distribution functions, $f_j(x)$, which are the probabilities of finding a parton of type j within the proton carrying a fraction x of the proton's momentum. The inelastic structure functions can then be written in terms of the parton distribution functions (where the Q_j are the electric charges of the partons):

$$F_1(x) = \frac{1}{2}\sum_j Q_j^2 f_j(x) \tag{1.3a}$$

$$F_2(x) = x\sum_j Q_j^2 f_j(x) \tag{1.3b}$$

One immediate consequence of these equations is the Callan-Gross relation, equation 1.4, which will hold for partons with spins of one half. The consistency of the DIS data with the Callan-Gross relation lent credence to the idea that the partons of Feynman's model were in fact objects known as quarks, which Gell-Mann and Zweig had proposed several years prior to explain the preponderance of observed hadrons [[10], [11]]. Further study of the DIS structure functions implied the presence of anti-quarks at low values of x. Eventually, it was determined that the quarks and anti-quarks contributed roughly 50% of the total momentum of the proton [2]. This implied the existence of a new neutral particle which was taken to be the gluon [12].

$$F_2(x) = 2xF_1(x) \tag{1.4}$$

The work outlined above led to a model for the inner structure of the nucleon known as the quark-parton model. It described a proton in which three so-called valence quarks (uud) dominated the structure at large values of x and gave the proton its SU(3) properties. Proton structure at lower values of x was dominated by quark-antiquark pairs (known as the sea) and gluons, which carried roughly 50% of the total proton momentum. The intense experimental and theoretical work based on the quark-parton model, combined with the earlier successes of QED to classical electromagnetic processes, led to the development of QCD as the theory which describes in detail the Strong Force which mediates the interaction between quarks and gluons. One consequence of QCD which will be of importance is that it predicts a slight violation of Bjorken scaling. That is, the inelastic structure functions should have a small (logarithmic) dependence on Q^2 which is due to the influence of the gluons. The scaling violation effects are small, and thus data over a wide range of Q^2 and x need to be collected to observe it; but by studying these violations, information about the gluon distribution functions can be gained from DIS measurements, despite the fact that leptons do not probe the gluon directly.

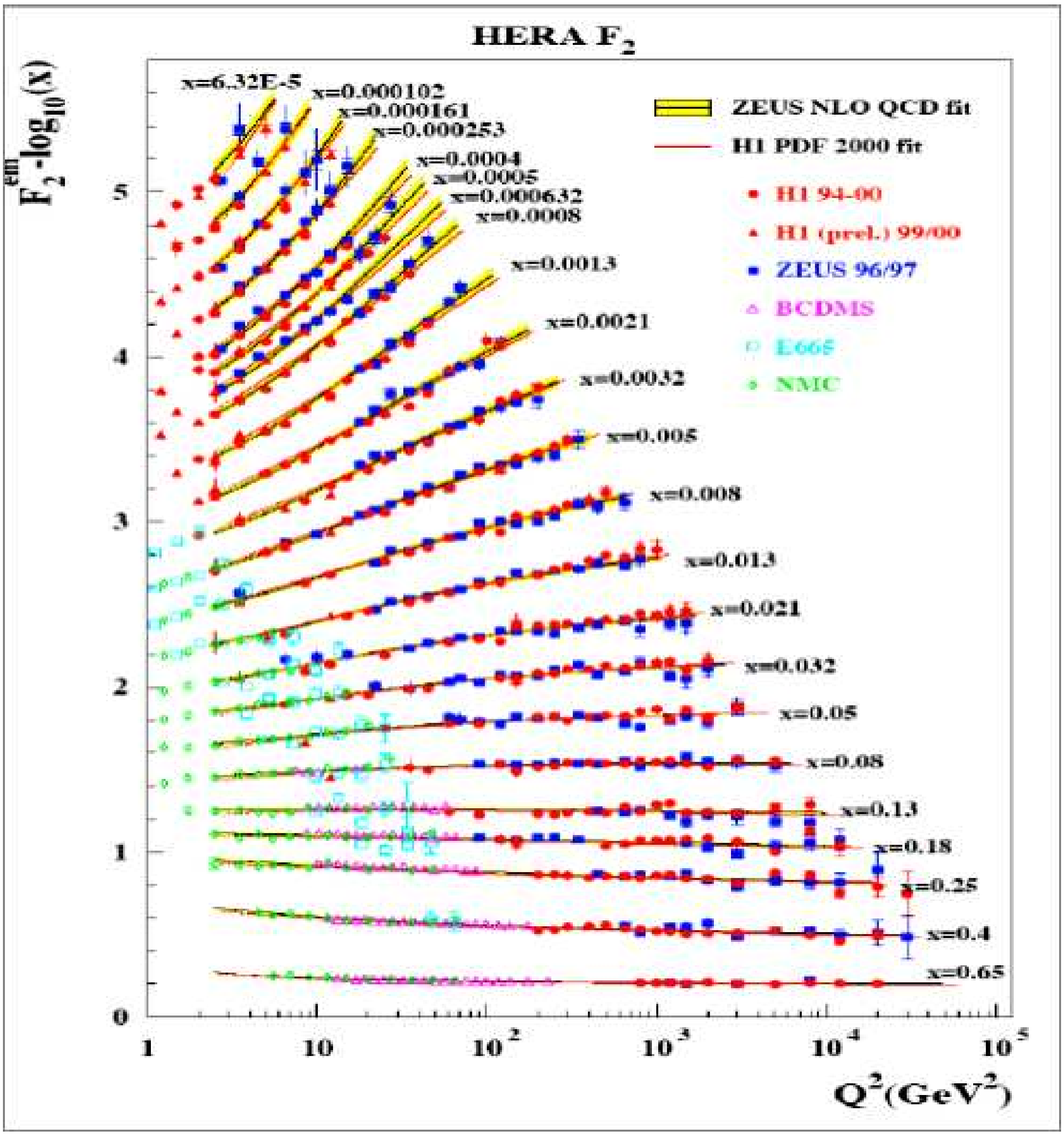

Figure 1.2: This figure shows the world's data on the F_2 structure function as a function of Q^2 for a wide range of fixed x values [13].

1.1.1 Helicity Structure and the Spin Crisis

The previous section gave a brief overview of the crucial role that DIS played in our understanding of the internal structure of the proton. Despite this, one important property has not been taken into account: spin. The formalism of the previous section was derived under the assumption that the spins of the incoming and outgoing lepton, as well as that of the target, were all averaged over. The study of polarized DIS has lead to some startling discoveries, which will be briefly summarized below, as well as some subtle insights into QCD which are beyond the scope of this dissertation. Reviews of polarized

DIS experiments and theory can be found in [14], [15], [16], [17], and [18].

If one considers a beam of longitudinally polarized leptons and a longitudinally polarized proton target, the difference in DIS cross sections between cases when the beam and target spins are parallel and anti-parallel gives access to two new structure functions, $G_1(\nu, Q^2)$ and $G_2(\nu, Q^2)$, as in equation 1.5.

$$\frac{\mathrm{d}^2\sigma^A}{\mathrm{d}\Omega \mathrm{d}E'} - \frac{\mathrm{d}^2\sigma^P}{\mathrm{d}\Omega \mathrm{d}E'} = \frac{4\alpha^2 E'}{Q^2 E}\left[(E + E'\cos\theta)\, mG_1 - Q^2 G_2\right] \tag{1.5}$$

The term σ^A refers to the cross section obtained when the beam and target spins are anti-parallel and σ^P refers to the case when the spins are parallel. As with the unpolarized DIS structure functions W_1 and W_2, the polarized structure functions scale in the Bjorken limit, giving the terms $g_1(x)$ and $g_2(x)$ which depend solely on x. Analogously to the unpolarized structure function $F_1(x)$, $g_1(x)$ can be expressed in terms of polarized parton distribution functions $\Delta q(x)$ (equation 1.6). The term $\Delta q(x)$ is the probability of finding a given parton at a certain momentum which has its spin parallel to the spin of the proton, minus one with its spin anti-parallel to the spin of the proton, i.e., $\Delta q(x) \equiv q^P(x) - q^A(x)$. Interestingly, the $g_2(x)$ structure function does not have a simple interpretation in the parton model, but that discussion is outside the scope of this dissertation.

$$g_1(x) = \frac{1}{2}\sum_j e_j^2 \left[\Delta q_j(x) + \Delta \bar{q}_j(x)\right] \tag{1.6}$$

The form of equation 1.6 illustrates that the $g_1(x)$ structure function contains information on how much of the proton's spin is carried by the spins of its electrically charged constituents. In the late 1980s, the European Muon Collaboration (EMC) measured $g_1(x)$ in an x range between 0.01 and 0.7 [[19], [20]]. They determined the first moment of $g_1(x)$ to be 0.126, which implied that the quarks and anti-quarks inside the proton only carried about 20% of the spin of the proton, assuming an unpolarized strange quark contribution. The value of 0.126 was also incompatible with the value of 0.189 predicted by Jaffe and Ellis [[21]] based on flavor $SU(3)$ considerations and known hyperon beta-decay values. The small contribution from the quarks to the spin of the proton came as a surprise, because in the quark-parton model the spin of the proton is constructed from the vector sum of the spins of the three valence quarks (relativistic models put the quark contribution at roughly 60%, still far above the value implied by the EMC result). The small contribution of the quark spins to the proton spin, as well as the seeming incompatibility of the EMC result with the Jaffe-Ellis prediction, was termed the "Proton Spin Crisis" and precipitated major experimental and theoretical efforts.

In the 1990s, Jaffe and Monahar [[22]]showed that the spin of the proton could be decomposed into contributions from the intrinsic spins of the quarks and gluons and the orbital angular momenta of both, as shown in equation 1.7.

$$\langle S_P \rangle = \frac{1}{2} = \frac{1}{2}\Delta\Sigma + \Delta G + L_q + L_g \tag{1.7}$$

Here $\Delta\Sigma \equiv \int \big(\Delta u(x) + \Delta\bar{u}(x) + \Delta d(x) + \Delta\bar{d}(x) + \Delta s(x) + \Delta\bar{s}(x)\big)$ is the contribution from the spins of the quarks, $\Delta G = \int_0^1 \Delta g(x, Q^2)\mathrm{d}x$ is that due to the spins of the gluons, and L_q and L_g are the orbital angular momenta of the quarks and gluons, respectively. At the present time, $\Delta\Sigma$ is quite well constrained from polarized DIS data, with a value of 0.366. Just as scaling violations of the F_2 structure function gave information about the unpolarized gluon distributions, scaling violations of g_1 can provide information about the polarized gluon distributions. Unfortunately, the world's data (figure 1.3) on g_1 from polarized DIS experiments does not cover a large enough range in Q^2 to place a significant constraint on ΔG [23]. The need for more precise data on $\Delta g(x)$ was one of the primary motivations for the polarized *pp* program at RHIC.

1.2 Gluon Polarization Studies at RHIC

The study of the spin-dependent structure of the proton at RHIC includes several independent programs. These include investigations of the proton's transverse spin structure, the polarized parton distribution functions of the sea quarks via $W^{+/-}$ production, and the contribution of the gluon spin to the total spin of the proton. This dissertation will only deal with the last issue, but an overview of the complete spin program at RHIC can be found here [24].

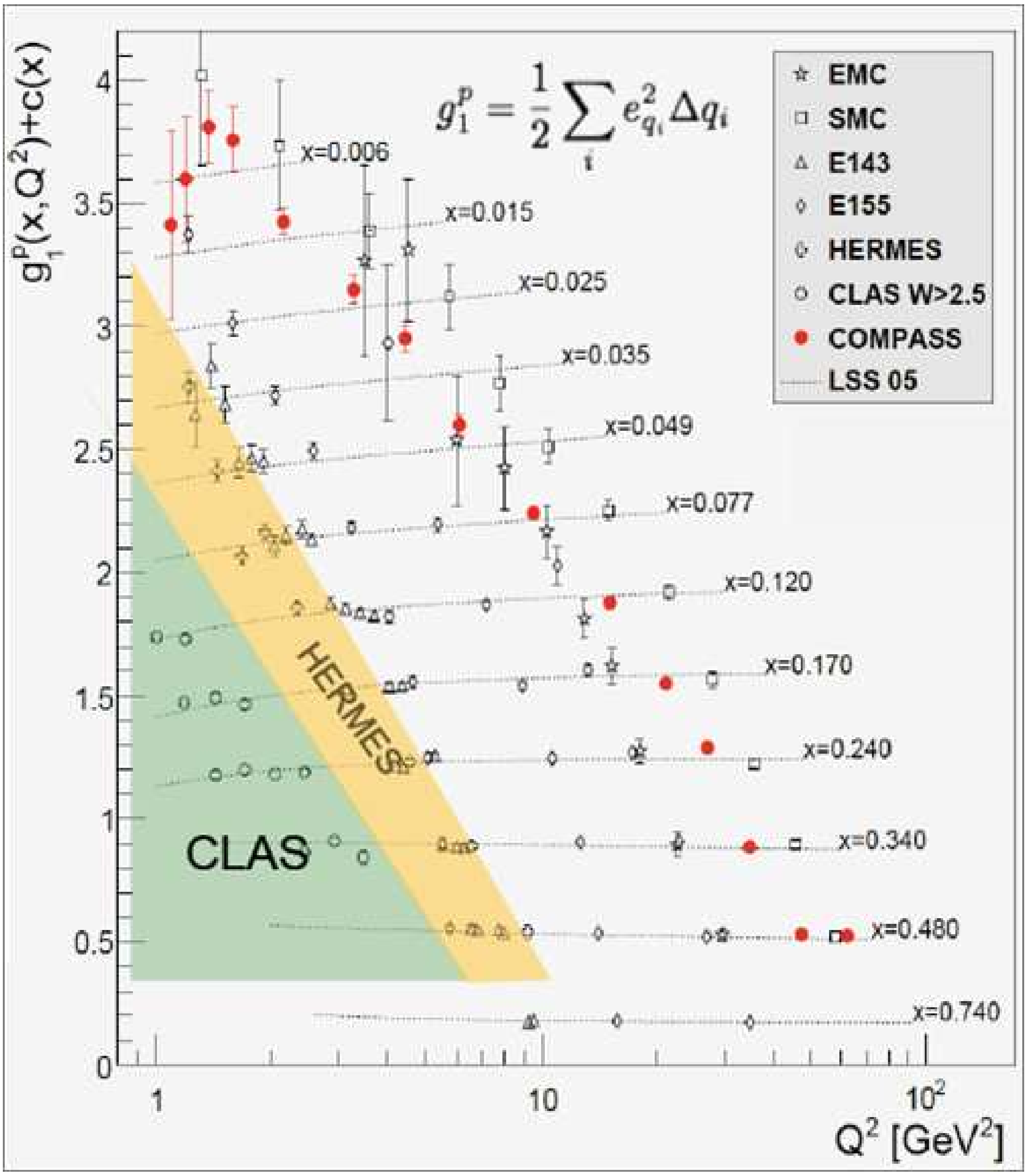

Figure 1.3: World's data on the g_1 structure function as a function of Q^2 for a range of fixed x values [15].

As mentioned in section 1.1.1, polarized DIS accesses $\Delta g(x, Q^2)$ indirectly by measuring scaling violations of the g_1 structure function. Longitudinally polarized pp collisions at RHIC, on the other hand, have the advantage of probing $\Delta g(x, Q^2)$ directly via quark-gluon and gluon-gluon scattering. The observable most sensitive to $\Delta g(x, Q^2)$ is the longitudinal double spin asymmetry, A_{LL}, which is formally defined in terms of helicity-dependent cross sections:

$$A_{LL} \equiv \frac{\sigma_{++} - \sigma_{+-}}{\sigma_{++} + \sigma_{+-}} \tag{1.8}$$

where σ_{++} and σ_{--} are the cross sections for scattering of partons with equal and opposite helicities. The sensitivity of A_{LL} to the gluon polarization can be explicitly seen by factorizing equation 1.8 into perturbative and non-perturbative terms as shown in equation 1.9.

$$A_{LL} = \frac{\sum_{\text{abc}} \Delta f_a \bigotimes \Delta f_b \bigotimes \mathrm{d}\hat{\sigma}^{f_a f_b \to f_c x} \hat{a}_{LL}^{f_a f_b \to f_c x} \bigotimes D^h_{f_c}}{\sum_{\text{abc}} f_a \bigotimes f_b \bigotimes \mathrm{d}\hat{\sigma}^{f_a f_b \to f_c x} \bigotimes D^h_{f_c}} \tag{1.9}$$

The $\hat{\sigma}$ and $\hat{a}_{LL}$ terms represent the hard partonic cross section and the partonic double helicity asymmetry, respectively. Both are calculable within the perturbative QCD (pQCD) framework (see [18]). The $D^h_{f_c}$ term encodes the probability for a parton c to fragment into a hadron h. The f_a and f_b terms are the unpolarized parton distribution functions for the colliding partons, and have been measured to high precision (see for example [13]). Finally, the Δf_a and Δf_b terms are the polarized parton distribution functions. When the partonic scattering involves one or two gluons, then one or both of the Δf terms are $\Delta g(x, Q^2)$, which the experiment hopes to constrain.

1.2.1 Inclusive Jet Studies

The two major experiments at RHIC, STAR and PHENIX, have measured A_{LL} for a number of different final states, but this section will focus only on jet measurements done at STAR. With its large acceptance, STAR is ideally suited for jet measurements. Moreover, jets are a good observable to use when measuring A_{LL} because they arise predominantly from quark-gluon and gluon-gluon scattering at RHIC kinematics, as shown in figure 1.4.

The first inclusive jet A_{LL} results from STAR came from data taken in 2003 and 2004 [25] and were followed by measurements from data taken in 2005 [26]. These early data, despite limited statistics, were already competitive with the available DIS data [27] in disfavoring the maximal gluon polarizations ($\Delta g(x, Q^2) = -g$ and $\Delta g(x, Q^2) =$

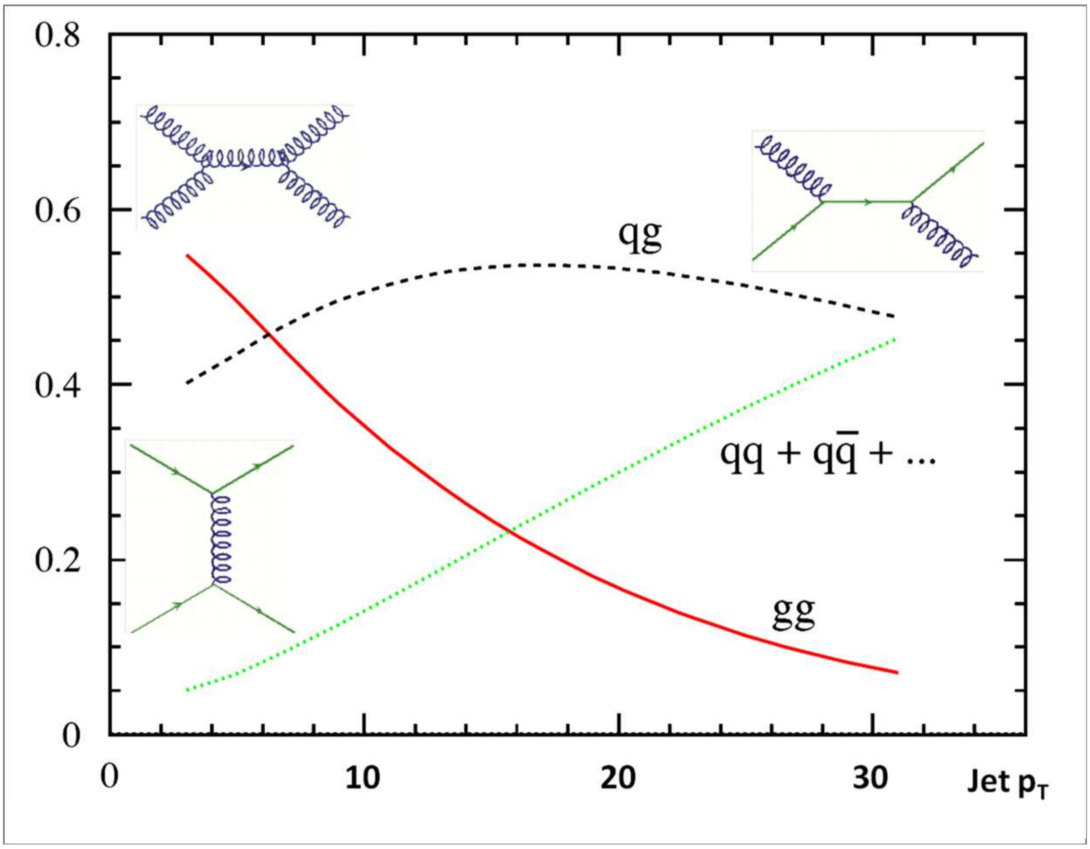

Figure 1.4: The fractions of quark - quark, quark - gluon, and gluon - gluon scattering which contribute to jet production as a function of jet p_T at RHIC kinematics.

$+g$). These results also started placing significant constraints on the allowable value of $\Delta g(x, Q^2)$ in the x region between 0.05 and 0.2. Another longitudinally polarized pp data-set was taken in 2006 [28] which had more than three times the integrated luminosity of the 2005 data-set. In addition, the 2006 data were the first taken with the STAR Barrel Electromagnetic Calorimeter (BEMC) fully installed (previous measurements had included only the West half). The inclusive jet A_{LL} vs jet p_T can be seen in figure 1.5 (see [28]).

Note: for the rest of this section, $\Delta g(x, Q^2)$ will refer to the gluon polarized parton distribution function as a function of x, whereas ΔG will refer to the integral of $\Delta g(x, Q^2)$ over some range of x. The symbol ΔG^{R} will refer specifically to the integral of $\Delta g(x, Q^2)$ over the 'RHIC x range' of 0.05 to 0.2, that is, $\Delta G^{\mathrm{R}} = \int_{0.05}^{0.2} g(x, Q^2)\mathrm{d}x$.

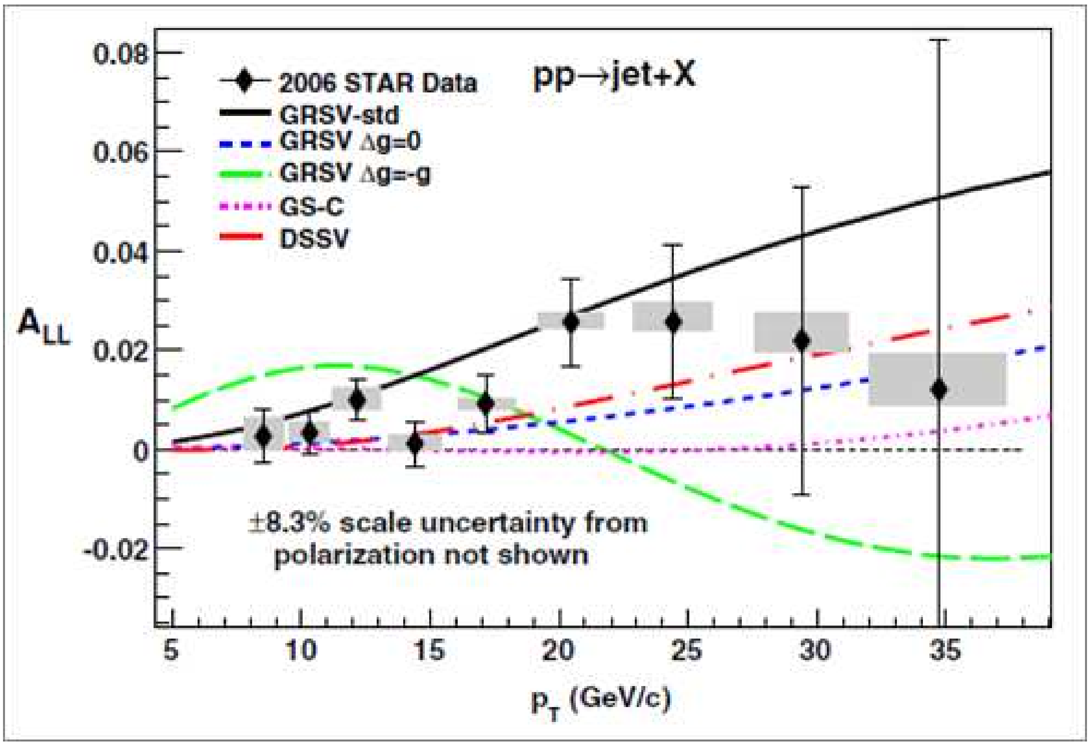

Figure 1.5: The published STAR inclusive jet A_{LL} result from the 2006 RHIC run as well as several model predictions [28],[27], [29]. The black error bars are statistical uncertainties, and the gray boxes are the point-to-point systematic errors.

Although it is sensitive to $\Delta g(x, Q^2)$, the A_{LL} measured in inclusive jet studies integrates over a large range in momentum fraction x, hard-scale Q, and includes contributions from several partonic sub-processes. Therefore, in order to extract $\Delta g(x, Q^2)$ from A_{LL}, a 'global QCD' analysis is needed which takes these issues into account in a simultaneous and consistent way. In 2008, the DSSV group (de Florian, Sassot, Stratmann, and Vogelsang) performed the first global analysis which included RHIC polarized *pp* data in addition to polarized DIS and semi-inclusive DIS data [29] and [30]. The RHIC 2005 results and a preliminary form of the 2006 inclusive jet A_{LL} were included in this analysis.

The results from the DSSV global analysis can be seen in figure 1.6. Panel (a) shows the best fit of $x\Delta g$ as a function of the gluon momentum fraction, along with two estimations of the error from the fitting procedure and an indication of the range of x values which are constrained by the RHIC data. Panel (b) of the same figure shows how each data-set

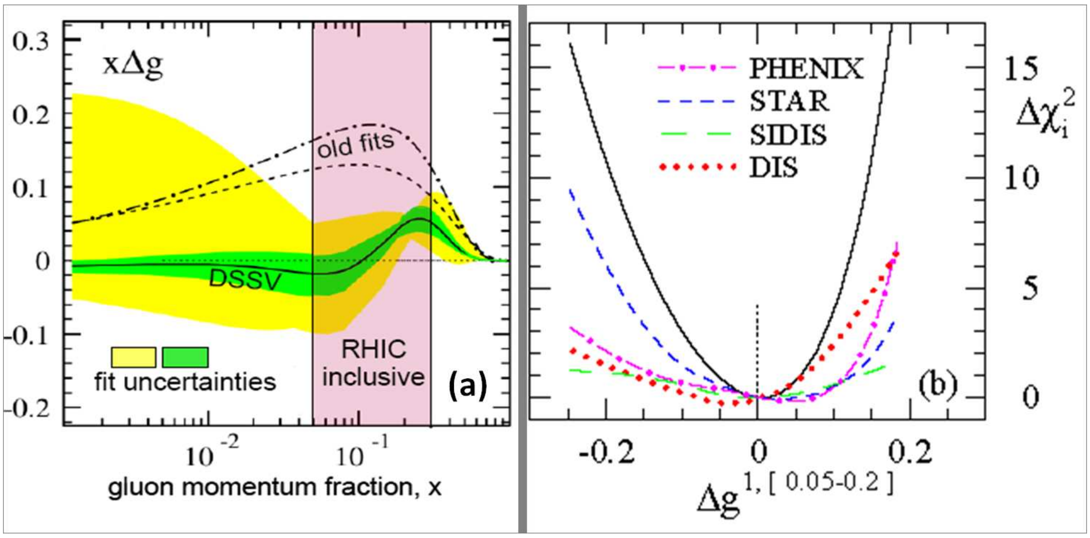

Figure 1.6: Summary of the DSSV global analysis. Panel (a) shows the quantity $x\Delta g$ as a function of x with the x range impacted by RHIC data highlighted in red. Also shown are the error bands for $\Delta\chi^2 = 1$ (green) and $\Delta\chi^2 = 2\%$ (yellow). Panel (b) shows the $\Delta\chi^2$ profile versus ΔG^{R} broken down by data type.

contributes to the $\Delta\chi^2$ profile vs ΔG^{R}. It is seen that the STAR inclusive jet data places the strongest constraints on negative values of ΔG^{R}. Panel (b) also suggests that ΔG^{R} is very close to zero. The value quoted is $0.005^{+0.129}_{-0.164}$ at $Q^2 = 10$ GeV^2 [30].

Although the DSSV global analysis predicts a small value of ΔG in the region covered by the RHIC results, there are rather large uncertainties on this value. The 2009 RHIC run saw the collection of another large longitudinally polarized *pp* data-set, with more than a factor of two increase in the integrated luminosity compared to the 2006 data-set. This larger data-set, coupled with increases in trigger rate due to an improved data acquisition (DAQ) system, has led to an inclusive jet A_{LL} result which is roughly three times more precise than the 2006 result. The preliminary 2009 inclusive jet A_{LL}, shown for two jet pseudorapidity ranges, can be seen in figure 1.7. The most striking feature of this figure is that the data points lie systematically above the 2008 DSSV best fit curve, which is shown in green. This would seem to indicate that the 2009 data prefer a larger value of ΔG^{R}.

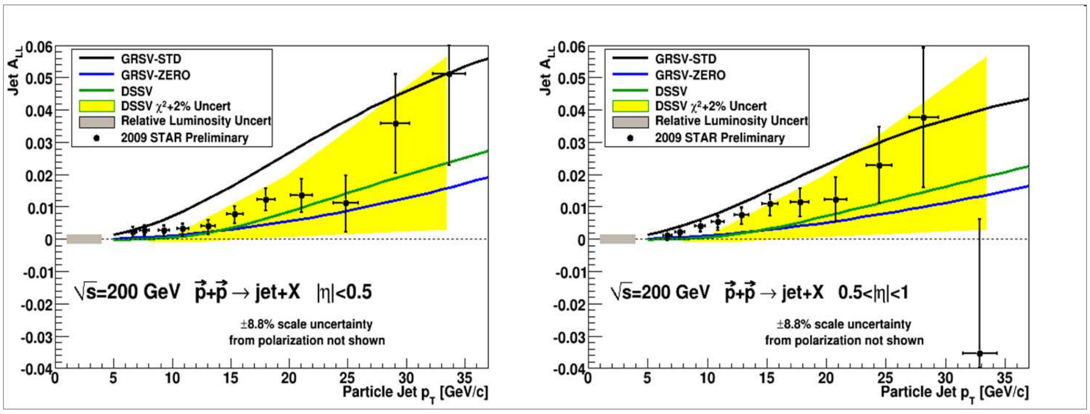

Figure 1.7: The preliminary STAR inclusive jet A_{LL} result from the 2009 RHIC run with several model predictions. The left panel is for jets with pseudorapidities between ± 0.5 and the right panel is for jets with an absolute value of pseudorapidity between 0.5 and 1. The yellow band is the DSSV $\Delta\chi^2 = 2\%$ error.

Recently, the DSSV group performed a new global analysis which included the preliminary 2009 STAR mid-rapidity inclusive jet A_{LL}. as well as the preliminary π^0 A_{LL} from PHENIX and new data from COMPASS ([31], [32], and [33]). This still preliminary analysis is known as DSSV++ [24], [34]. Figure 1.8 shows the $\Delta\chi^2$ profile versus ΔG^{R} for the DSSV and DSSV++ fits. The $x\Delta g$ versus x curves with their associated errors can be seen in figure 1.9. As expected, ΔG^{R} for the DSSV++ best fit has a higher value and smaller uncertainties than that of the original DSSV result. The current DSSV++ result for ΔG^{R} is $0.1^{+0.06}_{-0.07}$ at $Q^2 = 10$ GeV^2, and is the first indication of a non-zero gluon polarization in the 0.05 to 0.2 x range.

The DSSV++ result which contains the 2009 RHIC inclusive A_{LL} data is clearly exciting, as it gives the first evidence that the gluon spin may contribute in a non-negligible way to the spin of the proton. To better quantify what the gluon contribution is, more data will need to be taken, especially data which can reach to lower values of x where the DSSV++ fit is currently poorly constrained, as is evident in figure 1.9. This can be achieved by increasing the center of mass collision energy of the proton beams and/or measuring observables at more forward pseudorapidities. The DSSV++ result can also be improved with better experimental constraints on the shape of $\Delta g(x, Q^2)$ as a function of x. The

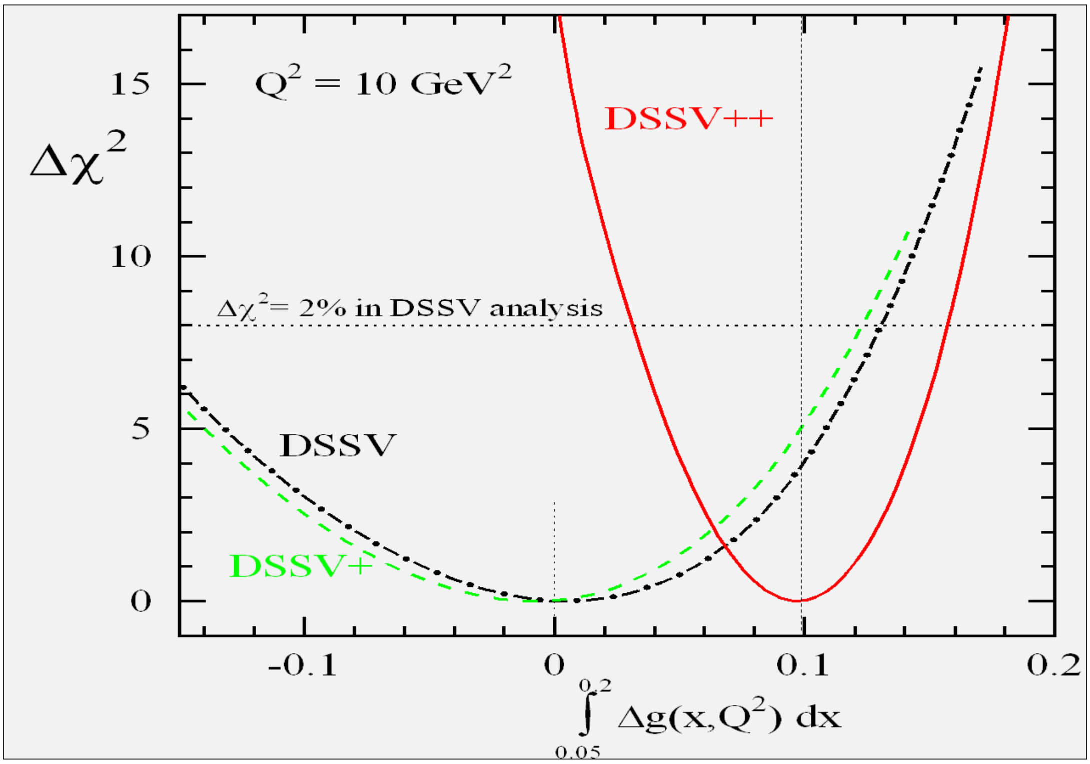

Figure 1.8: The $\Delta\chi^2$ profiles versus ΔG^{R} for the original DSSV analysis (black) and the new DSSV++ analysis (red).

desire for a more precise determination of the x dependence of $\Delta g(x, Q^2)$ motivates the studies presented in this dissertation.

1.2.2 Correlation Studies

Despite only probing the gluon spin indirectly, polarized DIS measurements have one major advantage over polarized pp collisions at RHIC: knowledge of the initial state kinematics. Because the lepton is structureless and does not interact via the strong force, the kinematics in a DIS reaction can be fully determined simply by knowing the energy of the incoming lepton and measuring the energy and scattering angle of the lepton after it has interacted with the target. In pp collisions, the hard scattering which gives rise to high p_T final states is between two partons which can each carry an arbitrary (and unknown) fraction of the momentum of the parent proton. To reconstruct the kinematics of the hard scattering, the energy and momentum of the two colliding partons would need to be determined.

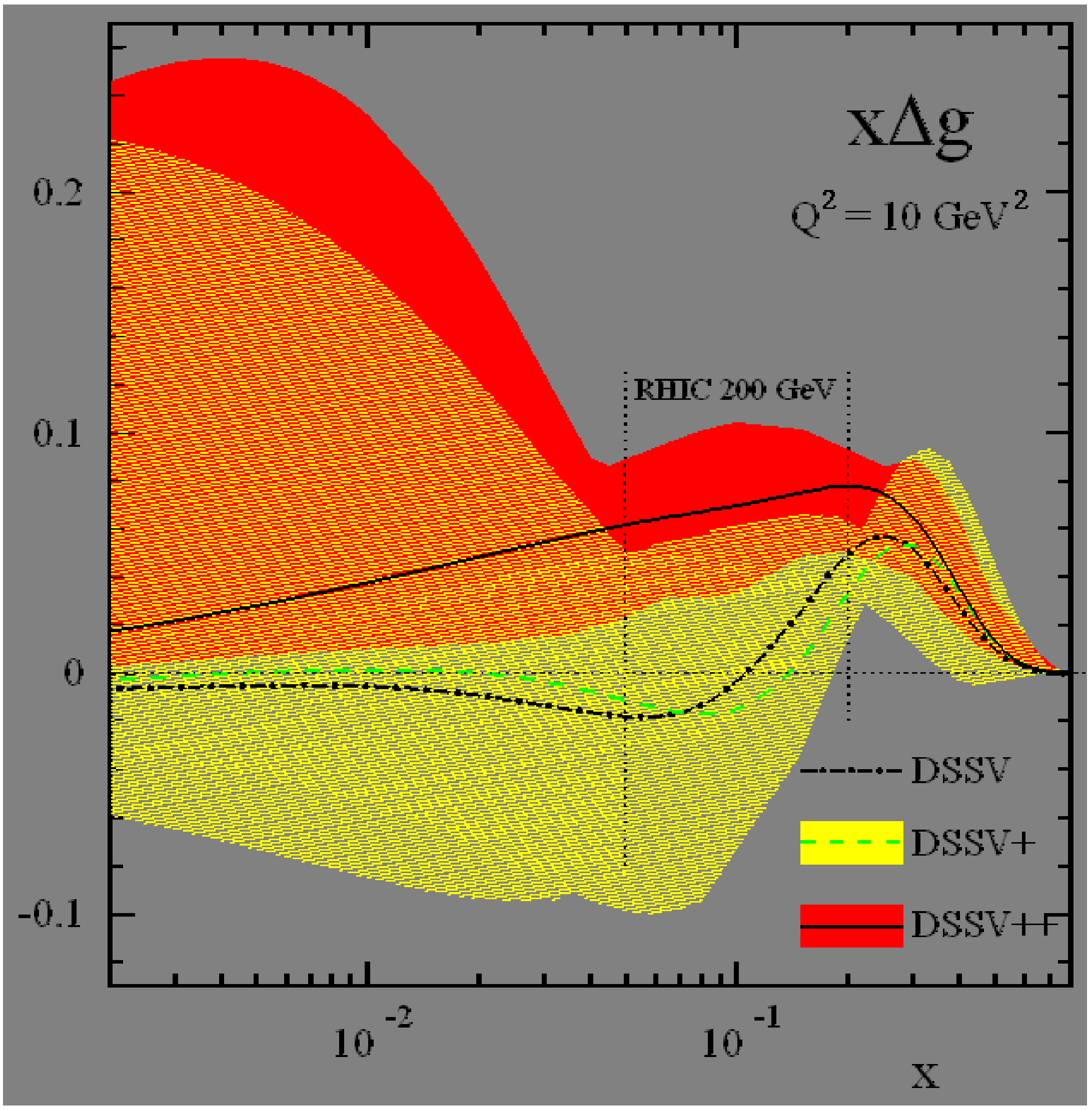

Figure 1.9: The $x\Delta g$ versus x plot for the new DSSV++ fit (solid black line) with the old DSSV fit for comparison (black dash-dot line). All error bands are for $\Delta\chi^2 = 2\%$.

Unfortunately, the exact energies and momenta of the outgoing partons cannot be accessed because the partons must hadronize into colorless final-state particles, and in that process information about the parton can be lost. However, if most of the particles which arise from a fragmenting parton can be detected, they can be used to approximately reconstruct the kinematics of the scattered parton. This is essentially what is done when reconstructing a jet (see chapter 4). Thus, if two jets corresponding to the two hard-scattered partons are measured, their kinematics can be used as a proxy for the kinematics of the scattered partons, and the details of the initial collision can be determined to leading order. Such a two jet system is called a di-jet.

Calculating the kinematics of the initial hard scattering event from the properties of the outgoing partons is a relatively simple matter of working out the relativistic two-body scattering problem (see appendix C). Assuming a completely co-linear system (i.e. no intrinsic transverse momentum) and that rapidity and pseudorapidity are equivalent in this regime, equations 1.10 relate final state observables which can be measured to the initial kinematics of the hard collision. Here x_1 and x_2 are the momentum fractions of the colliding partons, M is the invariant mass of the system, y is the rapidity of the system, and θ is the center of mass scattering angle. Using jets as a proxy for the scattered partons, p_{T3} and p_{T4} are the transverse momenta of the jets, η_3 and η_4 are the pseudorapidities of the jets, and $\sqrt{s}$ is the center of mass collision energy of the proton beams ($\sqrt{s} = 200$ GeV for this study).

$$x_1 = \frac{p_{T3}}{\sqrt{s}} \left(e^{\eta_3} + e^{\eta_4}\right) \tag{1.10a}$$

$$x_2 = \frac{p_{T4}}{\sqrt{s}} \left(e^{-\eta_3} + e^{-\eta_4}\right) \tag{1.10b}$$

$$M = \sqrt{x_1 x_2 s} \tag{1.10c}$$

$$y = \frac{1}{2} \ln\left(\frac{x_1}{x_2}\right) = \frac{\eta_3 + \eta_4}{2} \tag{1.10d}$$

$$|\cos(\theta)| = \tanh\left(\frac{\eta_3 - \eta_4}{2}\right) \tag{1.10e}$$

Although equations 1.10 are not exact relationships between the final state observables and the initial collision kinematics, due to higher-order effects which cause the jet properties to deviate from the initial parton properties, they illustrate how di-jet observables offer more information about the initial state than corresponding inclusive measurements. In addition, these equations give guidance on how to bin the di-jet events so as to preferentially select certain hard-scattering kinematics.

Note that the expression for the di-jet mass in equation 1.10 is not the one used in the analyses. When finding the mass of a di-jet in data or simulation, the more general formula is used equation 1.11. Here, the $m, p_T, \eta, \text{and} \phi$ terms refer to the masses, transverse momenta, pseudorapidities, and azimuthal angles respectively of the two jets making up the di-jet.

$$M = \sqrt{m_3^2 + m_4^2 + 2\sqrt{m_3^2 + p_{T3}^2} + \sqrt{m_4^2 + p_{T4}^2}\cosh\left(\eta_3 - \eta 4\right) - 2p_{T3}p_{T4}\cos\left(\phi_3 - \phi_4\right)} \tag{1.11}$$

1.3 Dissertation Structure

This chapter has given a brief review of proton structure, the role RHIC data have played in constraining the gluon contribution to the spin of the proton, and finally the motivation for performing studies with di-jet observables. This dissertation describes the measurement of the di-jet cross section, as well as the di-jet double helicity asymmetry A_{LL}, both as functions of the di-jet invariant mass. The results presented are based on 17.1 pb^{-1} of data collected in 2009 (Run IX) by the STAR detector at RHIC.

The remainder of this dissertation is organized in the following way. Chapter 2 describes the RHIC facility and the challenges associated with accelerating beams of polarized protons. It also describes the STAR detector and the subsystems which are relevant to these analyses. Chapter 3 gives a summary of the 2009 data-set used, including details on quality assurance, triggering, and the determination of the integrated luminosity of the data-set. A brief description of the associated simulation sample is also given. Chapter 4 gives an overview of how jets were reconstructed and how di-jets were selected for these analyses. Chapters 5 and 6 describe the measurements of the di-jet cross section and di-jet A_{LL}, respectively, and compares these results to predictions of current theoretical models. Finally, chapter 7 gives a brief summary of the results presented.

Chapter 2

Experimental Setup

Chapter 1 discussed the theoretical underpinnings of the measurements made in this thesis and highlighted the advantages of polarized *pp* collisions as a means of investigating the gluon contribution to the spin of the proton, ΔG . This chapter gives a brief overview of the experimental setup. The first section focuses on the RHIC facility and some of the technical challenges related to accelerating and colliding polarized protons. The second section focuses on the STAR detector with which the data in this thesis were collected.

2.1 The Relativistic Heavy Ion Collider

The Relativistic Heavy Ion Collider (RHIC) [35], [36] is located at Brookhaven National Laboratory (BNL) on Long Island, New York. The idea to build a heavy ion collider stems from the 1983 long-range plan for nuclear science which considered the construction of such a facility the highest priority. Construction of RHIC started in 1991 utilizing an existing 3.8 km tunnel originally dug for the ISABELLE project. Construction was completed in 1999 and the first Au-Au collisions were recorded in 2000.

RHIC is capable of colliding a number of different ion species over a wide range of center of mass energies, to facilitate the study of the QCD phase diagram. In addition to heavy ions, RHIC has a second mode of operation which makes it unique: RHIC is the only facility in the world capable of accelerating and colliding polarized protons. RHIC can collide polarized protons at center of mass energies exceeding $\sqrt{s} = 500$ GeV, which

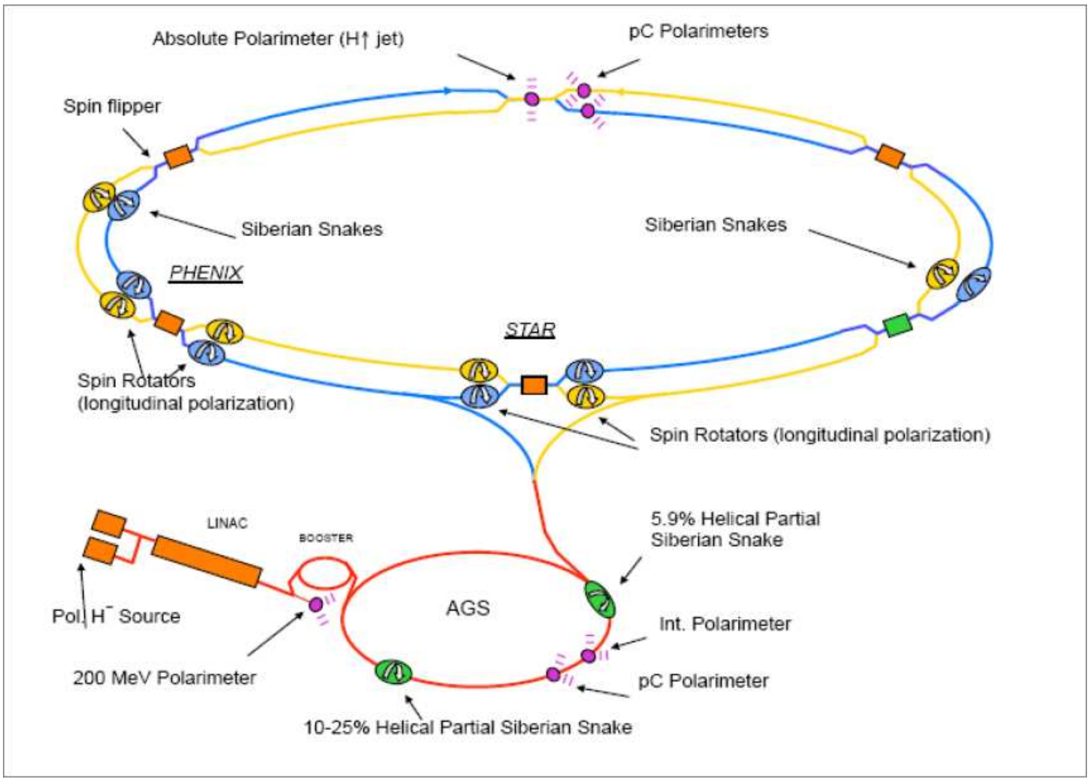

Figure 2.1: Layout of the areas of the RHIC accelerator complex pertinent to polarized *pp* running.

allows for the study of the proton spin structure in kinematic regimes inaccessible to fixed target experiments. The remainder of this chapter will detail RHIC as it operates in *pp* mode. A full overview of RHIC as a polarized proton collider can be found here [37]. The layout of the RHIC facility can be seen in Fig 2.1.

2.1.1 Proton Acceleration Path

In *pp* mode, the acceleration chain begins with an optically pumped H^- ion source called OPPIS [38]. This source was constructed at TRIUMF from the OPPIS source previously used at KEK.

The design luminosity for RHIC is $2\times10^{32}\text{cm}^{-2}\text{s}^{-1}$, which corresponds to roughly 2×10^{11} protons per bunch. OPPIS produces H^- ions in 300 μs pulses with currents of 0.5 mA and polarizations of about 80%, which translates to roughly $9\times10^{11} H^-$ ions/pulse. The high pulse intensity is needed to compensate for losses along the acceleration chain. The

H^- beam from the source has an energy of 35 keV and is accelerated to 200 MeV by an RFQ and linac system, after which it is strip injected and captured as a single bunch in the booster. The acceleration of the H^- beam to 200 MeV is about 50% efficient, meaning the bunch in the booster will contain 4×10^{11} protons. Once in the booster, the bunch is accelerated to 1.5 GeV and injected into the Alternating Gradient Synchrotron (AGS) where it is further accelerated to 25 GeV and injected into RHIC via the AGS-to-RHIC (AtR) transfer line.

RHIC consists of two rings (blue and yellow) which can each hold 120 proton bunches, although in normal operation only 109 bunches are filled. Because the bunches are injected one by one, each bunch can have an independent spin orientation. The bunch-by-bunch spin patterns are carefully chosen to help reduce systematic errors in the final measurements. Once all desired bunches are filled, the beams are accelerated to the desired energy and stored. The time from the first bunch injection into RHIC to the dump of the beam is called a "Fill". It takes roughly 10 minutes to fill both RHIC rings and accelerate to full energy. A good fill can last on the order of 8 hours, so data taking constitutes most of this time.

2.1.2 Siberian Snakes

The acceleration of polarized protons is complicated by the fact that as they are being accelerated, the protons will encounter depolarizing resonances which will perturb the spin vector and can cause a loss of polarization. To better understand the difficulties in maintaining proton polarization during acceleration, and the techniques used to overcome them, it will be instructive to briefly review the evolution of a spin vector undergoing acceleration in a circular collider.

The change in the proton's spin vector is governed by the Thomas-BMT equation

$$\frac{\mathrm{d}\vec{P}}{\mathrm{d}t} = -\left(\frac{e}{\gamma m}\right)\left[G\gamma\vec{B}_{\perp} + (1+G)\,\vec{B}_{\parallel}\right] \times \vec{P} \tag{2.1}$$

where $\vec{P}$ is the proton's spin vector (in the frame which moves with the proton), G is the anomalous magnetic moment of the proton ($G = 1.7928$), $\gamma = E/m$ is the Lorentz factor, and $\vec{B}_\perp$ and $\vec{B}_\parallel$ are the transverse and longitudinal magnetic fields, respectively. The Thomas-BMT equation is similar to the equation which describes the orbital motion of a proton in an external magnetic field

$$\frac{\mathrm{d}\vec{v}}{\mathrm{d}t} = -\left(\frac{e}{\gamma m}\right)\left[\vec{B}_\perp\right] \times \vec{v} \tag{2.2}$$

where $\vec{v}$ is the velocity vector of the proton. For the case of an ideal circular accelerator, there are no longitudinal magnetic fields and equations 2.1 and 2.2 differ only by a factor of $G\gamma$, which is known as the spin tune (ν_{sp}). The spin tune gives the number of extra precessions the proton spin vector makes in one full orbit. At top RHIC energies ν_{sp} can reach values of 478.

The spin tune is also related to the depolarizing resonances, as the condition for a resonance is that the spin tune matches the frequency of the perturbation pushing the spin vector away from the stable vertical direction. There are two main types depolarizing resonances: imperfection resonances, which are caused by magnet imperfections and misalignments; and intrinsic resonances, which are caused by the focusing fields. Imperfection resonances occur when the spin vector is in the same orientation each time the perturbation is reached, thus the condition for this resonance can be written $G\gamma = n$, where n is an integer. Solving for the energy, one sees that intrinsic resonances are separated by only 523 MeV. Intrinsic resonances are reached when $G\gamma = kP \pm \nu_y$ where k is an integer, P is the superperiodicity, and ν_y is the vertical betatron tune.

When protons are accelerated to low energies, as they are in the booster, there are few resonances to traverse, and the accelerator parameters can be adjusted in such a way as to minimize polarization loss. For higher energies, accelerator adjustments no longer work and a new technique is needed to maintain polarization. At RHIC, polarization is maintained by using ‘Siberian Snakes’, which are arrays of helical dipole magnets that flip the spin direction by 180° around a horizontal axis. Each ring contains two Snakes which flip the spin around horizontal axes which are perpendicular to each other. This has the net affect of rotating the spin vector by 180° around the vertical axis. Thus, the spin tune is fixed at half-integer values, independent of beam energy. Therefore the conditions for depolarizing resonances are never met as long as the vertical betatron tune does not take a half-integer value.

2.1.3 Spin Rotators

The stable spin direction at RHIC is transverse to the horizontal direction of motion, but many of the measurements of interest to the STAR spin program require the collision of longitudinally polarized protons. The spin orientation is switched from the transverse to longitudinal direction via spin rotators which, like the snakes, are sets of helical dipole magnets. The interaction regions at 6 and 8 o'clock both have spin rotators, so the STAR and PHENIX experiments can independently run in either transverse or longitudinal mode. Each interaction point requires four rotators, two for each beam. The first magnet rotates the spin vector from transverse to longitudinal, and the second rotates it back to transverse after the beam has passed through the interaction region of the detector.

2.1.4 The Zero-Degree Calorimeter System

The Zero-Degree Calorimeter (ZDC) [39] system at RHIC was designed to provide a common event characterization and luminosity monitoring capability for each of the four original experiments on the ring. Each experimental interaction region has two sets of ZDCs located behind the DX magnets (see Figure 5 in [36]). The ZDCs are small hadronic calorimeters consisting of layers of scintillators and tungsten plates. The ZDCs can be used to trigger minimum-bias events in which the ZDCs on both sides of the interaction region register signals within some time window after a RHIC bunch crossing. The ZDCs and BBCs (see section 2.2.4) together are used in the relative luminosity analysis. Relative luminosities (discussed further in sec 6.3) are ratios of luminosities for bunch crossings with different beam spin combinations, and are an essential component of the A_{LL} measurement.

2.1.5 Polarimeters

Beam polarization values are an essential ingredient to the spin-dependent measurements made at RHIC, and also provide important feedback to the accelerator physicists. RHIC uses two complementary systems to measure beam polarization: the proton-carbon (pC) polarimeter, which is capable of fast measurements but cannot provide an absolute polarization value, and the hydrogen gas jet (H-Jet) polarimeter, which takes much longer to accumulate statistics but which can provide an absolute polarization value that can be used to normalize the pC measurements. Both systems take advantage of elastic scattering in the so-called coulomb-nuclear interference (CNI) region where interference between the electromagnetic spin-flip and hadronic spin-nonflip amplitudes lead to a sizable analyzing power A_N (see [40], [41], and [42]). A_N is a measure of the left-right asymmetry of the cross section in the scattering plane perpendicular to the beam polarization.

The proton-carbon polarimeter apparatus consists of a thin carbon ribbon which is mechanically inserted into the beam, surrounded by a ring of silicon detectors which detect the scattered (recoil) carbon nuclei. The protons are scattered at very forward angles, so the carbon nuclei are emitted roughly perpendicular to the beam direction. The polarization of the beam incident on the carbon target can be written in terms of the analyzing power for the pC elastic scattering and the left-right asymmetry of scattered carbons:

$$P_{\text{beam}} = \frac{1}{A_N^{pC}} \frac{N_L - N_R}{N_L + N_R} \tag{2.3}$$

where A_N^{pC} is the analyzing power and $N_{L(R)}$ are the numbers of carbon nuclei scattered to the left(right) of the polarization direction. Unfortunately, A_N^{pC} is not well known at RHIC energies, so the pC polarimeters alone cannot provide absolute beam polarizations. The pC system does however provide relative polarization values between different fills. In addition, the large proton-carbon elastic cross section means that several measurements can be completed during the course of a fill, providing information on polarization loss. Finally, because the carbon target is narrow compared to the width of the beam, the pC polarimeter can measure the polarization at different points along the transverse dimension of the beam.

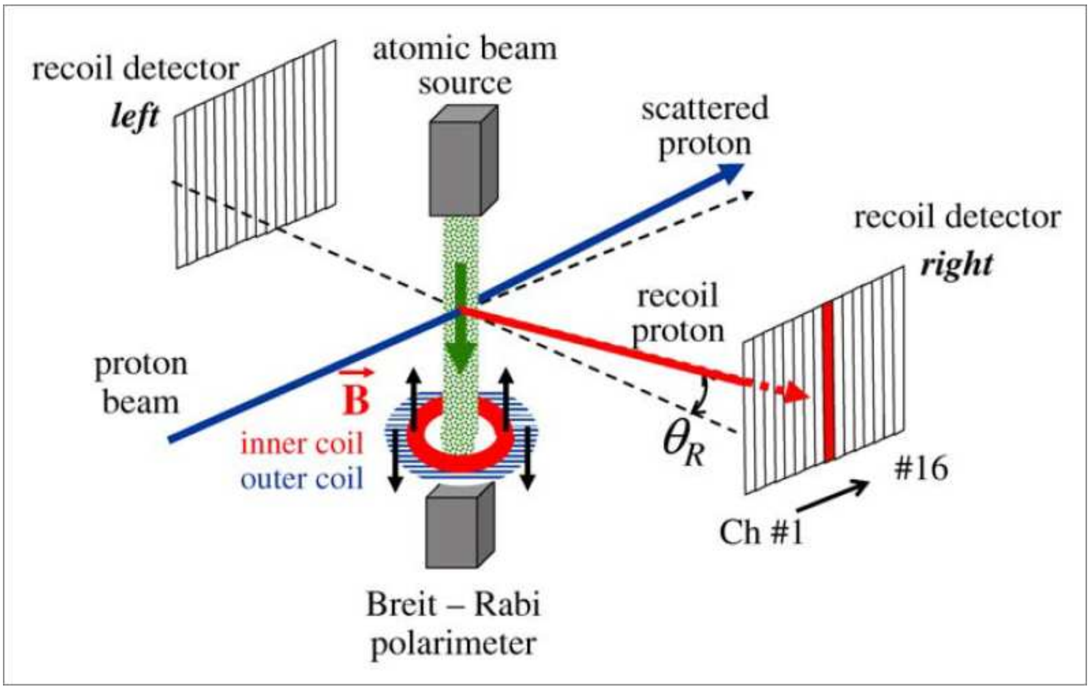

Figure 2.2: Schematic of the H-jet polarimeter system.

The need for absolute beam polarization values motivated the construction of a polarized H-jet target [43] which was installed at the 12 o'clock interaction point. Like the *pC* polarimeter system, the H-jet system takes advantage of scattering in the CNI region but the target is now a thermal beam of polarized atomic hydrogen. Because the beam and target particles are identical, the analyzing powers are equal, and the beam polarization can be expressed purely in terms of the target polarization and the beam and target left-right scattering asymmetries:

$$P_{\text{beam}} = \frac{\epsilon_N^{\text{beam}}}{\epsilon_N^{\text{target}}} P_{\text{target}} \qquad \epsilon_N = \frac{N_L - N_R}{N_L + N_R} \tag{2.4}$$

The beam and target asymmetries can be measured by averaging over the spin states of the target and of the beam, respectively. The absolute polarization of the H-Jet target is measured with a Breit-Rabi polarimeter with an accuracy of roughly 2%. A schematic of the H-Jet polarimeter setup can be seen in Fig 2.2 .

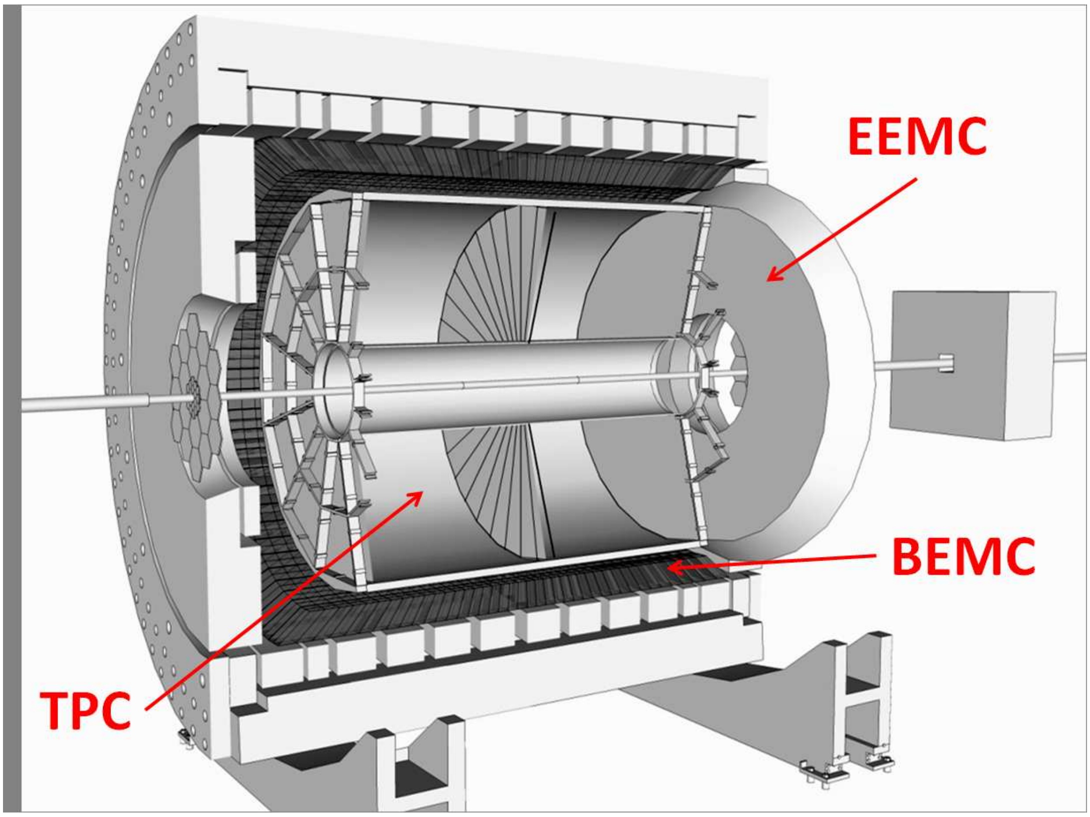

Figure 2.3: Schematic of the STAR detector with the Time Projection Chamber (TPC), Barrel Electromagnetic Calorimeter (BEMC), and Endcap Electromagnetic Calorimeter (EEMC) subsystems highlighted.

2.2 The Solenoidal Tracker at RHIC

The Solenoidal Tracker at RHIC (STAR) [44] is one of four experiments originally on the RHIC ring, the other three being PHENIX [45], BRAHMS [46], and PHOBOS [47]. STAR and PHENIX are the only remaining active experiments. STAR is a large acceptance detector with a solenoidal design. There are many STAR sub-systems which are optimized for different measurements or different kinematic regions. This section will detail three of the primary sub-systems used in the analyses presented in this thesis. In addition, a brief description of the BBCs, which were used in the relative and integrated luminosity analyses, will be provided. A diagram of the STAR detector can be seen in Fig 2.3.

2.2.1 The Time Projection Chamber

The central component of the STAR detector is the Time Projection Chamber (TPC) [48] which provides charge particle tracking and particle identification. The TPC measures 4.2 meters long and 4 meters in diameter, with the drift volume extending radially from 50 to 200 cm from the beam line. The TPC volume is filled with a mixture of 10% methane and 90% argon (P10) and the entire volume sits in a 0.5 Tesla solenoidal magnetic field oriented parallel to the beam pipe [49]. There is also a uniform electric field of roughly 135 V/cm parallel to the magnetic field.

Charged particles created by proton-proton or heavy ion collisions traverse the TPC and ionize the P10 gas. The electrons from the ionized gas drift in the electric field to the TPC endcaps, where they are read out by a multi-wire proportional counter (MWPC) system with readout pads. The electrons avalanche in the high field surrounding the MWPC wires and induce an image charge on the readout pads. A given avalanche is shared over several readout pads so the x-y position of the avalanche can be determined to a fraction of the pad size. The z position of an ionization event is determined by measuring the electron drift time and combining it with precision measurements of the the electron drift velocity made by a dedicated laser system [50]. With the x, y, and z positions of the ionization events fixed, the full trajectory of a charged particle can be reconstructed. Because the TPC is situated in a solenoidal magnetic field, the charged particles are bent into helical trajectories with a radius of curvature proportional to the particle's momentum in the plane transverse to the field direction, p_T. Thus, by measuring the curvature of the particle's trajectory, the momentum of the particle can be determined. The particle momentum is used along with energy deposition in the calorimeters (described in the next sections) to reconstruct jets.

The charged particle tracking provided by the TPC is crucial for vertex finding. The nominal collision point for particles from opposing beams is at the center of STAR (z=0), yet the actual collisions are distributed normally around z=0 with a sigma of roughly 60 cm for *pp* collisions. The particle trajectories reconstructed by the TPC can be projected back to the beam line, and the points where several tracks converge are designated as vertices. These vertices indicate the position of the collision (as well as the decay positions of long-lived daughter particles). Determining the position of the collision is necessary for determining the pseudorapidity ($\eta = -\ln\left[\tan\left(\frac{\theta}{2}\right)\right]$) of tracks, which is a quantity of interest in many analyses.

One consequence of the TPC design which will be of crucial importance to future extensions of the di-jet cross section and asymmetry measurements into the Endcap is that the track-finding efficiency decreases for tracks with a pseudorapidity greater than about 1.2. As explained above, charged particle tracks are reconstructed when the ionization electrons they produce as they traverse the TPC volume drift to the endcaps and avalanche onto readout pads. These pads are situated in rows (padrows) oriented roughly perpendicular to a straight radial line emanating from the interaction point (see Fig 2.4). The software which constructs tracks from the raw ADC values recorded by the readout pads requires that a minimum number of padrows contribute to a track in order for it to be reconstructed. Tracks with pseudorapidity $|\eta| > 1$ will not traverse the entire transverse extent of the endcap before they leave the TPC, and thus will not drift charge onto all the padrows, leading to a reconstruction inefficiency at high pseudorapidity. The effects of this inefficiency will need to be studied in detail for future Endcap analyses.

2.2.2 The Barrel Electromagnetic Calorimeter

The Barrel Electromagnetic Calorimeter (BEMC) [51] is the primary calorimeter subsystem in STAR. It covers two units of pseudorapidity ($-1 < \eta < 1$) and 2π in azimuth. The BEMC is situated outside the TPC, with an inner radius roughly 220 cm from the beam pipe. Mechanically, the BEMC is divided into 120 modules, each covering 6° of azimuth and 1 unit of psudorapidity. Each module is divided into 40 optically isolated 'towers' which project back to the nominal interaction point (see Fig 2.5). Each tower covers 0.05 units of rapidity and about 0.052 radians in azimuth. At $\eta = 0$ the BEMC is roughly 20 radiation lengths (χ_0) deep, meaning it can fully contain most electromagnetic showers produced at RHIC energies.

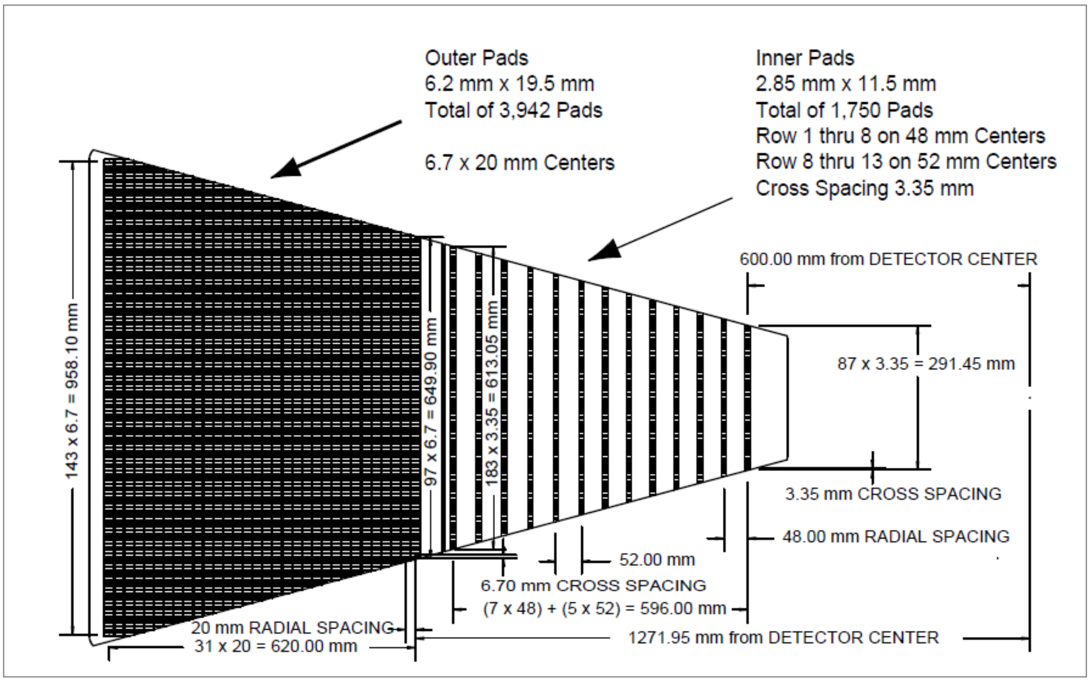

Figure 2.4: Layout of one TPC endcap sector [48]. The padrows are the dark vertical lines (padrow density is greater in the outer sector). The right side of the figure is closest to the beam line.

The BEMC is a lead-scintillator sampling calorimeter designed to detect the energy of electrons, photons, and other particles which shower electromagnetically. Each tower consists of alternating layers of lead and plastic scintillator: there are 20 layers of 5 mm thick lead, 19 layers of 5 mm thick plastic scintillator, and 2 layers of 6 mm thick plastic scintillator (see Fig 2.5). The first two scintillator layers are 6 mm thick and comprise the preshower detector. There is also a shower maximum detector (SMD) located roughly 5.6 radiation lengths deep, which provides precision information on the transverse shape of electromagnetic showers. Neither the preshower nor the SMD are used in the analyses presented in this thesis. The light from all of the scintillator layers in a given tower is combined and read out by a single photo-multiplier tube (PMT).

The summed light output from the tower scintillators is converted to a digital signal which is approximately proportional to the incident particle energy. The tower energy deposits, along with track momenta, are used to reconstruct jets. The vector from the

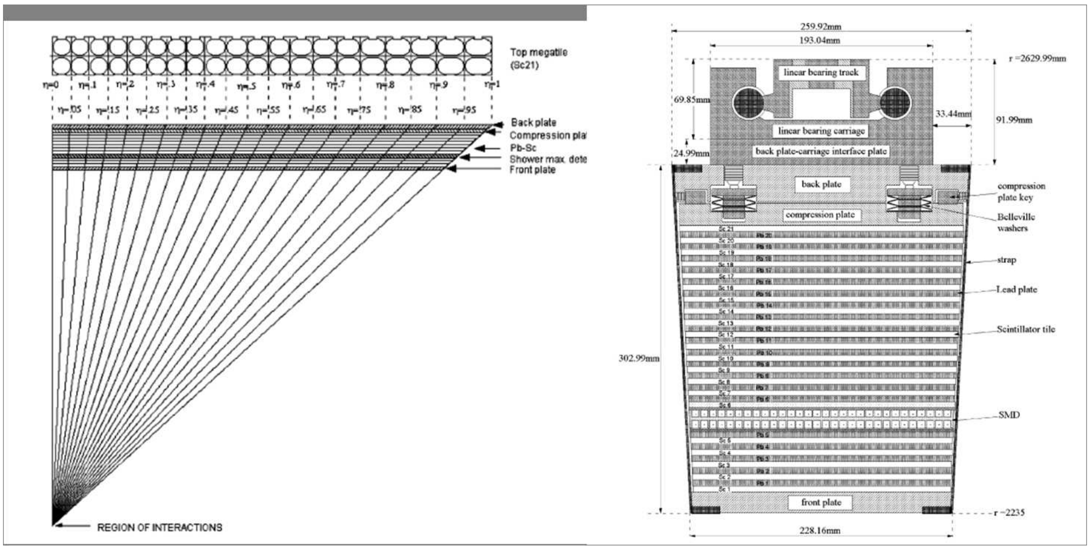

Figure 2.5: Structure of a BEMC Module [51]. The left hand figure shows an edge-on view of a module highlighting the projective nature of the towers. The right hand figure shows an end-on view of a module highlighting the lead-scintillator layering.

interaction vertex to the tower is used in the determination of the thrust axis of a jet. It is important to also note that because of its fast readout time, the BEMC is used in the STAR trigger system to record events most likely to be of interest to the jet and other analyses.

2.2.3 The Endcap Electromagnetic Calorimeter

The Endcap Electromagnetic Calorimeter (EEMC) [52] is the other major electromagnetic calorimeter subsystem in STAR. Like the BEMC, it is a segmented lead-scintillator sampling calorimeter. The EEMC covers the west endcap of the TPC, extending over nearly one unit of rapidity ($1.086 < \eta < 2.0$), and covering the full 2π in azimuth. Like the BEMC, the EEMC consists of alternating layers of scintillator and lead. The first two and the last scintillator layers are read out separately from the other scintillator layers, and make up the pre and post shower components, respectively. There are also two SMD planes located after the 5th scintillator layer. The EEMC is divided into 720 optically isolated projective towers, each read out by a single PMT. As with the BEMC, the energy deposits in the EEMC towers are used in the reconstruction of jets. Like the BEMC, the EEMC is also used to trigger on events of interest, and allows STAR to trigger on jets in

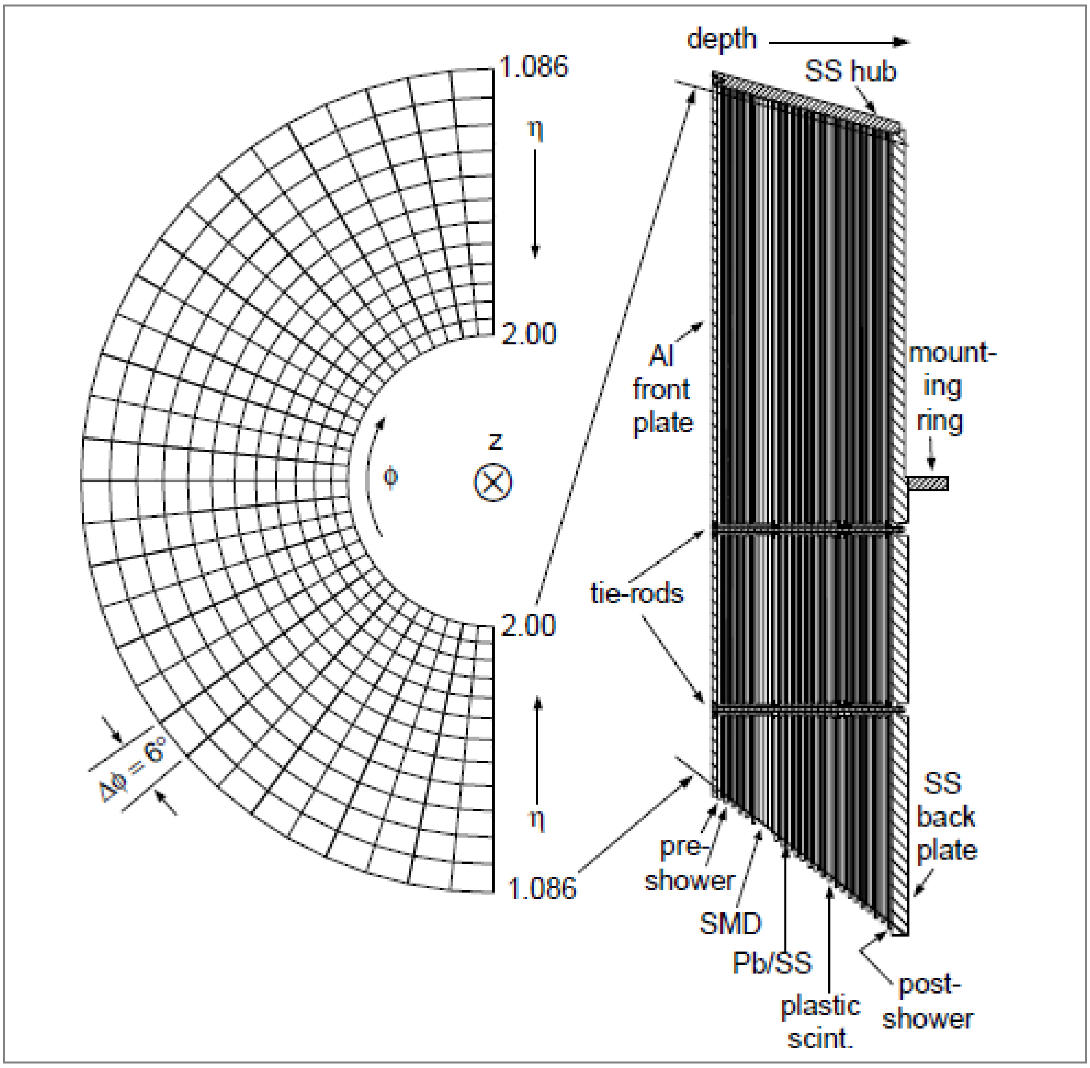

Figure 2.6: Structure of the EEMC [52]. The left hand figure shows a beam's eye view with tower boundaries indicated. The right hand figure shows a profile view of the lead-scintillator stack.

the region $1 < \eta < 2$. A schematic view of the face and profile of the EEMC is presented in Fig 2.6 .

2.2.4 The Beam-Beam Counters

The Beam-Beam Counters (BBC) [53] are two sets of hexagonal scintillator tiles surrounding the beam pipe just outside the East and West pole tips of STAR. The East and West modules of the BBC each sit 3.75 meters from the center of STAR. A BBC module

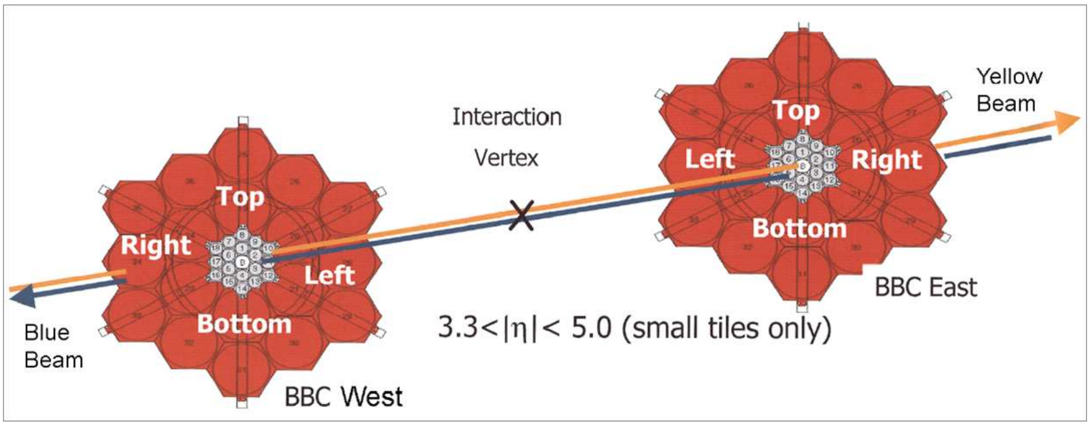

Figure 2.7: Schematic view of the Beam-Beam Counters [53]

consists of a set of large tiles and a set of small tiles. Each set of tiles is divided into two rings, with six tiles in the inner ring and twelve tiles in the outer ring. Only the eighteen small tiles, which are situated closest to the beam line, are used in this analysis. They cover a pseudorapidity range of roughly $3.4 < |\eta| < 5.0$.

The BBCs have several uses at STAR, including luminosity monitoring, local polarimetry, and relative luminosity determination. As with the ZDC, the BBC can be used to trigger on minimum-bias events by requiring hits in the East and West modules within some time window with respect to the bunch crossing. The minimum-bias rate is proportional to the luminosity, which is needed in the cross section analysis. The BBC also acts as a local polarimeter which can measure the transverse and radial components of the beam. This capability provides essential feedback when setting the currents in the spin rotators (see section 2.1.3), which are used to switch the beam polarization from the transverse to the longitudinal direction. Residual transverse or radial components of the beam register as a transverse asymmetry in the BBC, and the spin rotator magnet currents are then changed until these asymmetries are consistent with zero. Finally, as with the ZDC, the BBC can be used to determine the luminosities of each bunch crossing relative to the others. Bunch crossings with the same spin combination are combined, and luminosity ratios of different spin combinations can be formed. These relative luminosities (discussed further in sec 6.3) are an essential factor in the A_{LL} analysis. The comparison of relative luminosities as measured with the ZDC and BBC is used to determine the systematic error on the final relative luminosity values.

Chapter 3

Data and Simulation Samples

The data used in the analyses presented in this thesis were collected by the STAR detector at RHIC during Run IX which took place during the 2009 calender year. The data were taken during pp running with a center of mass energy of $\sqrt{s} = 200$ GeV. To complement this data set, a large simulation sample was created. The simulation sample is needed to quantify detector effects and calculate efficiencies. This chapter gives an overview of the data and simulation samples.

3.1 Data Quality Assurance

STAR records data during discreet periods called runs (not to be confused with the RHIC run period, which lasts for many months) which can last a few minutes for diagnostic tests up to nearly an hour when taking production data. The 200 GeV portion of Run IX contains well over 2000 runs, many of which are not suitable for the analyses presented in this thesis. This section describes the run selection criteria, as well as the human and script-based quality assurance (QA) checks performed on the data.

The run selection and QA were completed in several steps, the first of which was an initial human QA. A list was created of all Run IX 200 GeV runs longer than 1 minute which were not test or setup runs. This list was divided among several members of the STAR collaboration who looked at the Shift Log and several sets of diagnostic plots for each run, noted any problems with the detector, and discarded runs which contained

major problems. From the remaining runs, only those with the trigger setups production2009_200Gev_Hi, production2009_200Gev_Lo, and
production2009_200Gev_Single were retained (see section 3.2). The trigger setup denotes the specific triggers included in the run: production2009_200Gev_Hi contains only the L2JetHigh triggered events, production2009_200Gev_Lo contains only the JP1 triggered events, and
production2009_200Gev_Single contains both L2JetHigh and JP1 triggered events. The L2JetHigh and JP1 triggers will be discussed further in section 3.2. Runs which were shorter than 3 minutes or which did not include the TPC, BEMC, and EEMC were discarded. The resulting run list contained 1269 runs.

The next step in the QA process was to look at various quantities of interest to the analyses on a run-by-run basis and identify outliers. The quantities looked at are things which could be affected by the state of the detector, such as the number of tracks reconstructed or the energy deposited in the calorimeter in a given event. An event is the data recorded by STAR corresponding to a single bunch crossing; there are many events in a given run. For each run, the per event averages of the quantities looked at are plotted and the mean over all runs is found. Individual runs for which the per event mean of some quantity deviates too much from the global mean are investigated further, and runs which contain means farther than 5σ from the global mean are discarded. Figure 3.1 gives an example of the type of plots used in this part of the QA. There were 1112 runs remaining after the run-by-run QA was performed.

The calculation of A_{LL} requires three pieces of information for each run: the polarization values for each beam, the relative luminosity values, and the jet yields for each helicity combination, which requires valid spin bit values. Relative luminosity is described in section 6.3 and the spin bits are described in section 6.2 . The last step in the QA and run selection process is to remove runs in which any of the above information is missing. Removing these leaves 1029 runs. It was also found later that the production2009_200Gev_Lo trigger setup caused an issue with the analyses, so all fifty of these

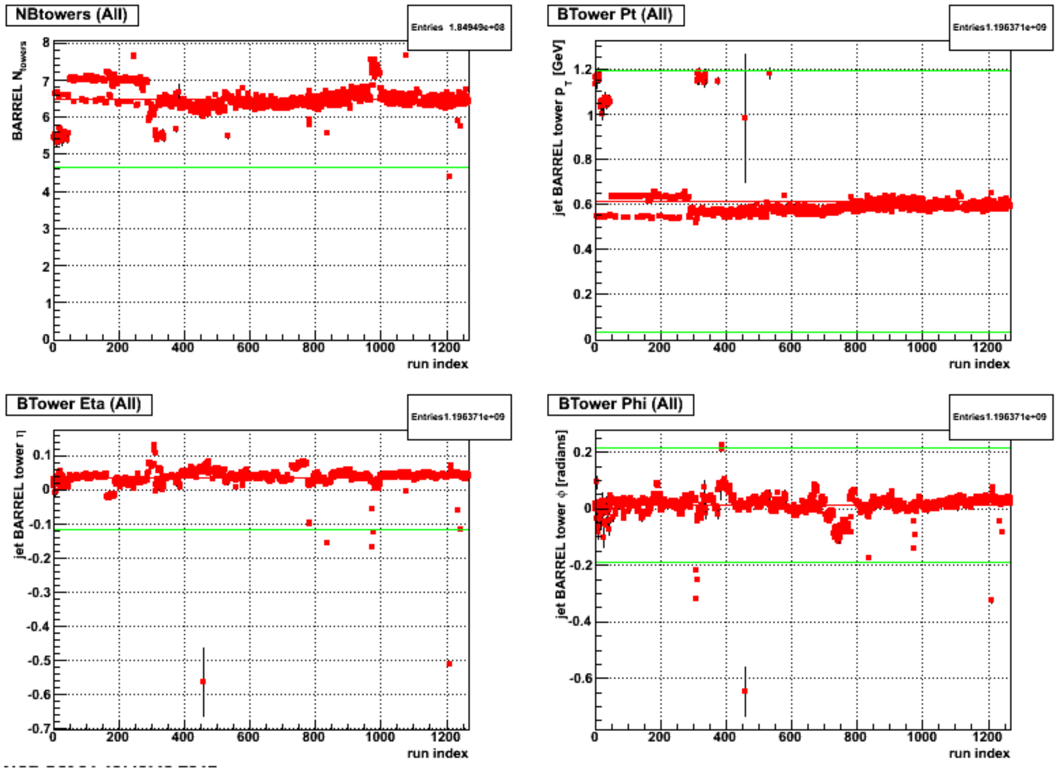

Figure 3.1: QA plot example. Each red point shows the per event mean value of the quantity specified for one run. The red line shows the mean of the points for all runs and the green lines show the $\pm 5\sigma$ lines. Points lying outside the green lines are discarded.

runs were removed, leaving 979 runs.

For the cross section analysis, it was decided that only runs which had a corresponding embedded simulation run (see section 3.5) should be used. Embedded simulation samples were produced for 867 runs; of these, 773 matched a data run which had passed all other QA. These 773 runs were used in the cross section analysis. The complete list, along with a list of fills they are from, can be found in appendix B.

Unlike the cross section analysis, the A_{LL} measurement is statistically limited so it was decided to use all runs from day 120 onward, regardless of whether or not it had an associated embedded simulation run. There were 888 runs used in the asymmetry analysis. The additional runs and fills used in the asymmetry analysis can also be found in appendix B.

3.2 Trigger

STAR, like any other high energy collider experiment, utilizes a sophisticated multi-layer trigger system [54] to select events which may be of interest to various analyses. STAR sees roughly ten million bunch crossings every second, the vast majority of which do not result in a *pp* collision containing an interesting event. In addition, the data acquisition system (DAQ) and some sub-components at STAR run at a much lower rate than the bunch crossing rate. The TPC, for example, can only operate at a rate of several hundred hertz. This means that the STAR trigger system needs to reduce the event rate by roughly five orders of magnitude while also predominantly selecting events which will be useful for future analyses.

The analyses presented in this thesis determine the cross section and spin asymmetry A_{LL} for di-jet final states, so this section will only focus on those triggers which select for jets and dijets. The relevant parts of the trigger system for these analyses are Level-0 and Level-2, which are described in detail below.

3.2.1 Level-0

The first layer of the STAR trigger system is Level-0 (L0) which makes trigger decisions based on energy deposits in fixed regions of the BEMC and EEMC. When triggering on jets, the calorimeter regions of interest are called jet patches. There are 30 jet patches, each of which spanned 1×1 in $\eta - \phi$ space in the Run IX configuration. The trigger logic sums the ADC outputs from all the individual towers which make up each jet patch and compares that ADC sum to a set of thresholds. Table 3.1 shows the approximate transverse energy required in a jet patch in a specific region of the detector in order to pass one of three thresholds.

The L0 trigger logic sets output bits based on which jet patches fired above which thresholds. If any of the 30 jet patches spanning the BEMC and EEMC fire above the highest threshold, the JP2 bit is set. If any of the 30 jet patches fire above the middle threshold,

	TH-0 (GeV)	TH-1 (GeV)	TH-2 (GeV)
BEMC-EEMC-Overlap	3.3	5.0	6.8
BEMC	3.5	5.4	7.3
EEMC	3.1	4.7	6.4

Table 3.1: Approximate transverse energy thresholds for the different jet patches.

the JP1 bit is set. The AJP (described further below) bit is set if two of the 24 jet patches fully contained in either the BEMC or EEMC and adjacent in ϕ fire above the lowest threshold. There are two L0 triggers which are input to the analyses presented in this thesis: JP1 and L2JetHigh. The JP1 trigger contains events for which the JP1 bit is set. The L2JetHigh trigger contains event in which the JP2 or AJP bits are set. L2JetHigh is the input to the jet algorithm at Level-2 which will be described in the next section.

The 1×1 size in $\eta - \phi$ space means that 18 non-overlapping jet patches can fit in the BEMC and EEMC: 6 each in the East and West halves of the BEMC and 6 in the EEMC. Because these jet patches are fixed in the detector, there will be sizable inefficiencies at the jet patch boundaries. A jet which strikes near the boundary of two jet patches and shares its energy between them may not deposit enough in either jet patch to pass threshold. To mitigate this effect in the η direction, two sets of 6 'overlap' jet patches were created. One set straddles the boundary between the jet patches covering a given ϕ range in the East and West halves of the BEMC, which meet at $\eta = 0$, and the other set straddles the boundary between the jet patches in the West half of the BEMC and those in the EEMC, which meet at $\eta = 1$. The 12 additional overlap jet patches give a total of 30 jet patches in the Run IX configuration. Table 3.2 lists the η ranges spanned by the 5 categories of patches. Unfortunately, hardware restrictions prevented the implementation of overlapping jet patches in the ϕ direction as well, but the inefficiencies in ϕ are eased by the Adjacent Jet Patch logic (AJP). AJP fires when two jet patches which are adjacent in ϕ pass the lowest energy threshold. Note: AJP is not implemented for the jet patches which span the BEMC-EEMC boundary.

	η - Position
BEMC-East	$-1 < \eta < 0$
BEMC-Overlap	$-0.6 < \eta < 0.4$
BEMC-West	$0 < \eta < 1$
BEMC-EEMC-Overlap	$0.4 < \eta < 1.4$
EEMC	$1 < \eta < 2$

Table 3.2: The η ranges spanned by the each of the 5 categories of jet patches.

3.2.2 Level-2

The second component of the trigger system that is of interest is the Level-2 (L2) system which is entirely software based and allows for the implementation of more sophisticated triggering algorithms than is possible at L0. The triggers which feed the W or γ analyses, for example, require a single tower to be above some threshold, as well as a cluster of towers around that tower to be above a separate threshold. The single tower condition is handled at L0 whereas the tower cluster condition is implemented at L2. The L2 logic can tag events which pass these more sophisticated requirements and can abort or prescale events which do not.

In addition to the capabilities listed above, the L2 system is useful for monitoring the health of the calorimeters. Many of the L2 trigger algorithms generate diagnostic histograms which are stored in a web-visible location. These histograms provide a convenient way to identify areas of the detector which have stopped working due to hardware failures, or towers which fire at abnormally high rates due to radiation induced stuck bits in the trigger electronics. The L2 histograms can also be used to identify areas of the calorimeters affected by high beam-background rates, which is difficult to do using other diagnostic plots.

The L2 algorithm pertinent to jet and dijet analyses is called L2Jet. The L2Jet algorithm is fed by events which pass the L2JetHigh trigger at L0. Like the L0 jet patch logic, the L2Jet algorithm looks for energy deposits in 1×1 regions in the calorimeters, but because L2Jet is implemented in software it is not restricted to the jet patches set by the L0 trigger hardware. The algorithm first divides the calorimeter into 30 ϕ bins and 15 η bins. These correspond roughly to trigger patches, which (in the BEMC) are 4×4 groupings of individual towers. A 1×1 jet patch corresponds to a 5×5 grouping of $\eta - \phi$ trigger patches. The cylindrical geometry of the detector means that the jet patches can wrap around in ϕ but not in η, so there are 30 unique ϕ configurations and 11 unique η configurations for a total of 330 unique 5×5 areas. This obviously gives much finer granularity than the 30 fixed jet patches available at L0.

L2Jet scans each of these 330 5×5 areas and finds the one containing the most energy. Once this patch is found, the algorithm excludes all patches within 30 degrees and scans all remaining 5×5 areas for the patch with the next highest energy. Thus, for every event passed to L2, the L2Jet algorithm finds the two $1 \times 1 \quad \eta - \phi$ regions of the detector separated in ϕ which contain the most energy. Once these regions have been found, their total energies are compared to a set of threshold values and a trigger decision is made.

The L2Jet algorithm defines three trigger categories: monojet, dijet, and random. The monojet trigger is satisfied if the high patch transverse energy is above the monojet threshold, typically set around 6.5 GeV. The dijet trigger is satisfied if both patch transverse energies are above separate dijet thresholds which are somewhat lower than the monojet threshold. There are three sets of dijet thresholds and which set is used is based on the sum of the energy weighted η positions of the two patches. This functionality was included because jets at forward pseudorapidities tend to have lower transverse energies, so lower thresholds are needed in the forward region to keep the dijet acceptance rate somewhat constant across the detector. The random trigger, as its name suggests, accepts random events at a set rate regardless of whether or not the event would have passed either the monojet or dijet conditions. The random trigger acceptance rate can be set to 100% to force L2Jet to accept all events it sees. A given event can satisfy multiple L2Jet trigger categories simultaneously, but events which don't satisfy any of the above

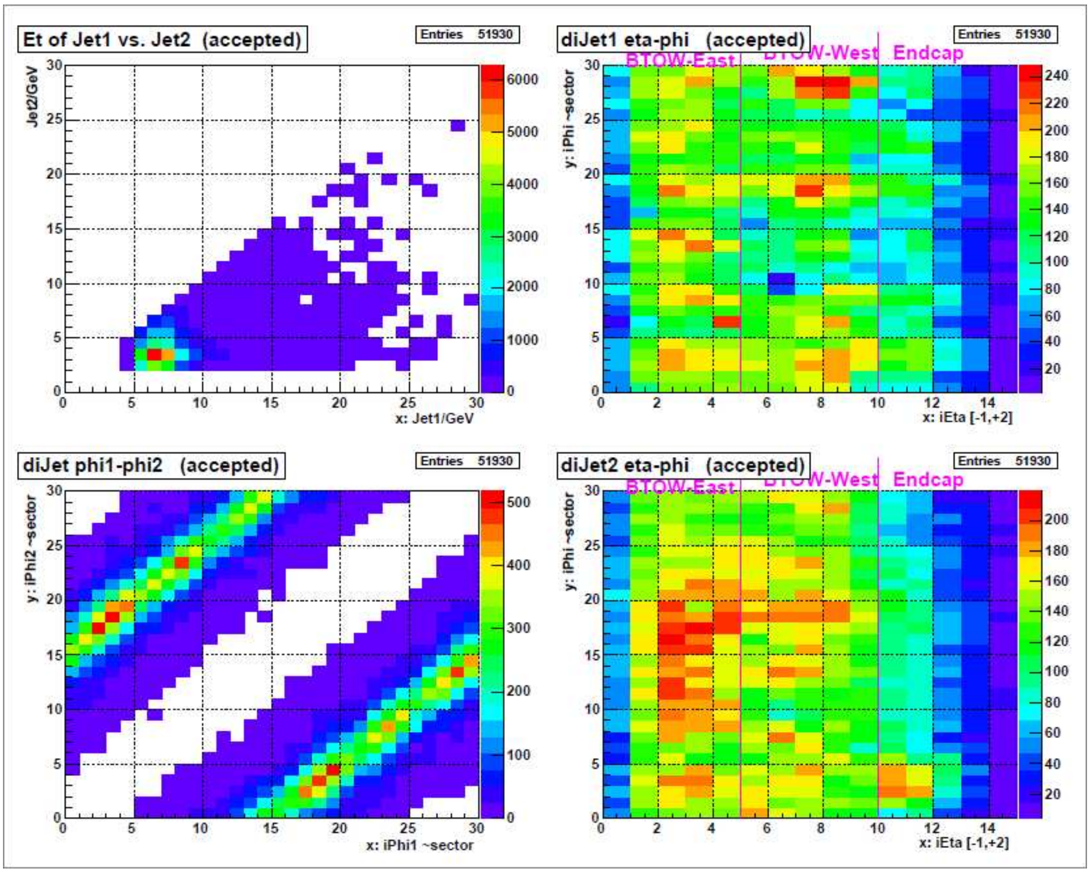

Figure 3.2: Example histograms from the L2Jet algorithm for events passing the dijet condition. Clockwise from upper left: the p_T vs p_T of the two jet patches, the energy weighted ϕ vs η position of the high jet patch, the energy weighted ϕ vs ϕ of the two jet patches, and the energy weighted ϕ vs η position of the low jet patch.

categories are dropped and not used in these analyses. An example of the kinematic distributions of events passing the dijet trigger condition can be seen in figure 3.2.

3.3 Integrated Luminosity

A critical component of the cross section analysis is the determination of the integrated luminosity of the data sample, which is (roughly speaking) a measure of how many collisions could have occurred in the data being analyzed. The integrated luminosity is the integral over time of the instantaneous luminosity, which for a collider setup can be approximately expressed as [55]:

$$\mathcal{L} = f\frac{N_1 N_2}{4\pi\sigma_x\sigma_y} \tag{3.1}$$

where f is the bunch collision frequency, $N_{1(2)}$ are the number of protons in each bunch, and $\sigma_{x(y)}$ are the transverse profiles of the bunches. The dimensions of $\mathcal{L}$ are $\mathrm{cm}^{-2}\mathrm{s}^{-1}$ meaning that the integrated luminosity has dimensions of cm^{-2}.

The cross section (σ) for a given final state is proportional to the probability that a single collision will produce said final state. Thus, if a final state is observed N times, that number needs to be normalized by the integrated luminosity in order to determine the cross section. The relationship can be written as [55]:

$$\sigma = \frac{N}{\int \mathcal{L}(t)\mathrm{d}t} \tag{3.2}$$

The form of equation 3.2, with the integrated luminosity as a known quantity, is essentially what is used later in this dissertation to find the di-jet cross section. If there is some other process for which the cross section has previously been determined, the above equation can be inverted to find the integrated luminosity. At STAR, the absolute BBC trigger cross section has been determined using the Vernier Scan technique [56] and has a value of $26.1 \pm 0.2(\mathrm{stat}) \pm 1.8(\mathrm{sys})$ mb [57]. Thus, the integrated luminosity of the data sample can be found by counting the number of BBC coincidence triggers and scaling by the absolute BBC cross section.

There are two factors which need to be taken into account when using the BBC to determine the integrated luminosity: dead time and prescale. The L2JetHigh and JP1 L0 triggers have an associated dead time which is related to the detectors which these triggers read out. The BBC coincidence trigger which is used in the integrated luminosity determination must have the same dead time conditions as the jet triggers, or it won't sample the same events seen by the jet triggers. The BBCMB-Cat2 trigger was set up so as to have the same dead time conditions as the L0 jet triggers and is thus used to determine the integrated luminosity. The second issue which needs to addressed is the prescale associated with the BBCMB-Cat2 trigger. The number of BBCMB-Cat2 triggered events recorded in the data files is actually scaled by a factor of 1.0×10^5 from the scalar system. The number of BBCMB-Cat2 triggers must be multiplied by this prescale factor to get the actual number of BBC coincidence events needed in order to find the integrated luminosity.

The integrated luminosity of the data set used in the cross section measurement was determined to be 17.1 pb^{-1}. The integrated luminosity of the data used in the A_{LL} analysis was determined to be 19.5 pb^{-1}.

3.4 Average JP1 Pre-Scale

The JP1 trigger was satisfied at a lower energy threshold and thus fired at a higher rate than the L2JetHigh trigger. In order to keep the JP1 trigger from filling up the available trigger bandwidth, it was prescaled throughout the run. The prescale factor changed from run to run based on a measure of the instantaneous luminosity seen at STAR at the beginning of that run. This prescale factor must be taken into account in the calculation of the JP1 cross section, to convert from the number of events seen to a 'true' number of events produced from the *pp* collisions. (Note: the L2JetHigh trigger was always take-all, that is, not prescaled at all).

Because the JP1 prescale factor changed from run to run, it is the event-weighted average prescale which must be used in the determination of the cross section. The average prescale was found by summing the prescale factors of all events firing the JP1 trigger and dividing by the total number of JP1 events. All JP1 events entering the analysis were used in the determination of the average prescale whether or not that event yielded a di-jet.

The properly weighted average JP1 prescale for the data sample was found to be 5.16

3.5 Simulation Studies

Accurate simulation is vital to both the cross section and A_{LL} analyses, to correct for various detector effects so that comparisons to theory can be made. The simulation sample used in this thesis was originally produced for the 2009 inclusive A_{LL} analysis.

The simulation sample consisted of roughly 21 million pp collisions at $\sqrt{s} = 200$ GeV generated using the Pythia [58] event generator in ten separate partonic p_T bins. Version 6.426 of Pythia with the Perugia 0 tune [59] was used. The response of the STAR detector to the Pythia events is modeled using the GSTAR package which is based on GEANT 3 [60]. The Pythia events are also embedded into real zero bias events to simulate the effect of pileup. These zero bias events were acquired by triggering the STAR detector on random bunch crossings, and were taken from the same runs that were used in the analysis in order to accurately simulate the detector conditions throughout the run. The simulation is broken into individual runs, and the embedding files used in that simulation run are taken from the corresponding data run so that a given simulation run will match the detector conditions seen during that data run.

A significant amount of computing time is needed to fully simulate the STAR detector response to a Pythia event. In order to reduce the amount of time needed to run the simulation, a trigger filter was used. The trigger filter rejects events which would not have fired the JP1, AJP, or BHT3 (BHT3 is a Barrel high tower trigger) triggers before the detector response is simulated. The trigger filter rejected roughly 91.5% of all Pythia events; however, the full Pythia record for the rejected events is saved so that corrections to the unbiased sample can be made. The embedded simulation would have taken a prohibitively long time to generate without the use of the trigger filter.

3.5.1 Three Levels of Simulation

The simulation consists of three distinct levels of information corresponding to the partonic hard scattering, the hadronization of the scattered partons, and the response of the detector to the final state particles. These divisions will be referred to as the parton level, particle level, and detector level, respectively.

The parton level of the simulation contains information about the partons involved in the $2 \rightarrow 2$ hard scattering event generated by Pythia. Various kinematic properties of the hard scattering, such as the Q^2, center of mass scattering angle, and momentum fractions of the incoming partons are stored. When the jet finder is run on the parton level of the simulation, only the partons involved in the hard scattering and partons which arise from initial or final state radiation are included. Partons arising from the underlying event or beam remnant are not included in the parton-level jet finding.

The partons generated by Pythia propagate and hadronize to form stable, color-neutral particles. The particle level of the simulation records the kinematic information, particle id, and index of the parent parton for all of these stable particles. When the jet finder is run on the particle level, all stable particles are used, including those which arise from the underlying event and beam remnant.

The last level of the the simulation records the detector response to the stable particles from the previous level. As the particles traverse the GSTAR model of the detector, they interact with the various volumes in ways consistent with how that particular particle would behave in a specific material. This interaction includes ionizing the gas in the TPC and depositing energy in the scintillator of the calorimeters. This, along with a simulation of the detector readout electronics, allows the simulation to respond to particles as the real detector would. When the jet finder is run on the detector level simulation, it constructs jets from the simulated response of the TPC and calorimeter towers, and their readout electronics.

3.5.2 Z-Vertex Correction

The simulated events are thrown with some distribution of z-vertex position which may not exactly match the z-vertex distribution of the data. In order to achieve the best matching between the data and simulation, the z-vertex distribution of the simulation should be altered to match that of the data. This is done by re-weighting the simulation. The re-weighting is performed separately for the two trigger categories used in the cross section analysis, and is only performed on the simulated events which pass the trigger filter and undergo the full detector reconstruction.

The re-weighting is done by taking the ratio of the z-vertex distribution observed in the data to that of the simulation. This ratio is then fit with a 4^{th} order polynomial, as shown in figure 3.3. When the simulation is used in the analysis, the function which fits the ratio is evaluated at the z-vertex of the simulated event and the value returned is multiplied by the weight associated with the partonic p_T bin in which the simulated event was generated. Figure 3.4 shows the z-vertex distributions from data and simulation after the z-vertex re-weighting has been applied.

It should also be noted that there is a matching condition placed on the z-vertices from the particle / parton level and the detector level. The vertex associated with the particle / parton level is the one which is set when Pythia is run, whereas at the detector level the vertex is found by emulating the vertex finder which is run on the actual data. This can cause a small difference between the vertex position at the particle / parton and detector levels. The fact that the simulation is embedded into physical zero-bias events can also change the detector level vertex position as more tracks are added to the event. Once in a while a zero-bias event will contain an actual hard scattering event, and the vertex of that event will be used as the detector level vertex, causing a large mismatch between the particle / parton vertex and the detector level vertex. To avoid these cases, only simulated events where the particle / parton level z-vertex and detector level z-vertex are within two centimeters are used, see figure 3.5.

3.5.3 Data - Simulation Comparison

In order to be useful for correcting detector effects, the simulated detector response must closely match the actual data for the quantities and kinematic regions of interest. The

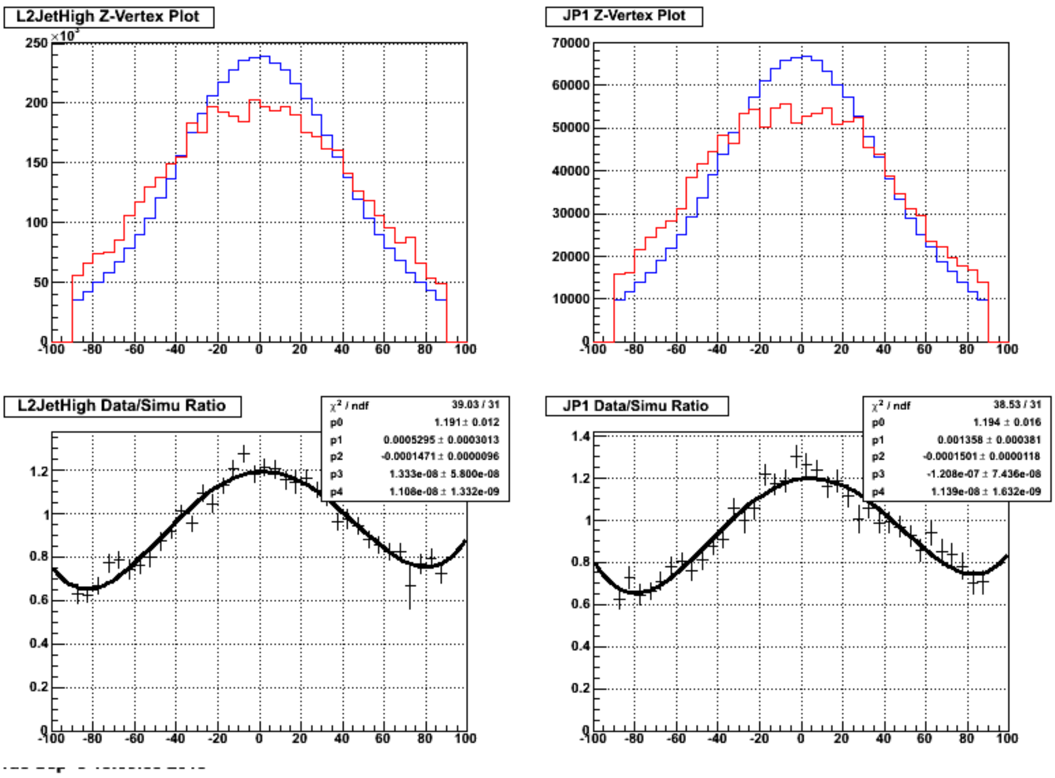

Figure 3.3: z-vertex distributions from the data (blue curves) and the simulation (red curves) for the L2JetHigh (left) and JP1 (right) trigger categories. Also shown are the data / simulation ratio fit with a 4^{th} order polynomial.

main kinematic quantity used in these analyses is the di-jet invariant mass. The di-jet mass depends mainly on the p_T of the two jets, the difference in pseudorapidity, and the difference in azimuthal angle between the two jets. Figures 3.6, 3.7, and 3.8 show the comparisons between data and simulation for these quantities. Figures 3.9 and 3.10 show the comparisons between data and simulation for the jet pseudorapidity and jet azimuthal angle distributions. The good agreement found between data and simulation for jet η and ϕ show that the detector conditions are well matched in the simulation, as the ϕ spectrum in particular is sensitive to hardware failures in the TPC. Finally, figure 3.11 shows the comparison between the di-jet invariant mass as measured in data and in the embedded simulation, and very good agreement is seen. This gives confidence that the response of STAR is well understood, including the effects of hardware problems.

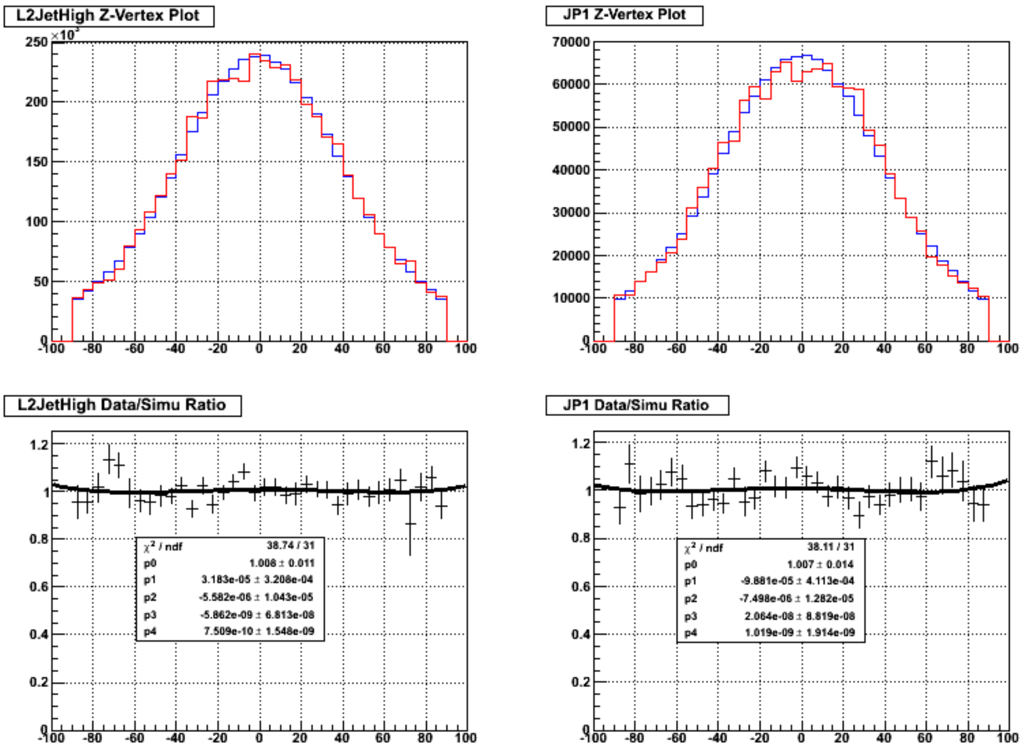

Figure 3.4: z-vertex distributions from the data (blue curves) and the simulation (red curves) after the vertex re-weighting has been applied.

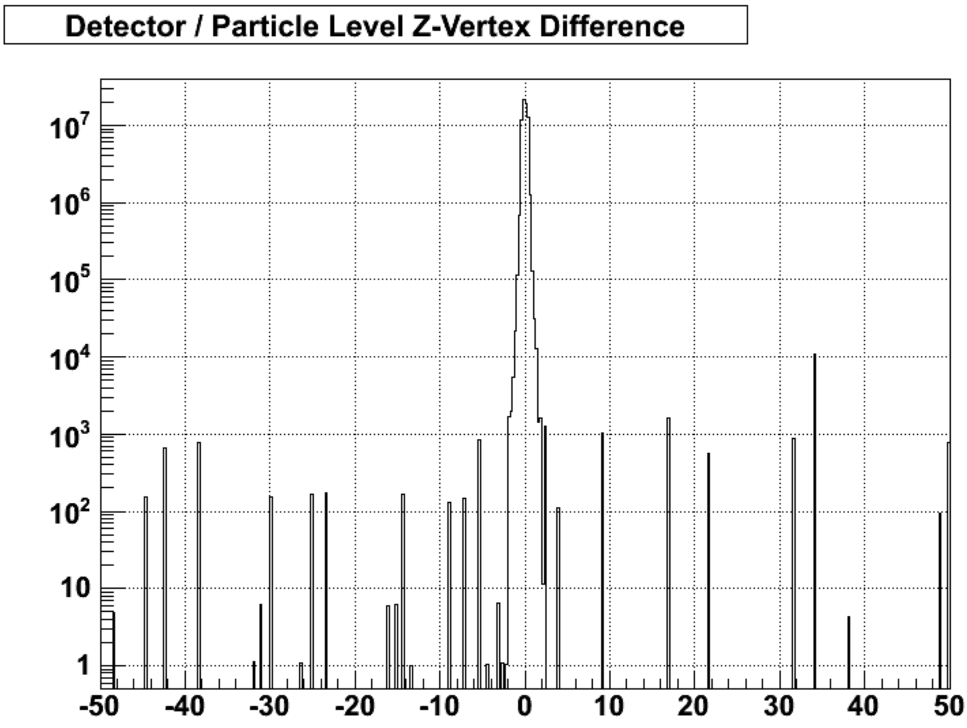

Figure 3.5: Difference in z between the particle level vertex and the detector level vertex.

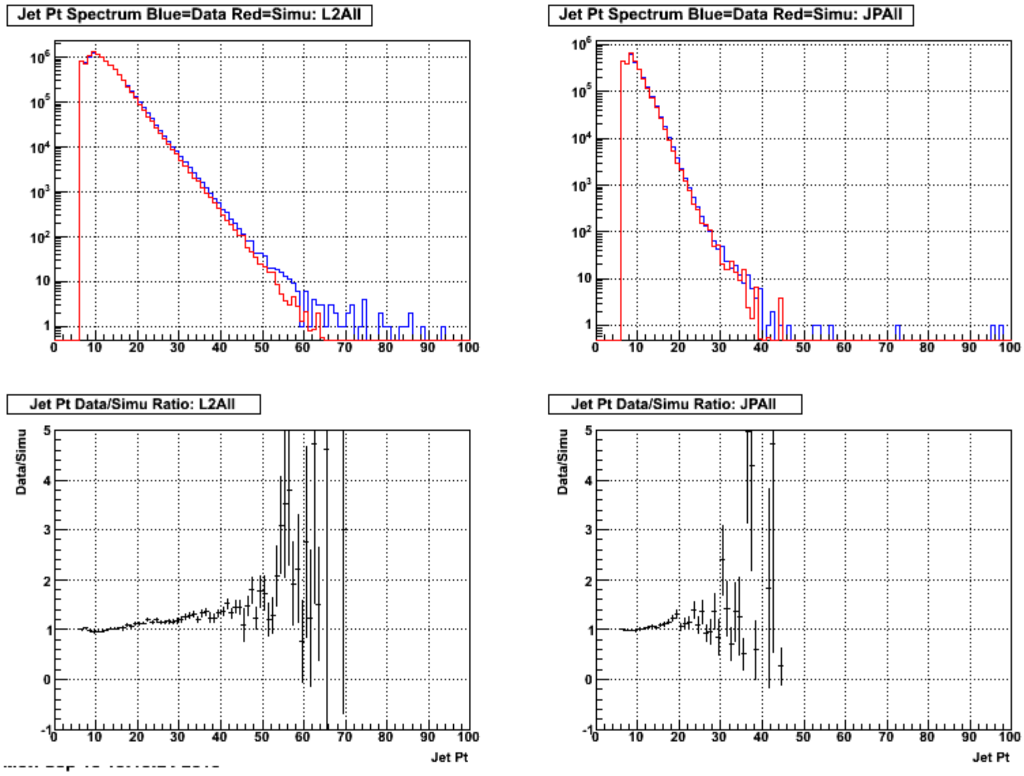

Figure 3.6: Data / simulation comparisons for the jet transverse momentum.

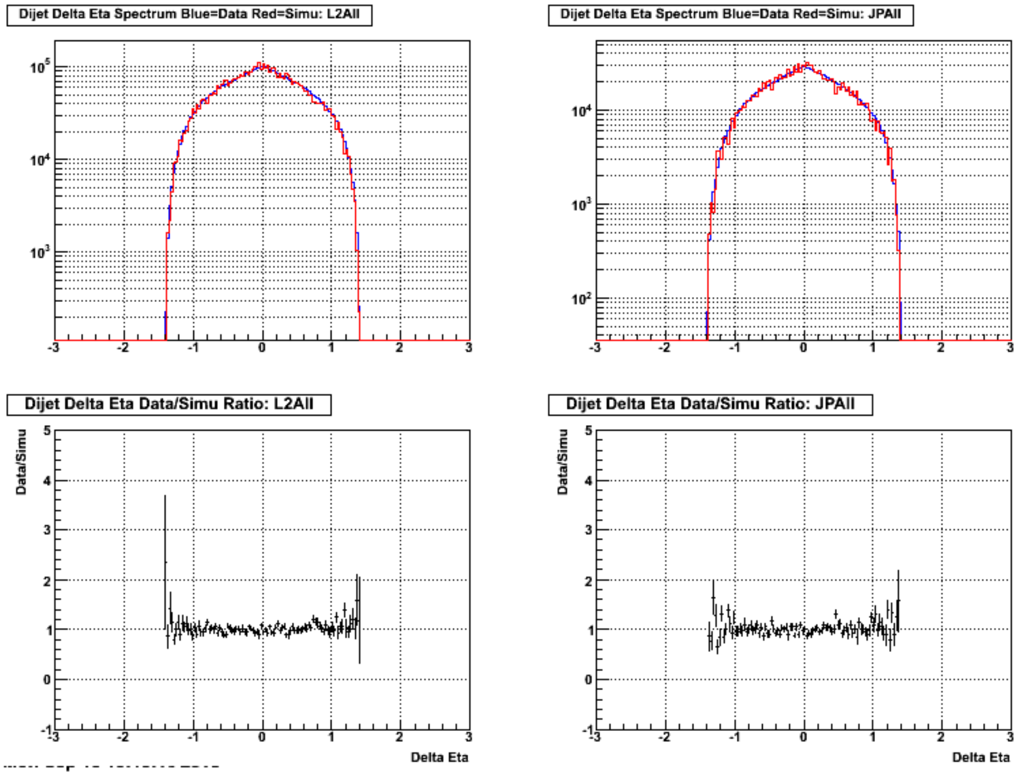

Figure 3.7: Data / simulation comparisons for the di-jet pseudorapidity difference.

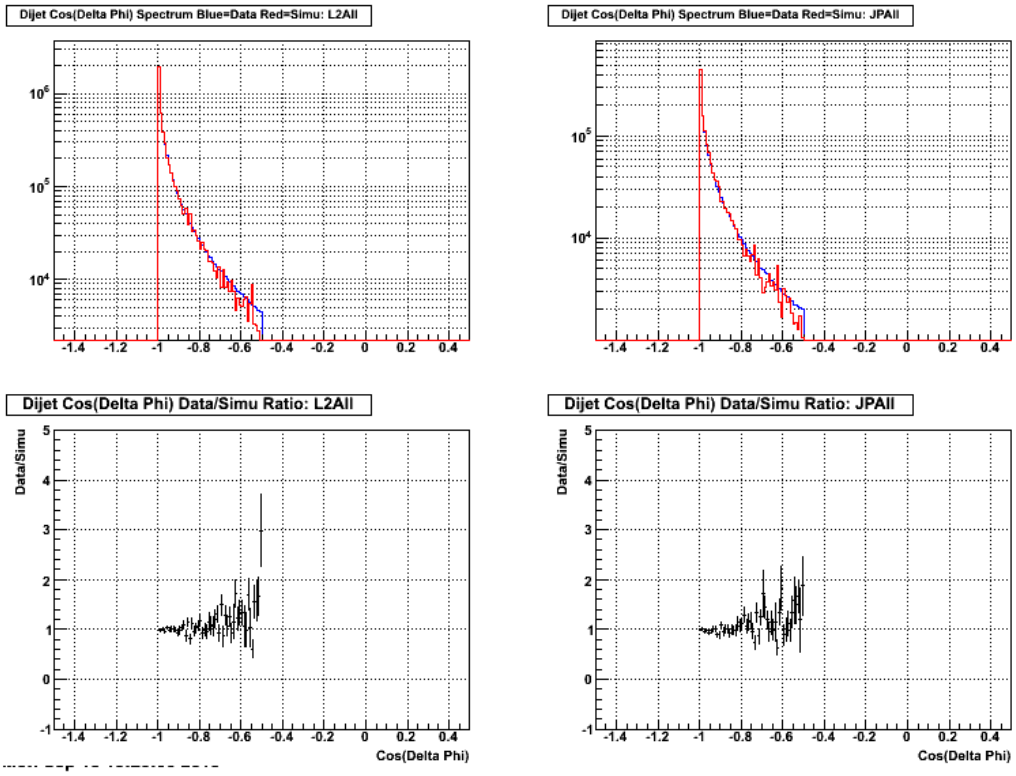

Figure 3.8: Data / simulation comparisons for the cosine of the di-jet azimuthal angle difference.

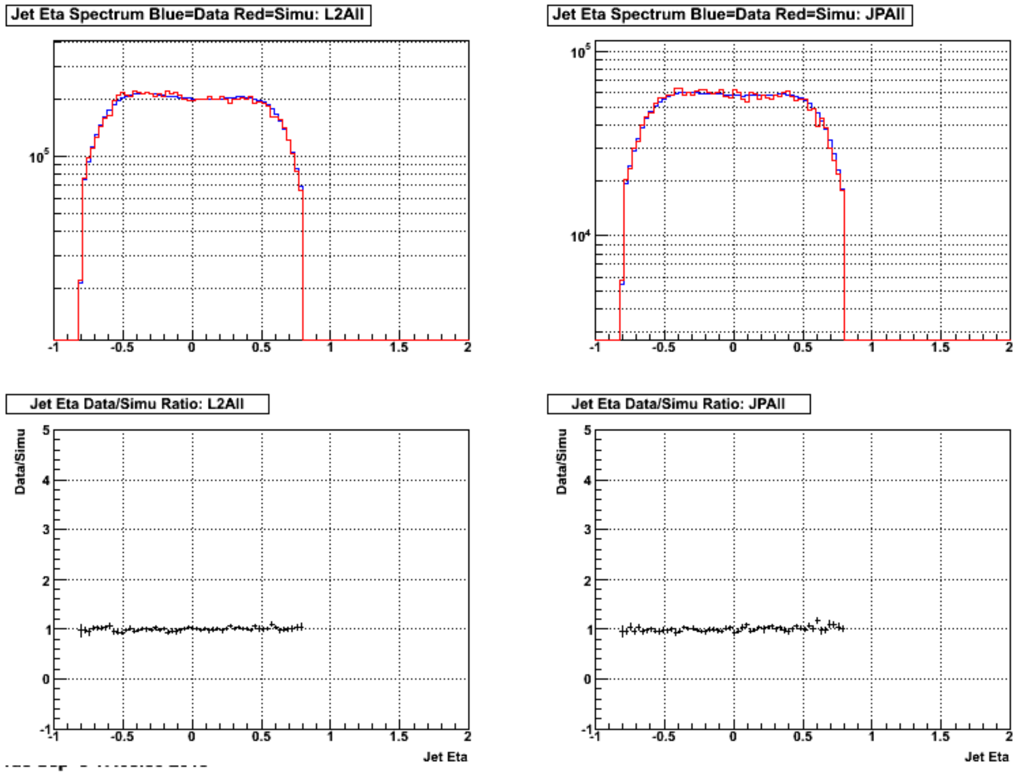

Figure 3.9: Data / simulation comparisons for the jet pseudorapidity.

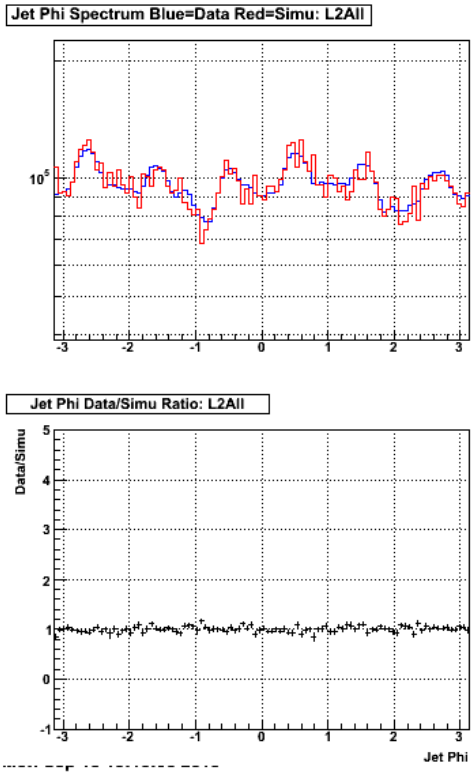

Figure 3.10: Data / simulation comparisons for the jet azimuthal angle.

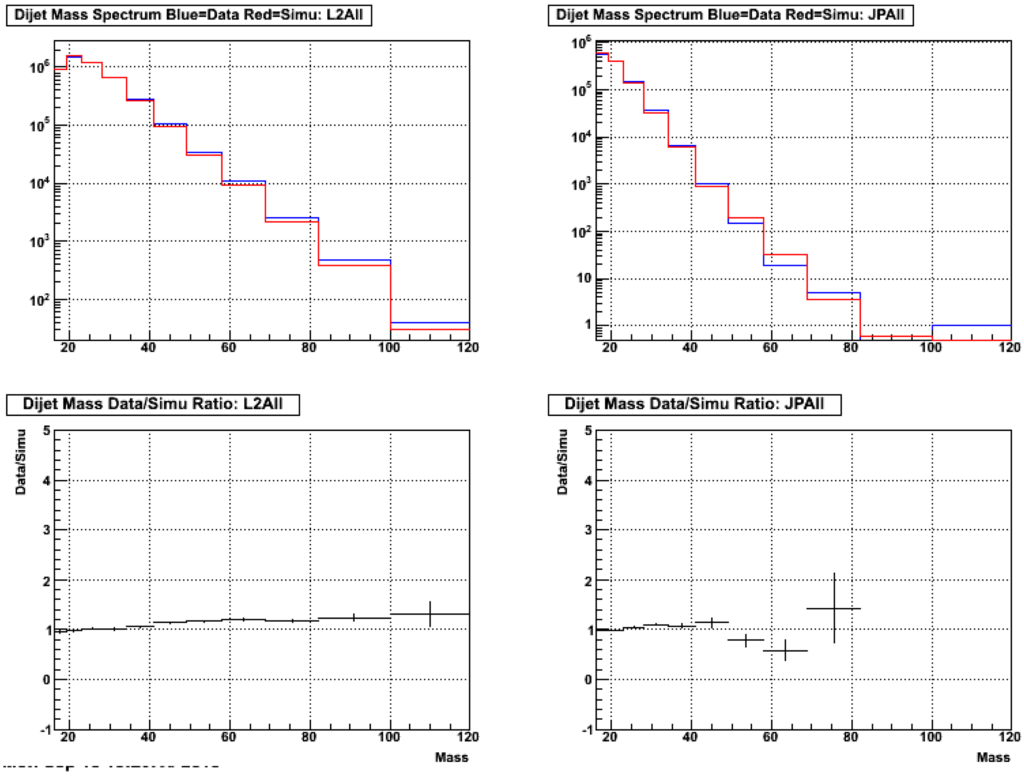

Figure 3.11: Data / simulation comparisons for the di-jet invariant mass.

Chapter 4

Jet and Di-jet Reconstruction

The existence of jets with large transverse momenta as a final state in proton-proton collisions was an early prediction of the parton model of nucleon structure [61]. If protons contained hard, point-like partons, then in some fraction of high energy *pp* collisions two partons from the colliding protons should scatter and be ejected with significant momentum transverse to the collision axis. A jet is a collimated spray of particles which arises from the fragmentation and hadronization of one of these hard scattered partons, either a quark or gluon. Jets also arise from the fragmentation of quarks produced in e^+e^- collisions and in the decay of highly boosted massive particles, but those processes and the techniques used in the analysis of those jets will not be discussed here.

This chapter describes the algorithms used to find jets at STAR in *pp* collisions, the specific requirements on tracks and towers used in jet finding, and the selection criteria and cuts used to select two-jet final states (di-jets). Good overviews of different jet algorithms and jet finding in general can be found in [62] and [63]. A historical overview of the role jets have played in the development of QCD can be found in [64].

4.1 Jet-Finding Algorithms

Unlike individual particles which have a well defined mass that can aid in identification, jets are somewhat ill-defined objects. The fragmentation of a quark or gluon into hadrons can proceed in a large number of ways, leading to jets that have different particle content, momentum distributions, and spacial extent. To be useful in a quantitative analysis, there must be a well defined procedure for determining which particles should be grouped together into a jet. The method needs to be flexible enough to handle the variations in event characteristics mentioned above. The procedure used to group (or exclude) particles into jets is known as a jet algorithm.

In addition to the jet algorithm, which provides a set of rules for grouping individual particles into jets, there is always an associated recombination scheme which defines how to build the momentum of combinations of particles from the momenta of the individuals. The most intuitive recombination scheme is simply the addition of individual 4-momenta and is known as the E-scheme but there are other prescriptions for combining particle momenta [63]. This thesis will deal only with the E-scheme. The combination of a jet algorithm and a momentum recombination scheme is called a jet definition and, as the name implies, fully defines a jet for the purpose of an analysis.

The goal of most analyses is to relate the final jet observables measured by the detector to some underlying partonic interaction, and thus enable comparison to a theoretical prediction or model. In order to make these comparisons in a rigorous way, a jet definition should work on detector tracks and towers, individual particles or partons from Monte Carlo simulation, or fixed-order perturbative calculations with little or no modification needed to handle the different input. In addition, a good jet definition should be insensitive to infrared radiation and collinear emission (IRC). Collinear emission occurs when a hard particle splits into two lower energy particles which travel in very nearly the same direction as the original. Infrared radiation refers to the emission of low energy particles from a higher energy particle. These affects will not change the number or the kinematics of jets found by an IRC-safe jet definition. The IRC safety of a jet definition is an important factor in the rigorous comparison of jets found in data, simulation, and theory.

Further details on the IRC safety of several of the most commonly used jet algorithms, along with basic descriptions of their function, can be found here [63].

There are many jet algorithms available, but they all generally fall into two broad categories: cone algorithms and sequential recombination algorithms. Previous STAR analyses have used a cone algorithm (specifically the midpoint cone algorithm) [26], [28]. Starting with analysis of Run IX data, STAR has begun using the anti-k$_t$ algorithm which, unlike most cone algorithms, is IRC safe at all levels of perturbation theory.

4.1.1 Anti-k$_t$ Algorithm

The anti-k$_t$ algorithm [65] belongs to the broader class of sequential recombination algorithms which repeatedly combine pairs of particles which are closest to each other as determined by some distance criterion. This thesis utilizes the anti-k$_t$ algorithm as it is implemented in the FastJet [66] software package. FastJet provides a simple interface for several jet algorithms, and also leverages geometrical considerations to greatly enhance the speed of jet-finding for sequential recombination type algorithms (the time to run basic anti-k$_t$ scales as N^3, where N is the number of particles; the run time of the FastJet implementation scales like $N \log N$).

The anti-k$_t$ algorithm defines two distance measures:

$$d_{ij} = min\left(p_{ti}^{-2}, p_{tj}^{-2}\right) \frac{\Delta R_{ij}^2}{R^2} \tag{4.1a}$$

$$d_{iB} = p_{ti}^{-2} \tag{4.1b}$$

where $\Delta R_{ij}^2 = (y_i - y_j)^2 + (\phi_i - \phi_j)^2$ with p_{ti}, y_i, and ϕ_i being the transverse momentum, rapidity, and azimuthal angle of particle i. The R term sets the approximate size of the jets in $\eta - \phi$ space and how close two jets can be. In these analyses, R is set to 0.6. Using the two definitions above, the anti-k$_t$ algorithm works as follows [63]:

1. Find d_{ij} and d_{iB} for each particle and all particle pairs
2. Find the minimum of the d_{ij} and d_{iB}

3. If the minimum distance measure is a d_{ij}, combine particles i and j into a single new particle and return to step 1
4. If the minimum distance measure is a d_{iB}, then particle i is a final state jet and is removed from the list of particles. Return to step 1
5. Stop when all particles are included in final state jets

The anti-k$_t$ algorithm behaves much like an iterative cone algorithm while avoiding the IRC safety issues which often arise with those algorithms. Because the p_t factor in the d_{ij} measure comes in the denominator, the d_{ij} value for a hard particle and a nearby soft particle will always be smaller than that for two similarly separated soft particles. This means that soft particles will tend to cluster with hard particles before they cluster with other soft particles.

4.2 Jet-Finding Conditions

As mentioned above, the analyses in this thesis utilize the anti-k$_t$ jet algorithm with a radius parameter of 0.6. In addition to the parameters native to the jet algorithm, there are a number of conditions placed on the TPC tracks and calorimeter towers which are used as input to the jet algorithm at the detector level. There are also a number of cuts placed on the jets used in the analyses.

4.2.1 Track Conditions

The TPC tracks must pass the following conditions in order to be used in the jet finding:

- Track p$_T$ > 0.2 GeV/c
- Track pseudorapidity between ±2.5
- Number of padrow hits > 5
- Number of padrow hits divided by number of possible hits > 0.51
- Transverse momentum-dependent Dca cut

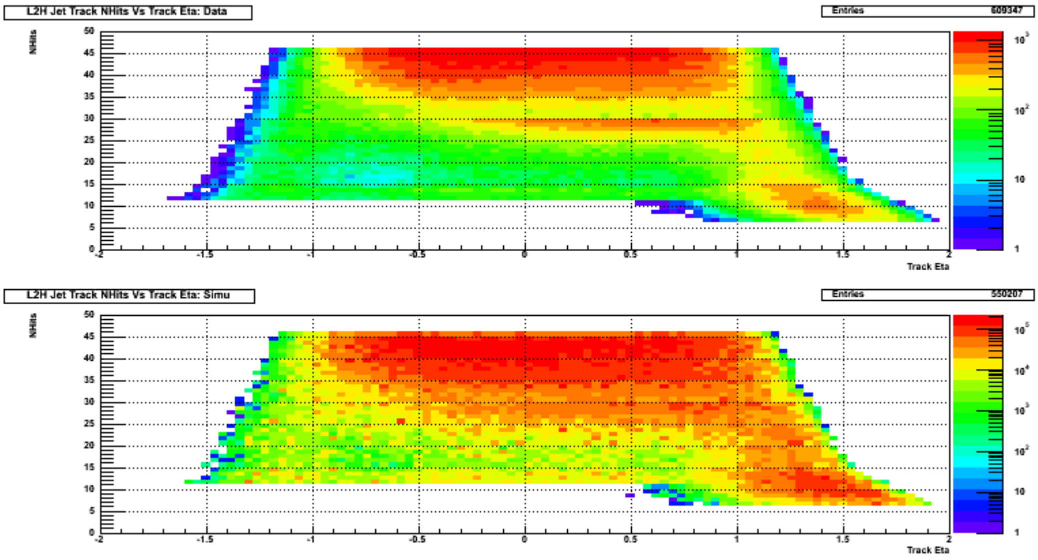

Figure 4.1: Number of padrows hit by tracks at a given track pseudorapidity. The pseudorapidity region where 5-point tracking is implemented is visible for NHits < 12 and η greater than 0.5. The top panel is data and the bottom panel is simulation.

The requirements on track p_T and η are self explanatory, and are meant to remove tracks which are too soft or tracks which will fall too far outside the TPC acceptance. The tracks used in jet finding must also be constructed from more than five hits in the TPC padrows. This cut is meant to ensure that there is enough information to adequately determine the track momentum. Previous STAR jet analyses required tracks to contain more than twelve hits in the padrows but this condition was relaxed here in anticipation of extending these analyses into the Endcap. Note: the 5-point tracking does not extend over the full TPC, it is only implemented for tracks with $\eta > 0.6$ (see figure 4.1).

The DCA (distance of closest approach) is the distance between the event vertex and the charged particle track trajectory at the point when the trajectory is closest to the vertex. The p_T dependent DCA cut rejects tracks which have a 3-D DCA greater than or equal to 2 cm if the track has a p_T less than 0.5 GeV/c, and tracks with a DCA greater than or equal to 1 cm if the track has a p_T greater than 1.5 GeV/c. The cut is linearly interpolated between p_T of 0.5 and 1.5 GeV/c.

4.2.2 Tower Conditions

As with TPC tracks, there are several conditions the calorimeter towers must satisfy to be included in the jet-finding:

- Tower transverse energy $>$ 0.2 GeV
- Tower ADC > 4
- Tower ADC $> 3\times$ RMS
- Hadronic subtraction scheme

As with the cut on track p_T, the tower transverse energy (E_T) cut is meant to remove very soft towers, and the ADC conditions ensure that the tower signal is not from the pedestal. The hadronic subtraction scheme is designed to prevent double counting the contributions from tracks and towers. The hadronic subtraction removes 100% of the p_T of a track from the tower that the track points to. If the track p_T is greater than the transverse energy of the tower, the tower E_T is set to zero.

4.3 Di-jet Selection and Cuts

Di-jets are two jets which arise from the same partonic hard scattering event and are the focus of this thesis. It is important to fully specify how di-jets are selected from the many jets which may be reconstructed in any given event, as applying the cuts in different orders may lead to different individual jets being identified as the di-jet. The steps used to determine which jets in an event will be identified as a di-jet candidate are (in order):

1. Select the highest ranked vertex in event (vertex must have rank > 0)
2. Require this vertex to have $|z| < 90$cm
3. Select all jets satisfying $-0.8 \leq \eta \leq 1.8$ and $-0.7 \leq$ detector $\eta \leq 1.7$
4. Select the two highest p_T jets

5. Require that at least one jet points to a jet patch which fired either the L2JetHigh or JP1 L0 trigger

The two jets selected using the steps above define a di-jet candidate. There is only one di-jet candidate defined per event, even if the event contains enough individual jets to construct more di-jet pairs. The candidate di-jets constructed using the procedure above must pass a number of further conditions to be used in the analyses:

- Opening angle cut: $\cos(\Delta\phi) \leq -0.5$
- Neutral fraction cut: At least one jet must have a neutral fraction < 1.0
- Asymmetric p_T cut: High p_T jet ≥ 8.0 GeV/c and low p_T jet ≥ 6.0 GeV/c
- Jet fiducial cut: $-0.8 \leq \eta \leq 0.8$ and $-0.7 \leq \text{detector} \quad \eta \leq 0.7$
- p_T balance cut

The two jets arising from a partonic hard-scattering event should be roughly back-to-back in azimuth (ϕ). Jets which are close to each other in azimuth likely do not represent the $2 \rightarrow 2$ scattering. To remove these events from the analysis, an opening angle cut was placed on the two jets included in the di-jet such that the azimuthal angle between them must be 120 degrees or greater. This requirement is illustrated in figure 4.2.

Previous inclusive jet analyses have used neutral energy conditions to remove jets comprised primarily of background energy with no associated tracks. The cut was usually placed such that jets with greater than 95% of their p_T coming from the calorimeter towers are rejected. This kind of cut is not useful when studying jets in the EEMC because the falling TPC efficiency means that jets in this region will have few tracks and therefore large neutral fractions. It is unlikely that a background jet will be coincident with a physics jet, so instead of putting a neutral energy cut on the individual jets, the requirement can be loosened so that only di-jet candidates where both jets have neutral fractions of 100% are rejected, as shown in figure 4.3.

Theoretical calculations of di-jet quantities require an asymmetric cut on the transverse momenta of the two jets. Generally, the lowest p_T jets should differ by 2 GeV/c. To be able to compare to theory, an asymmetric p_T cut is placed on the data and simulation. The high p_T jet must have a p_T greater than or equal to 8 GeV/c and the low p_T jet must have a p_T greater than or equal to 6 GeV/c.

The cuts listed above have been designed so that they can be applied to future forward di-jet analyses. The analyses detailed here deal only with the mid-rapidity region however, so cuts are placed to restrict the jet pseudorapidity to between -0.8 and 0.8 and the jet detector pseudorapidity to between -0.7 and 0.7.

Plotting the p_T of one jet vs the p_T of the other jet in di-jet events reveals 'tails' of events with highly unbalanced p_T's (see figure 4.4). The jets in these tails have been shown to be dominated by single tracks with very high p_T. These tracks are uniformly distributed throughout the TPC, and are likely a result of finite resolution in the measurement of track curvature. These high p_T tracks are not a result of physics processes, so the jets which contain them should be removed from the analysis. This is done with a two-step process. First, jets which contain a track with $p_T \geq 30$ GeV are flagged. Next, the p_T's of the two jets from events in which one (or both) of the jets was flagged are compared and the event is excluded from the analysis unless the jet p_T ratio is between 2/3 and 3/2. Figure 4.4 shows the effect of this p_T balance cut.

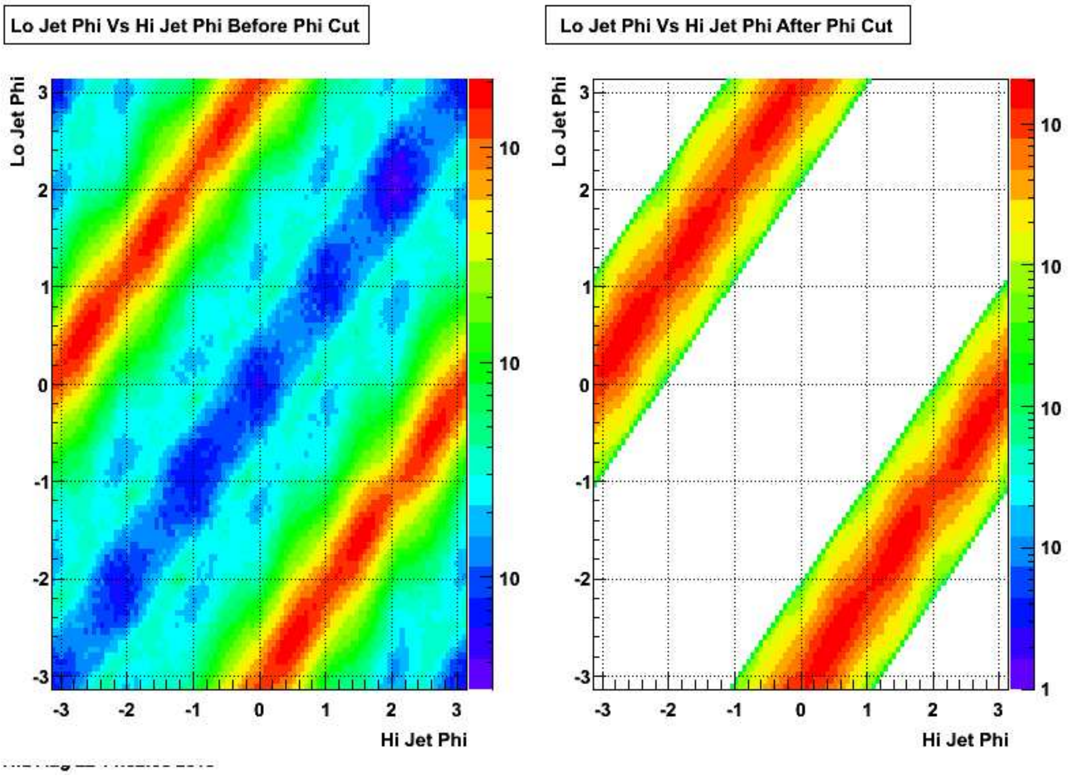

Figure 4.2: The left panel shows the jet-ϕ vs jet-ϕ correlation for di-jet candidates before the azimuthal opening angle cut was applied. The right panel shows the same correlation after the cut is applied.

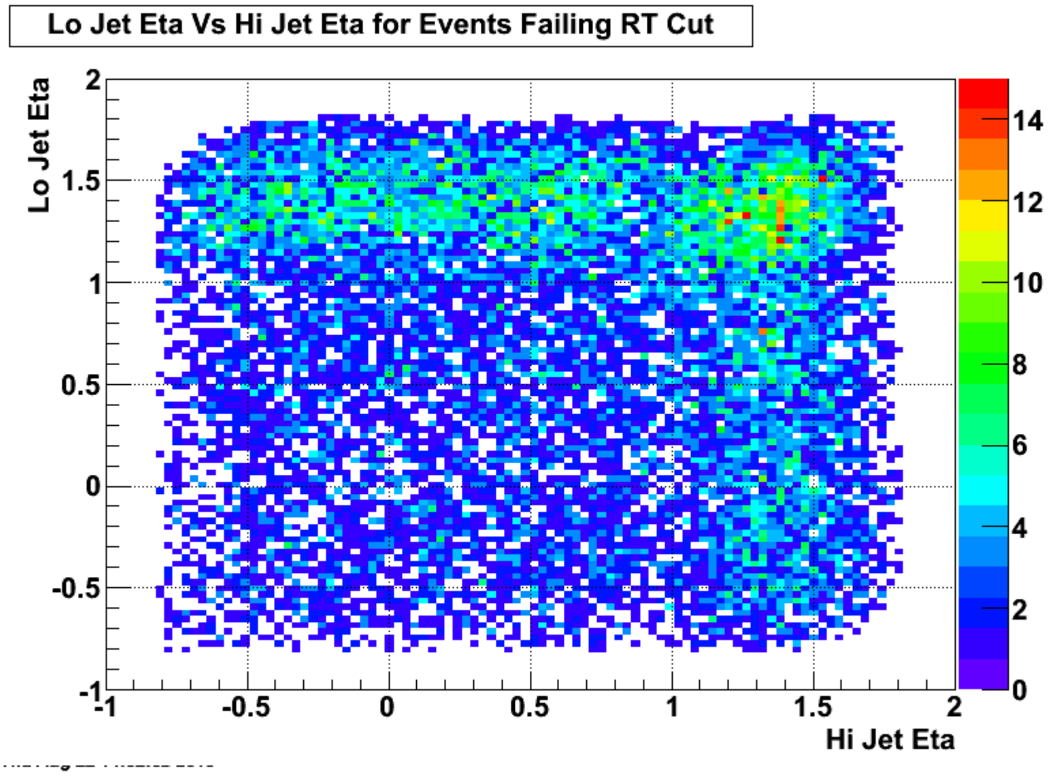

Figure 4.3: Pseudorapidity of the low p_T jet vs. that of the high p_T jet for di-jet candidates which fail the neutral fraction cut.

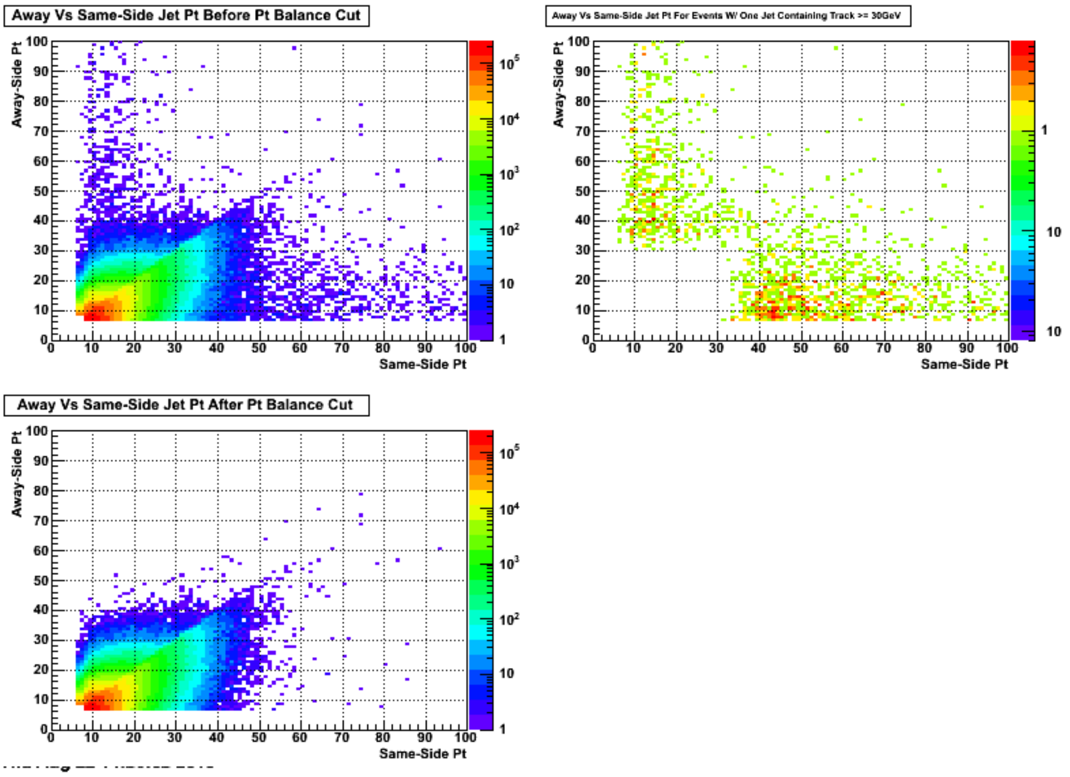

Figure 4.4: Effect of the p_T balance cut. The top left panel shows the away vs same-side jet p_T for di-jet candidates before the balance cut is applied. The top right panel shows the p_T's for di-jet candidates in which at least one jet has a track with $p_T \geq 30$ GeV. The bottom left panel shows the p_T's for events which pass the balance cut.

Chapter 5

Di-jet Cross Section

This chapter presents the mid-rapidity di-jet cross section as a function of invariant mass measured at STAR at $\sqrt{s} = 200$ GeV from the L2JetHigh trigger sample (described in section 5.1). Di-jet production is a QCD process, and so the cross section should be calculable from that theory when one is in the perturbative regime, where the strong coupling constant is small. Thus, a measurement of the di-jet cross section can be used to test the validity of the perturbative QCD (pQCD) framework. However, the applicability of pQCD at RHIC kinematics has previously been verified by inclusive jet [25] and pion [67] [68] cross section measurements, so good agreement between the measured cross section and theory serves to show that detector and jet reconstruction effects are well understood for the di-jet observable at STAR.

The differential cross section in a particular invariant mass bin is given by the following formula:

$$\frac{\mathrm{d}^2\sigma}{\mathrm{dMd}\eta} = \frac{1}{\Delta\mathrm{M}\Delta\eta}\frac{<\mathcal{P}>}{\mathcal{L}}\mathrm{J} \tag{5.1}$$

The ΔM and $\Delta\eta$ terms give the phase space volume, with ΔM being the width of a given invariant mass bin and $\Delta\eta$ being the allowed jet pseudorapidity range, which is 1.6. The $<\mathcal{P}>$ term is the average prescale for the JP1 trigger as discussed in section 3.4. This term is set to unity for the L2 trigger sample as the L0 L2JetHigh trigger was take-all throughout the run. The $\mathcal{L}$ term is the integrated luminosity of the data sample, as discussed in section 3.3. Finally, J is the corrected yield in a given mass bin. J is

Bin	Mass Range (GeV)	$\frac{1}{\Delta M \Delta\eta}$ $(\Delta\eta = 1.6)$
1**	13-16	0.208
2*	16-19	0.208
3	19-23	0.156
4	23-28	0.125
5	28-34	0.104
6	34-41	0.089
7	41-49	0.078
8	49-58	0.069
9	58-69	0.057
10	69-82	0.048
11	82-100	0.035
12*	100-120	0.031

Table 5.1: The mass ranges and phase space factors for the cross section result. The starred bins (2 and 12) are used when unfolding but are not shown in the final result. The double starred bin (1) is only used when calculating the systematic on the unfolding due to bin choice.

the raw yield corrected for efficiency, acceptance effects, and bin smearing due to finite detector resolution. In this analysis, all the corrections needed to take the raw yield to the corrected yield J are handled in the unfolding procedure, which is described in section 5.2.

5.1 Trigger Selection

Section 3.2 described how events were selected for this analysis based on the energy deposited in the calorimeters. This section will describe how the di-jet events are sorted into different trigger categories.

A di-jet event is categorized based on the trigger conditions satisfied by its individual jets. An individual jet can fall into one of three mutually exclusive categories: L2JetHigh, JP1Lo, and JP1Hi. If a jet does not fall into one of these categories, it is considered untriggered. The conditions a jet must satisfy to be placed in one of these three categories are listed below:

L2JetHigh: The jet must be geometrically matched to a jet patch which fired the L0 L2JetHigh trigger. The jet must also have $p_T \geq 8.4$ GeV.

JP1Lo: The jet must be geometrically matched to a jet patch which fired the L0 JP1 trigger. The jet must also have $p_T < 8.4$ GeV.

JP1Hi: The jet must be geometrically matched to a jet patch which fired the L0 JP1 trigger. The jet must also have $p_T \geq 8.4$ GeV. Finally the L0 L2JetHigh trigger cannot have fired.

The geometric matching condition is that the thrust axis of a jet must be within a radius of 0.6 in $\eta - \phi$ space of the center of the jet patch (or the E_T-weighted centroid of two adjacent jet patches for the AJP component of L2JetHigh). The p_T conditions are designed to ensure no jet can be placed into more than one category.

There are eight unique, valid combinations of trigger categories for a di-jet event: L2JetHigh-L2JetHigh, L2JetHigh-JP1Lo, L2JetHigh-Untriggered, JP1Lo-JP1Lo, JP1Lo-JP1Hi, JP1Lo-Untriggered, JP1Hi-JP1Hi, and JP1Hi-Untriggered. Because the cross section calculation depends on the average prescale factor for the event sample, it was decided to split the sample into events which were take-all and those which were prescaled. The L0 L2JetHigh trigger was take-all throughout the run, so all combinations which contain a jet in the L2JetHigh category are grouped together and are referred to as the L2JetHigh sample. The remaining combinations are also grouped together and referred to as the JP1 sample. The final cross section is computed from the L2JetHigh sample only and the JP1 sample was used as a consistency check.

5.2 Unfolding

In order to make comparisons to theory, or to other experimental data, the di-jet cross section should be plotted as a function of the physical invariant mass. What is measured, however, is an invariant mass which has been distorted by various detector effects such as acceptance and finite resolution. The challenge then is to take the measured invariant mass spectrum and, using detailed knowledge of the detector response, work back to the physical invariant mass spectrum. This process is known as unfolding [69], and can be described in terms of a set of linear equations:

$$\mathbf{A}\mathbf{x} = \mathbf{b} \tag{5.2}$$

If the invariant mass is divided into $\mathcal{N}$ bins, then $\mathbf{x}$ and $\mathbf{b}$ are vectors with dimension $\mathcal{N}$ where the i^{th} component of the vector contains the particle and detector level cross sections, respectively, in the i^{th} mass bin. $\mathbf{A}$ is an $\mathcal{N} \times \mathcal{N}$ response matrix relating the particle (or parton) level to the detector level. The vector $\mathbf{b}$ is what is measured, and $\mathbf{A}$ is constructed from simulation, so equation 5.2 must be solved for $\mathbf{x}$. These types of inversion problems can be ill-determined and unstable with respect to small variations in $\mathbf{A}$ or $\mathbf{b}$. There are a number of techniques that can be used to unfold measured distributions in a stable way, and several will be discussed in section 5.2.3.

5.2.1 Response Matrix

The response matrix encodes the response of the detector to a given physical input, *i.e.*, it shows how a particular observable will be reconstructed. In practice, the response matrix is a 2-dimensional histogram filled from simulation, as shown in figure 5.1. The x-axis is the detector level di-jet invariant mass, and the y-axis shows the corresponding particle or parton level di-jet mass. Both axes use the binning shown in table 5.1.

Because the response matrix relates the detector level to the particle or parton levels, only the simulation which passes the trigger filter can be used to populate this histogram, as only those events undergo the full detector simulation (see section 3.5 for a description of the simulation). The first step in populating the response matrix is to find a di-jet at

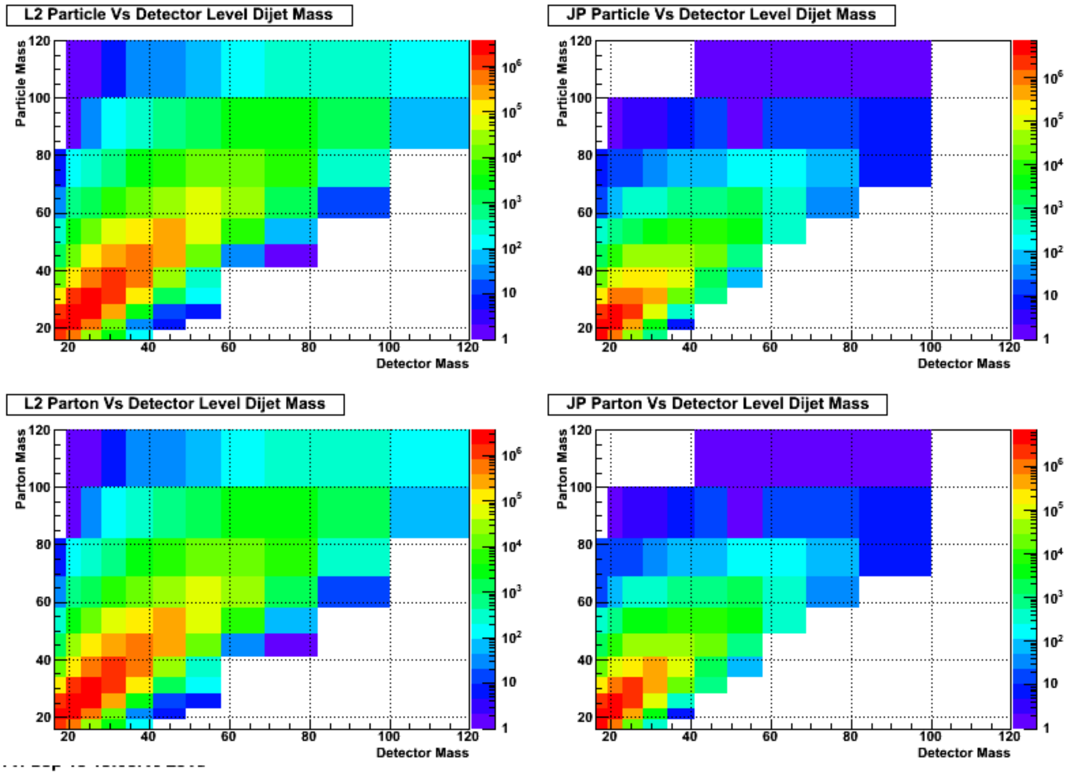

Figure 5.1: The response matrices used in the analysis. The top panels show the L2JetHigh (left) and JP1 (right) particle level vs. detector level response matrices, and the bottom panels show the parton level vs. detector level matrices.

the detector level. The same selection criteria used for the data are used to find di-jet candidates in the simulation, and the same cuts are placed on the simulated candidates. Once the detector level di-jet has been found, the next step is to find the matching particle or parton level di-jet. A detector level di-jet is said to have a matching particle or parton level di-jet if both detector level jets have matching particle or parton level jets.

For each detector level jet, the matching jet is found by looping over all particle or parton level jets and selecting the one which is closest in $\eta - \phi$ space, that is, the one that minimizes the quantity ΔR, defined by:

$$\Delta R = \sqrt{\left(\eta_{\mathrm{Det}} - \eta_{\mathrm{Par}}\right)^2 + \left(\phi_{\mathrm{Det}} - \phi_{\mathrm{Par}}\right)^2} \tag{5.3}$$

A particle or parton level jet is only considered matched to a detector level jet if $\Delta R < 0.5$. No kinematic cuts beyond the matching criteria are placed on the particle or parton level jets.

Once the particle or parton level di-jet which matches the detector level di-jet is found, the invariant masses of both di-jets are calculated. For each event containing matching di-jets, the response matrix bin which corresponds to the intersection between the detector level and particle or parton level invariant mass is filled.

5.2.2 False Events and Efficiency Corrections

Before the response matrix can be used in the unfolding to correct the invariant mass spectrum of the data back to the particle or parton level, a correction must be made to the data to remove false events. The fraction of false events is found by taking the ratio of detector level di-jets which have a matching particle / parton level jet to the total number of detector level di-jets in the simulation. This correction fraction is calculated for each mass bin and trigger type, and for the particle and parton levels. Figure 5.2 shows the correction factors for the particle level and parton levels. The particle level correction factors are so close to unity that they are set identically to one in the analysis.

After the false event correction is applied and the response matrix is used to unfold the invariant mass spectrum of the data back to the particle or parton level, an efficiency correction needs to be applied to account for particle or parton level di-jets which are missed. To find this correction factor, the full Pythia sample is needed. This sample contains all 21 million embedded events, regardless of whether or not they passed the trigger filter. Note that the full Pythia sample only has particle and parton level information. Because the full Pythia sample contains all jets which arise from the generated hard-scattering events, the difference between the full Pythia yield and the matched particle / parton yield gives a measure of the total efficiency. The efficiency correction determined in this way should remove all remaining dependence on the specifics of the analysis, such as trigger and detector acceptance effects.

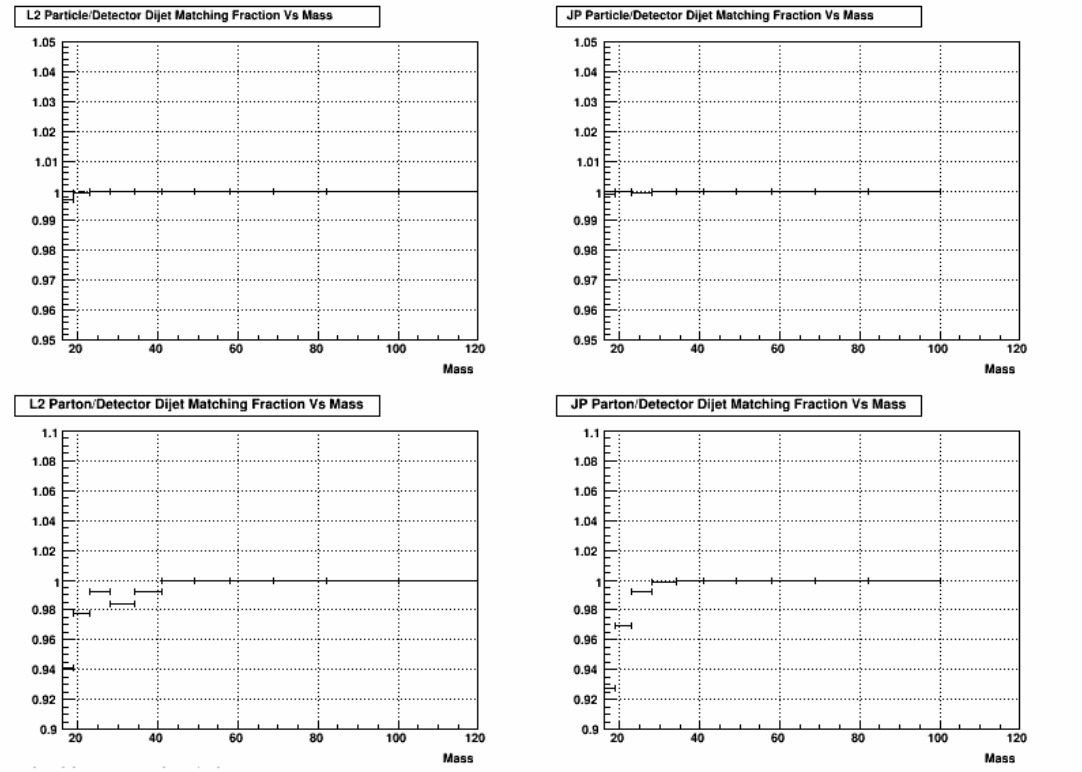

Figure 5.2: This figure shows the matching fraction, that is, the ratio of the number of detector level di-jets which have matching particle or parton level di-jets to the total number of detector level di-jets. The upper row shows the matching to particle level and the bottom row shows the matching to parton level. The left column is for L2JetHigh di-jets and the right column is for JP1 di-jets

5.2.3 RooUnfold Package

The unfolding and corrections described above are all handled by the RooUnfold package [70]. RooUnfold is a software package based on the ROOT [71] analysis framework which implements several unfolding methods, including the bin-by-bin method, an iterative method based on Bayes' theorem [72], and one based on the Singular Value Decomposition method [73]. RooUnfold is run from a ROOT script and takes as input histograms containing the raw data, the response matrix, the total number of matched and unmatched di-jets from the simulation sample which passes the trigger filter, and the total number of di-jets from the full Pythia sample.

The Singular Value Decomposition (SVD) method was used to unfold the raw data for the cross section analysis. The SVD method allows for the expression of the response matrix in terms of a set of singular values and singular vectors. Once the response matrix is expressed in this way, it is relatively easy to identify and overcome problems which arise due to degeneracies in the problem, and the set of linear equations presented in equation 5.2 can be solved in a stable way for $\mathbf{x}$.

The SVD routine requires a cutoff parameter to drop degenerate terms in the problem which may cause instability in the unfolded result. The cutoff parameter can run between zero and the number of bins in the problem. The smaller the cutoff parameter, the more closely the unfolded result will follow the original, while the larger the cutoff parameter, the more the unfolded result will be dominated by unphysical statistical fluctuations. The cutoff value is the only parameter needed by the SVD method, but there are several other parameters required to specify the behavior of RooUnfold. These parameters set the number of toy simulations used in the propagation of errors and the error methods used. The parameters used in this analysis are:

- Number of Toys = 1000
- IncludeSystematics = 1
- ErrorMethod = 2

The SVD method was used to unfold the raw data, but the physical cross section should not depend on the unfolding method used. To confirm that the choice of unfolding method did not significantly affect the extracted cross section, two other methods were tested: the bin-by-bin correction and the iterative Bayesian method. The bin-by-bin method was the simplest correction used. The yield in each di-jet mass bin is multiplied by the ratio of the number of particle or parton di-jets found in the full Pythia sample to the number of particle or parton di-jets which were matched to a detector level di-jet, as described in section 5.2.1. This method does not account for possible bin migration effects. A comparison of the cross section extracted using the bin-by-bin correction to that extracted using the SVD unfolding method can be seen in figure 5.3.

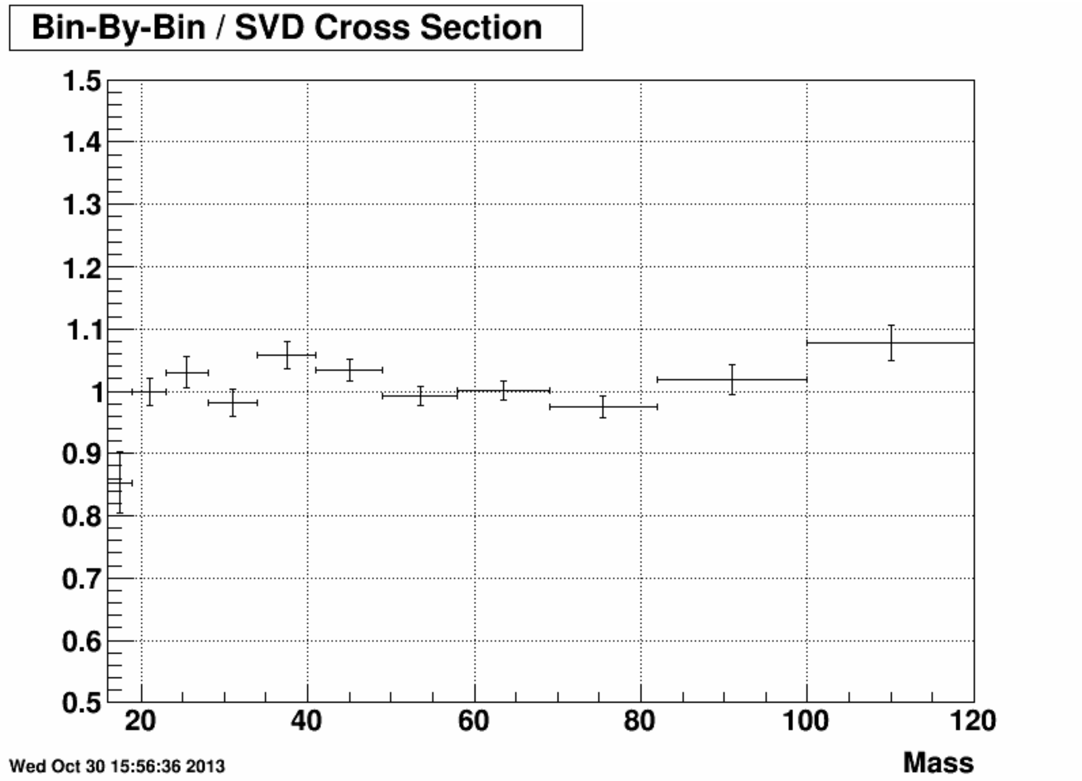

Figure 5.3: Ratio of the di-jet cross section extracted using the Bin-by-Bin correction method to the cross section extracted using the SVD method. Note: the statistical error bars were computed using the error from the SVD method only, as the Bin-by-Bin errors are not handled correctly by RooUnfold.

The second unfolding method tested was the iterative Bayesian method which repeatedly applies Bayes' theorem to bring the raw distribution asymptotically close to the true distribution. The raw distribution serves as the input to the first application of Bayes' algorithm, and that output becomes the input to the next application. This pattern continues until a set number of iterations is reached. The number of iterations used is determined by the user and is usually set at the point where subsequent iterations do not significantly change the unfolded distribution. A comparison of the cross section extracted using the iterative Bayesian method using several different numbers of iterations to the cross section extracted using the SVD method can be seen in figure 5.4.

The production version of RooUnfold that was used in this analysis was version 1.1.1.

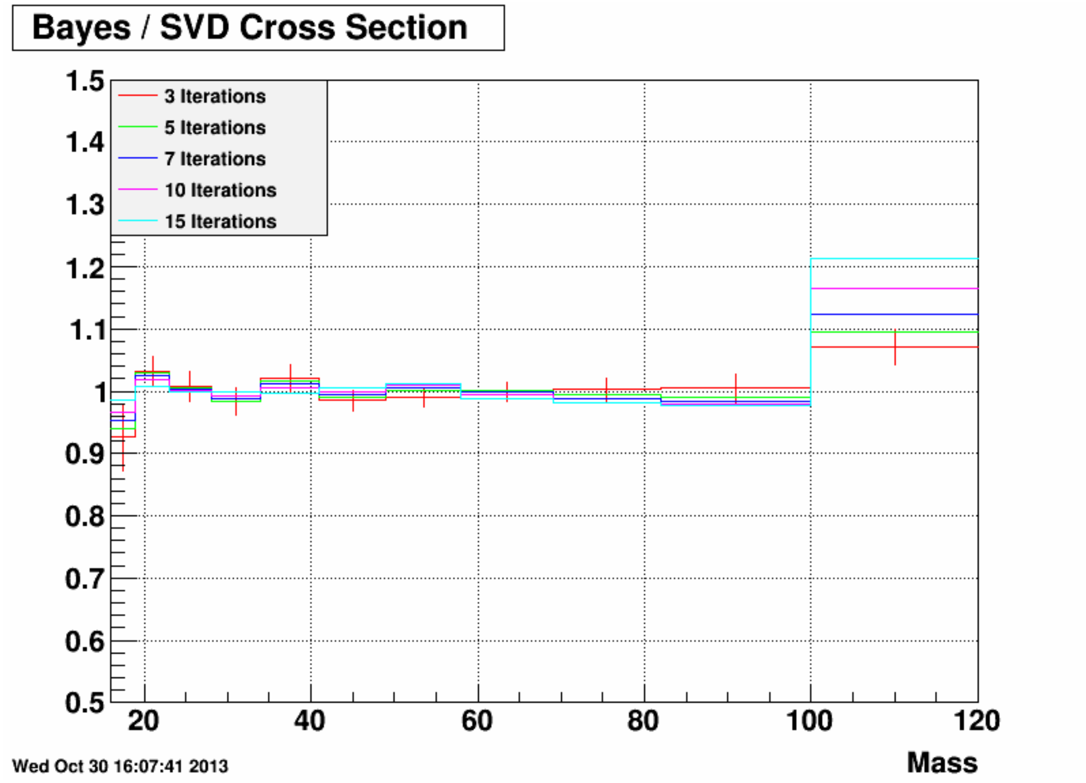

Figure 5.4: Ratio of the di-jet cross section extracted using the iterative Bayesian method to the cross section extracted using the SVD method. Several different numbers of iterations are shown. Note: the statistical error bars were computed using the error from the SVD method only, and are shown only for the iteration = 3 curve to avoid clutter on the plot.

During the course of implementing the package it was found that there was an error with the way RooUnfold calculates the statistical error due to the finite statistics of the response matrix. As mentioned in section 3.5, the simulation was generated in ten partonic p_T bins, and each bin has an associated weight factor. In addition to these weights, an overall normalization factor can be applied, which corresponds to a luminosity. This luminosity factor should not affect any physical observable; however it was found that the size of the statistical error bars on the unfolded mass spectrum depended on this overall normalization. This means that the contribution to the statistical error from finite simulation statistics could be made arbitrarily small simply by changing the luminosity factor, for the same number of simulated events.

This issue was brought to the attention of the RooUnfold author, Tim Adye, and the author of the TSVDUnfold method in ROOT (which the RooUnfold SVD method calls), Kerstin Tackmann. With their help, the issue was identified and a fix was implemented. This fix has not been propagated through official versions of ROOT or RooUnfold yet, so this analysis uses a developmental version of RooUnfold: version 345. This version can be downloaded via the RooUnfold web page [70].

5.3 Systematic Errors

The extraction of the di-jet cross section relies on information from many subsystems of the STAR detector. Systematic uncertainties in the responses of these subsystems will translate into systematic errors on the extracted cross section, which must be evaluated. The subsystem uncertainties evaluated in this analysis are the TPC track-finding inefficiency, track p_T uncertainty, and BEMC tower energy scale uncertainty. In addition to the systematic errors due to subsystem response uncertainties, there are errors associated with the parameters used in the SVD unfolding. The systematic effects investigated were those due to the choice of cutoff parameter and to the choice of the number of bins used in the unfolding. The final systematic effect which was investigated was an apparent decrease in the cross section as a function of time through the run.

5.3.1 Detector Response Systematics

The systematic errors on the cross section due to uncertainty in the track-finding efficiency, the track p_T scale, and the BEMC tower energy were all found using the same procedure. For all three systematics, the appropriate quantity was altered in the simulation sample and the jet finder was rerun, with each alteration residing in a separate branch of the resulting jet trees. This means that the response matrix and efficiency factors used to unfold the data, and thus the resulting cross section, will contain the effect of the corresponding uncertainty. This altered cross section was then compared to the nominal one to obtain the systematic.

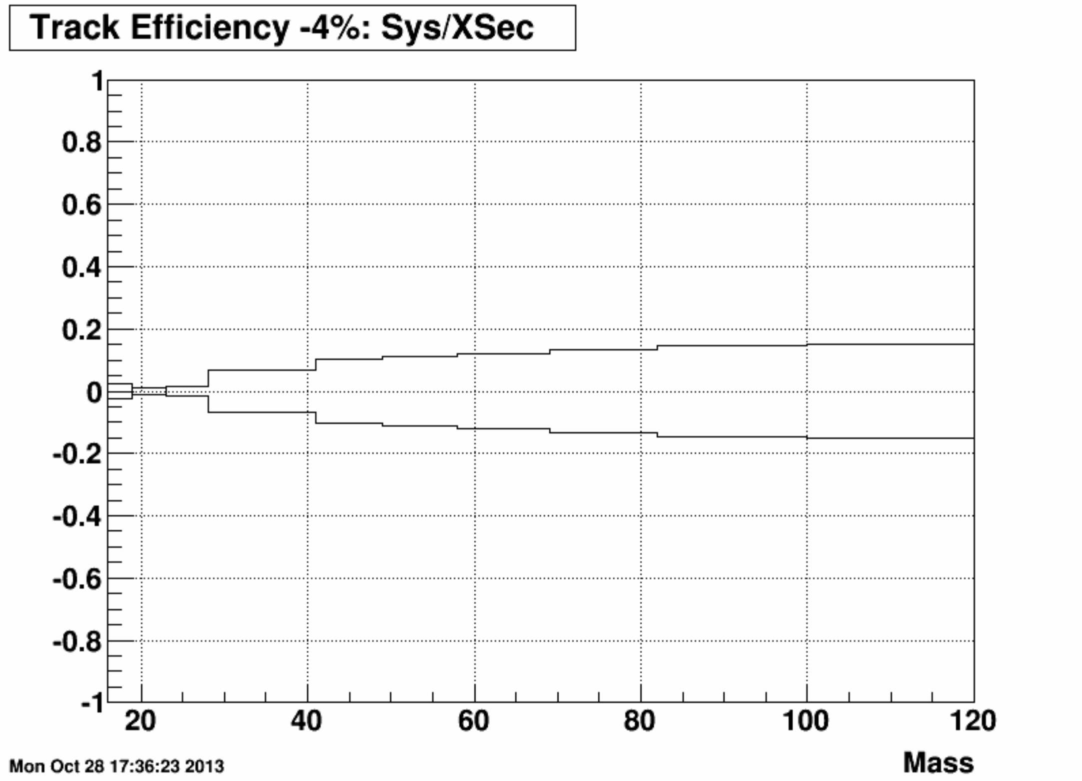

Figure 5.5: Size of the track-finding inefficiency systematic divided by the value of the cross section for each mass bin.

The track-finding efficiency systematic was found by randomly removing 4% of all reconstructed tracks before the jet finder was run. The value of the systematic in each cross section bin is the magnitude of the difference between the cross section obtained using the track loss jet branch and the nominal cross section. This value was then added to and subtracted from the value of the nominal cross section in a given bin to get the track-finding efficiency systematic error band. Figure 5.5 shows the size of the track-finding efficiency systematic.

The systematic due to the track p_T uncertainty was found by increasing and decreasing the track p_T by one percent before the jet finder was run. Two altered cross sections are calculated, one from the plus 1% branch and one from the minus 1% branch. The magnitudes of the differences between the nominal cross section and the two altered cross sections are found, and the value of the systematic is taken as the average of these two differences. Again, this systematic value was added to and subtracted from the nominal

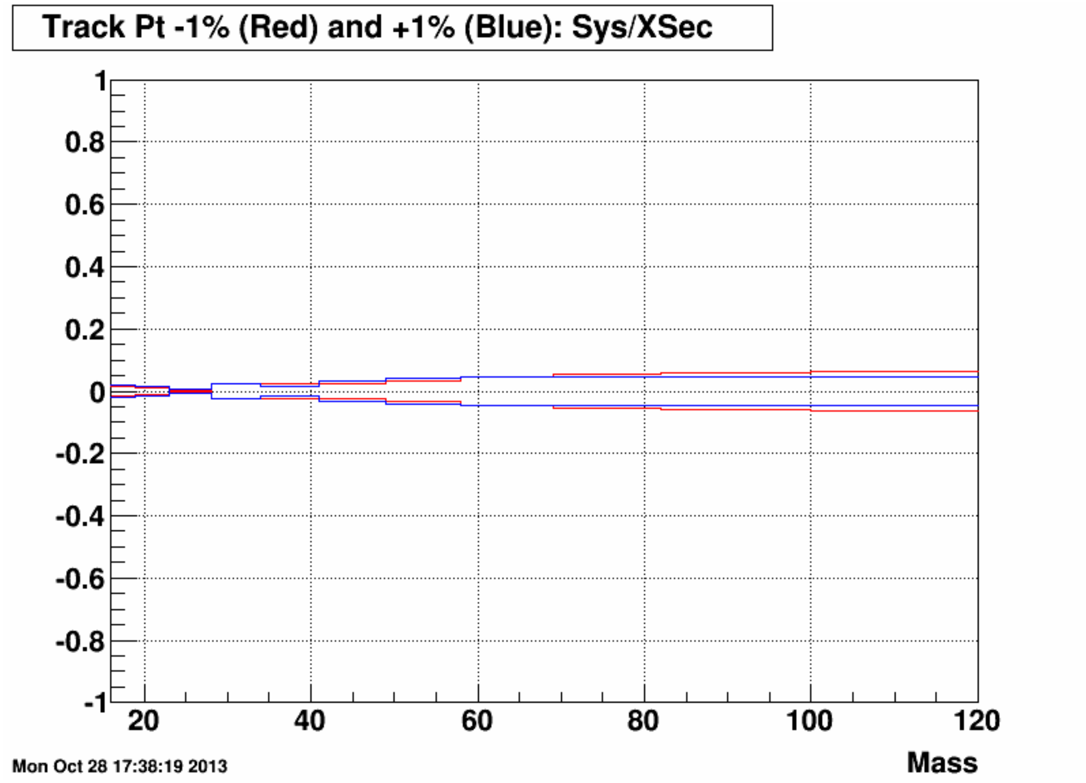

Figure 5.6: Size of the track p_T systematic divided by the value of the cross section for each mass bin. The red curve represents the -1% shift and the blue curve represents the +1% shift.

cross section to get the systematic error bounds. Figure 5.6 shows the size of the track p_T systematic.

The systematic due to the uncertainty of the BEMC tower energy scale is found in the exact same way as the track p_T systematic. The tower energy was scaled up and down by 3.7% before the jet finder was run. The value of 3.7% is the estimated uncertainty in the average absolute gain of the BEMC towers (see discussion in appendix A). Figure 5.7 shows the size of the BEMC tower energy systematic.

5.3.2 Unfolding Systematics

This section describes the sensitivity of the unfolded cross section to the choices made in the implementation of the SVD method. The first effect looked at was the sensitivity of the cross section to the choice of cutoff parameter. As mentioned above, the nominal

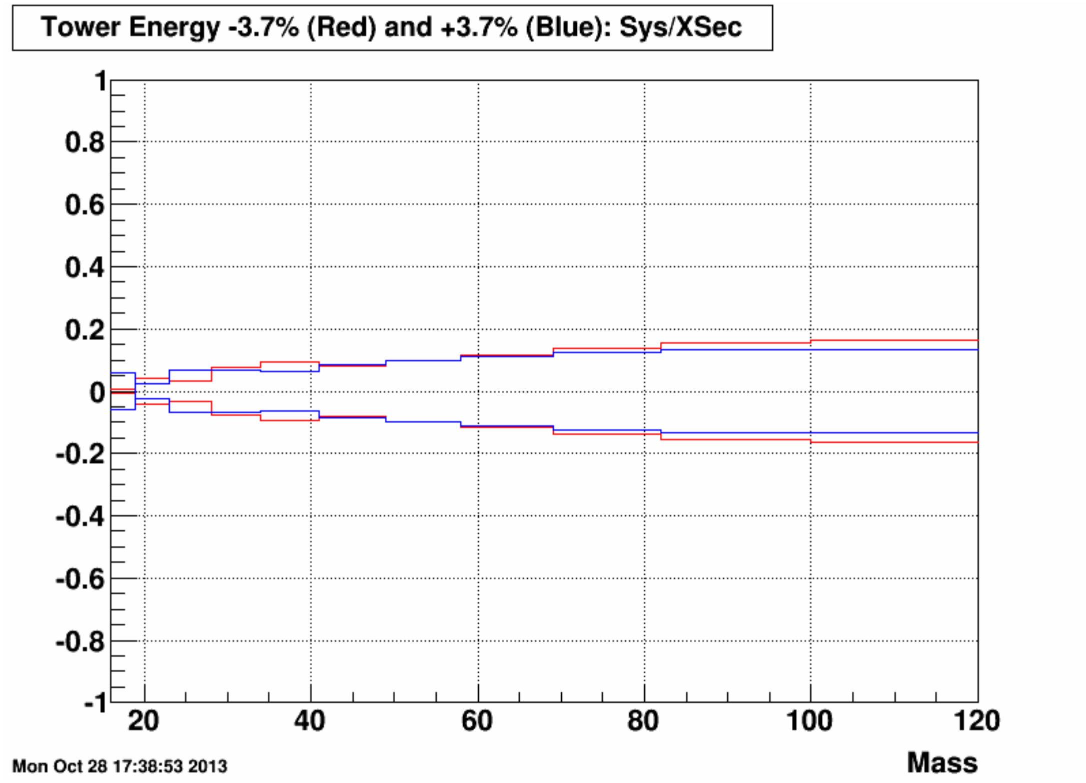

Figure 5.7: Size of the systematic due to the uncertainty in the barrel tower energy scale divided by the value of the cross section for each mass bin. The red curve represents the -3.7% shift and the blue curve represents the +3.7% shift.

cross section was unfolded using a cutoff value of six. The systematic on this choice was evaluated by recalculating the cross section using cutoff values of five and seven. The value of the systematic error was taken as the average of the magnitudes of the differences between the nominal cross section and the cross section obtained using the cutoff values of five and seven. Figure 5.8 shows the size of this systematic.

The second systematic effect evaluated was the sensitivity of the result to the number of bins included when unfolding. For this analysis, the unfolding was done using eleven invariant mass bins, but nine bins are shown in the final result. The two extra bins (one on the low mass side and one on the high mass side) were used in the unfolding to properly account for any bin migration effects into and out of the region of interest. The extra bin on the low mass side extends from 16-19 GeV/c^2, however there are di-jet events which exist with invariant masses below 16 GeV/c^2. To gage the effect of the

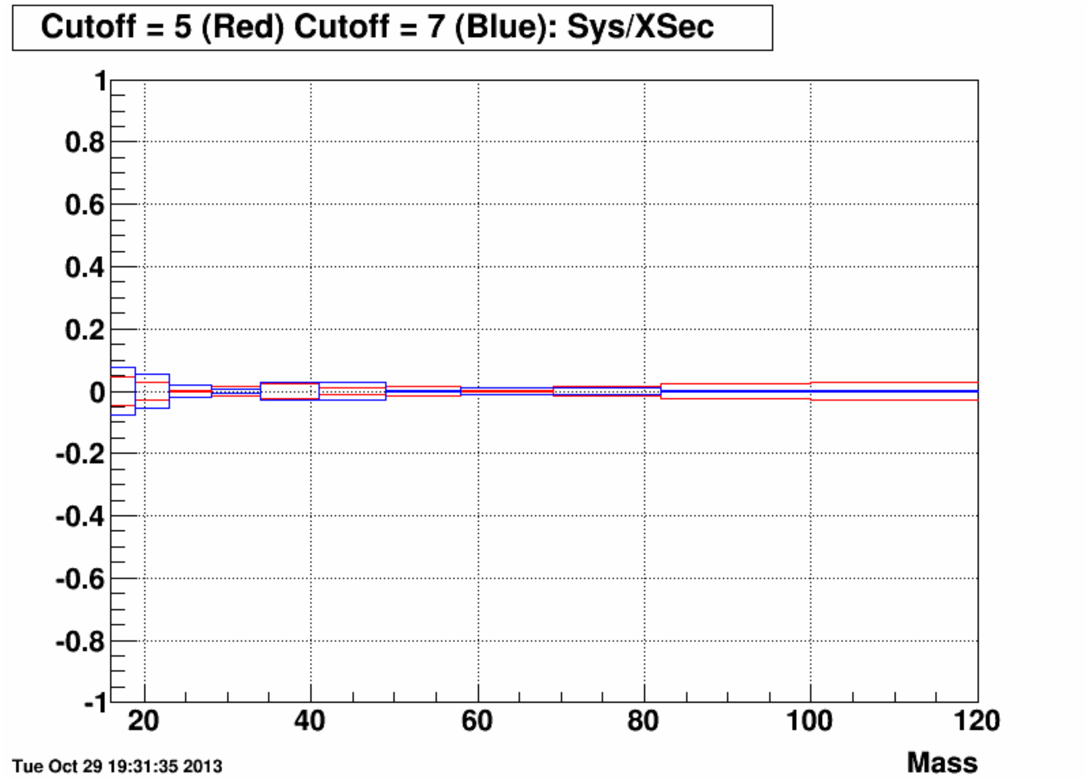

Figure 5.8: Size of the systematic due to a change in SVD cutoff value divided by the value of the cross section for each mass bin. The red curve represents a cutoff value of 5 and the blue curve represents a cutoff value of 7.

bin migration from these low mass di-jets, a bin from 13-16 GeV/c^2 was added, and the unfolding rerun. The size of the systematic was taken as the magnitude of the difference between the nominal cross section and the cross section obtained using the extra low mass bin. Figure 5.9 shows the size of this systematic.

Both systematic effects investigated associated with the unfolding method were found to not significantly impact the overall systematic and were thus neglected in the final error estimate.

5.3.3 Time Variation Systematic

The final systematic effect investigated in the cross section analysis was an observed drop in cross section as a function of time throughout the run. To check the stability of the cross section, the full data sample was broken into two periods, corresponding to the two

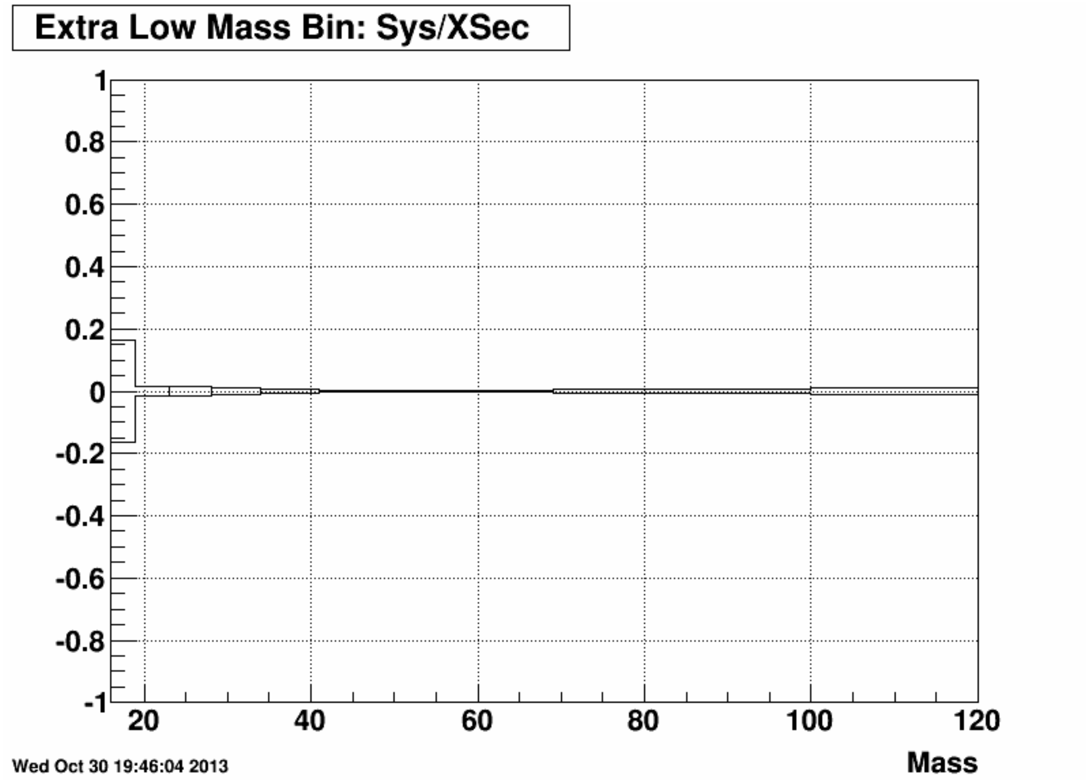

Figure 5.9: Size of the systematic due to the addition of a low mass bin when unfolding, divided by the value of the cross section for each mass bin.

magnetic field directions of the STAR solenoid used during the run. It was found that the cross sections determined from the two periods were significantly different. To further investigate this issue, the data sample was split into six time periods, each covering ten days (a seventh period was also included which only covered day 180). The raw di-jet yields from each period were normalized by the integrated luminosity from that period and compared to each other, as shown in figure 5.10. It is seen that the raw number of di-jets, normalized by the corresponding integrated luminosity, decreased throughout the run. There are a number of possible mechanisms which could cause this drop, and the issue is still under investigation. While this study is ongoing, a systematic has been placed on the cross section to account for the uncertainty caused by the drop in normalized raw yield. The size of the systematic was taken as the magnitude of the difference between the cross sections determined for each magnetic field direction. The two cross sections were each calculated independently, using the embedded simulation runs which corresponded to those periods. A comparison of the reverse full-field (RFF) and full-field (FF) cross

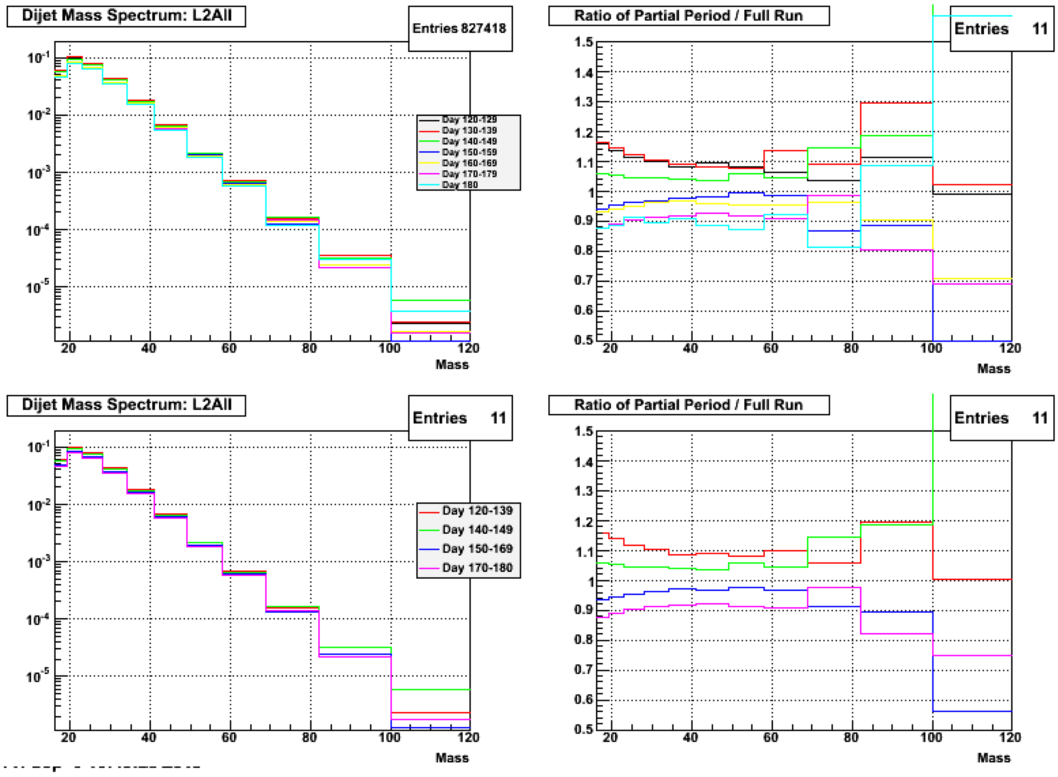

Figure 5.10: This figure illustrates how the normalized di-jet yields changed over the course of Run IX. The top left panel shows the normalized di-jet yields for several periods. The top right panel shows the ratio of the yields from the several periods to the total yield. The bottom two panels show the same quantities for a reduced number of periods.

sections to the full cross section can be seen in figure 5.11.

The final overall systematic uncertainty was found by adding the systematic errors from the track-finding efficiency, track p_T uncertainty, BEMC tower energy scale uncertainty, and time variation together in quadrature. This final systematic error was added to and subtracted from the cross section to give a symmetric error band. Table 5.2 shows the numerical values of the individual systematics divided by the cross section for each bin. Figure 5.12 shows the size of the combined systematic error divided by the measured cross section.

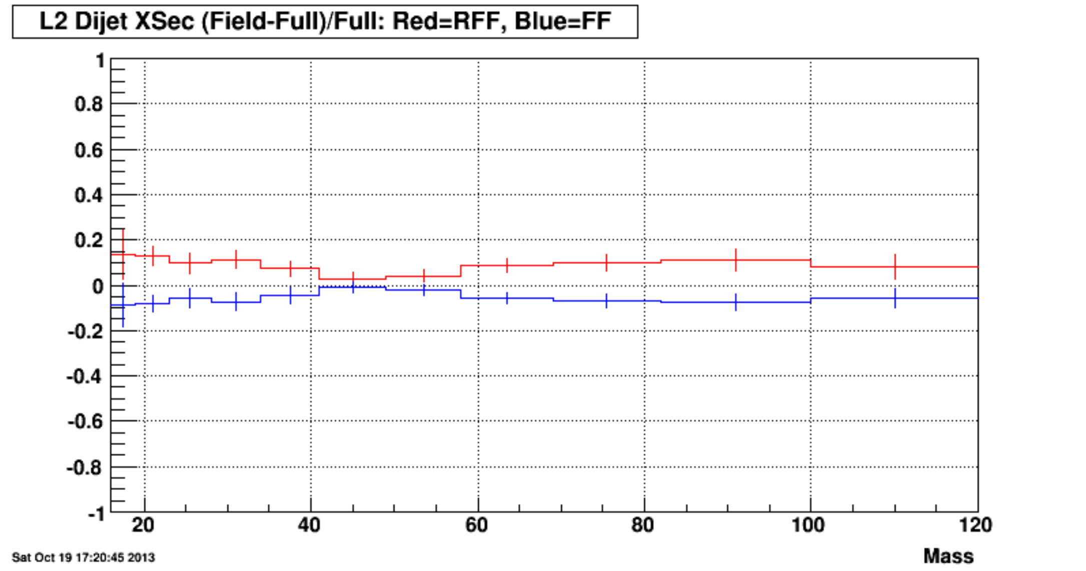

Figure 5.11: Ratios of the Reversed Full Field (red) and Full Field (blue) cross sections to the average cross section. The ratio plotted is (Field-Full)/Full, where Field refers to either the RFF or FF cross section.

Di-jet Invariant Mass [GeV/c^2]	Track Efficiency	Track p_T	Tower E_T	Time Variation	Total
16-19	0.026	0.017	0.033	0.224	0.228
19-23	0.009	0.011	0.033	0.208	0.211
23-28	0.015	0.004	0.049	0.155	0.163
28-34	0.066	0.023	0.074	0.189	0.214
34-41	0.067	0.021	0.079	0.118	0.158
41-49	0.104	0.028	0.082	0.034	0.139
49-58	0.113	0.039	0.099	0.062	0.167
58-69	0.122	0.045	0.114	0.145	0.225
69-82	0.134	0.050	0.130	0.170	0.257
82-100	0.145	0.053	0.143	0.188	0.282
100-120	0.150	0.055	0.149	0.137	0.258

Table 5.2: Numerical values for the four systematic errors on the cross section, as well as the quadrature sum for each di-jet invariant mass bin.

5.4 Underlying Event and Hadronization Corrections

As mentioned previously, the measured cross section was unfolded and corrected to the particle level, which removes detector effects and allows the measurement to be com-

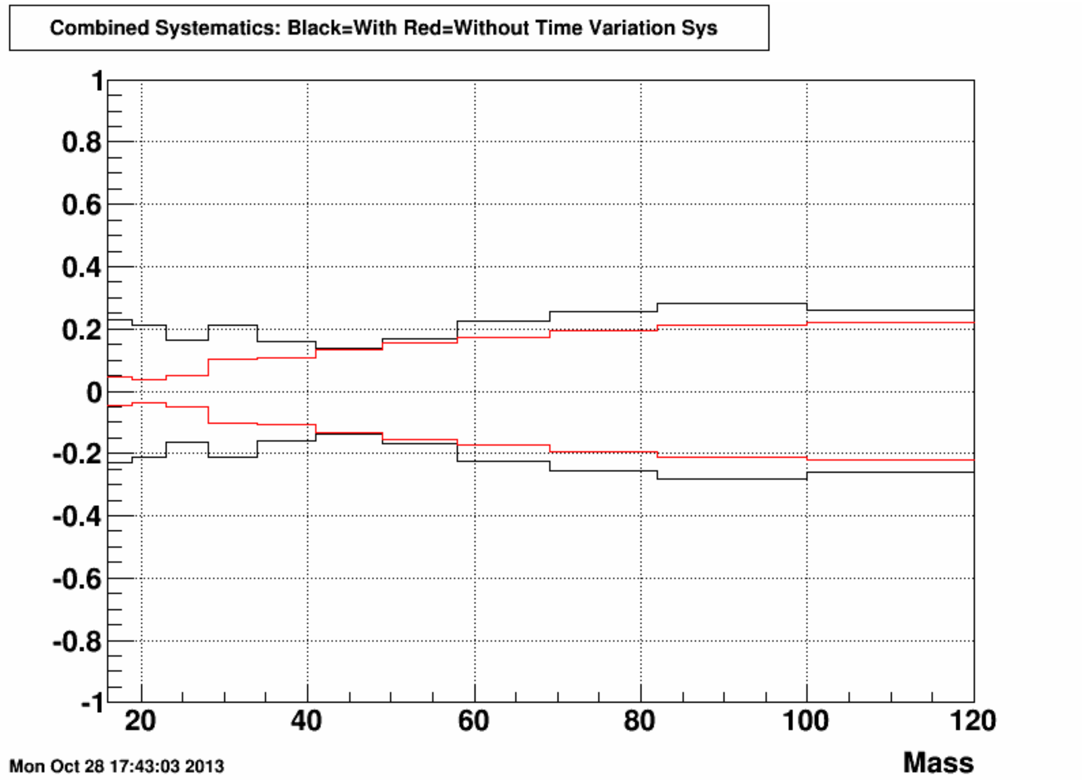

Figure 5.12: The total systematic error for this analysis divided by the cross section. The red curve shows the size of the three detector systematics added in quadrature, while the black curve shows the detector systematics and the time variation systematic combined.

pared to theory or to measurements from different experiments. As discussed in section 3.5, the particle level of the simulation contains the effects due to underlying event and hadronization. However, the theory calculation (next-to-leading order perturbative QCD implemented by Daniel de Florian [30] using the CTEQ6M parton distribution function set [74]) to which the extracted cross section is compared does not include these effects. In order to make a valid comparison between data and theory, these effects must be treated in a consistent manner. There are two ways to ensure consistency. The first is to correct the extracted cross section to the parton level, instead of to the particle level, as the parton level more closely reflects what is calculated in theory. The second way is to determine the size of the underlying event and hadronization effects from simulation, and apply these as corrections to the theory. The second method was used in this analysis.

To determine the size of the underlying event and hadronization effects, the cross section was extracted from the raw data twice, once corrected to the particle level and once to the parton level. Because the particle level contains the underlying event and hadronization effects, while the parton level does not, the difference between particle level and parton level cross sections should be the underlying event and hadronization contribution. This difference was then added to the theoretical cross section so that a valid comparison between data and theory could be made. Figure 5.13 shows the effect of the underlying event and hadronization correction on the theoretical calculation.

5.5 Trigger Sample Comparison

Section 5.1 described how di-jets were sorted into the L2JetHigh and JP1 trigger samples based on the properties of the individual jets in the di-jet. The L2JetHigh sample contains many more events than the JP1 sample, as can be seen in figure 5.14, and so combining JP1 with L2JetHigh would not significantly reduce the statistical errors, compared to using the L2JetHigh sample alone. Because of this, only the L2JetHigh sample was used for the final cross section result.

Note that although the JP1 sample was not used in the cross section result, it is still useful as a cross check on the L2JetHigh sample. The JP1 and L2JetHigh samples have very different raw di-jet invariant mass distributions (see figure 5.14), but the unfolding procedure should remove any differences due to trigger effects in the final cross sections. Any large discrepancies seen between the L2JetHigh and JP1 cross sections could be an indication of a problem. Figure 5.15 shows a comparison between the cross sections determined using the L2JetHigh and JP1 data samples and good agreement is seen at low to intermediate values of invariant mass. At larger di-jet mass values the agreement becomes worse, but this is not surprising given the lack of statistics in the JP1 sample.

5.6 Results

The di-jet cross section is presented as a function of invariant mass in the mid-rapidity ($|\eta| < 0.8$) region. The result was obtained using 17.1 pb^{-1} of pp data taken at $\sqrt{s} = 200$

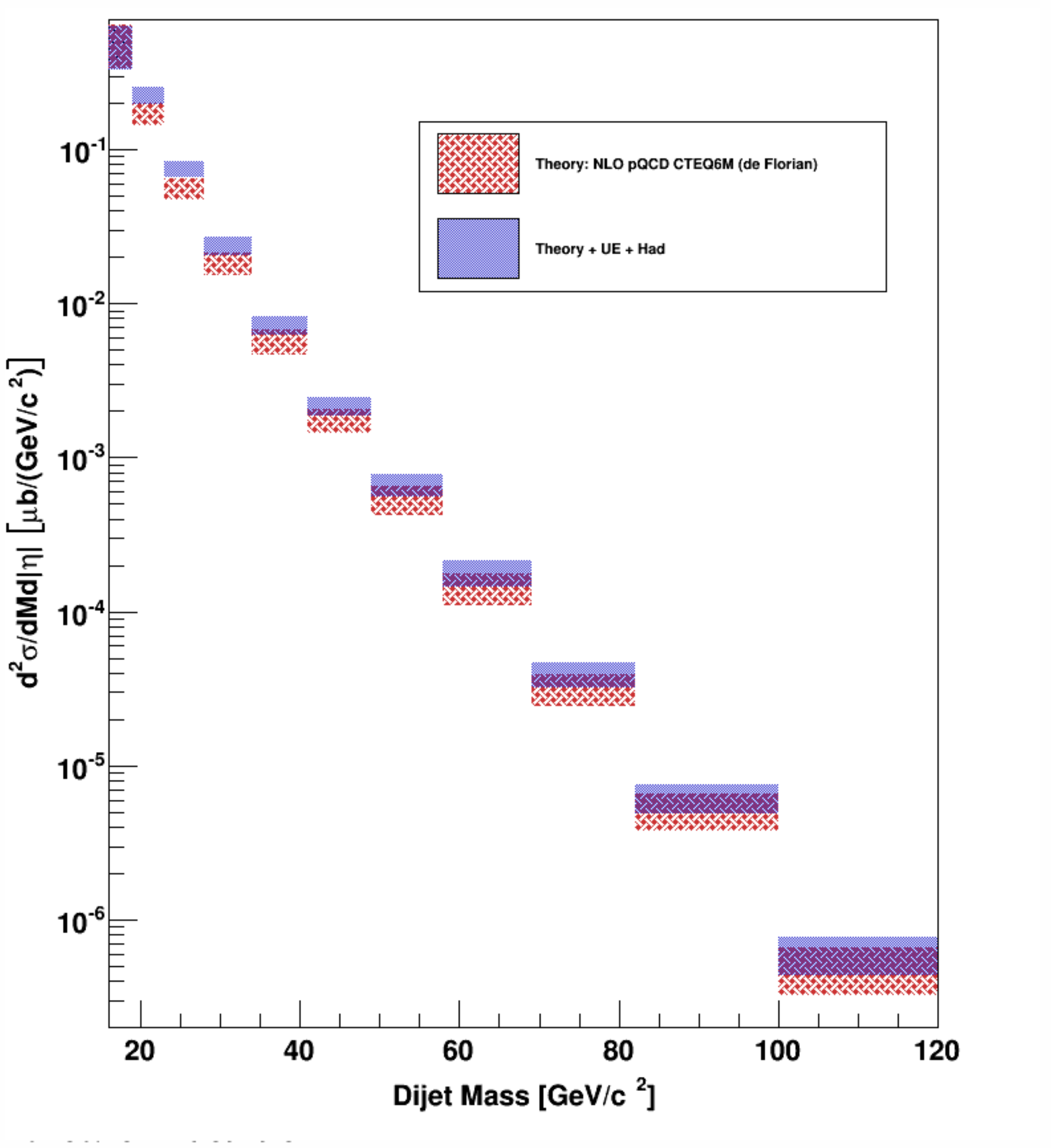

Figure 5.13: Effect of the underlying event and hadronization correction on the theoretical calculation. The thickness of the bands represents the size of the systematic error on the theoretical calculation, derived by changing the factorization and renormalization scales by factors of 0.5 and 2 .

GeV from Run IX, and used the anti-k_T jet algorithm with a radius of 0.6 to reconstruct jets. The results are compared to an NLO pQCD prediction from de Florian using the CTEQ6M [74] PDF set. This theoretical calculation has been corrected for underlying event and hadronization effects. Table 5.3 gives the numerical values found for the cross section, as well as the statistical and systematic errors for each mass bin. Figure 5.16 presents this data graphically and also shows the comparison to the NLO pQCD theoret-

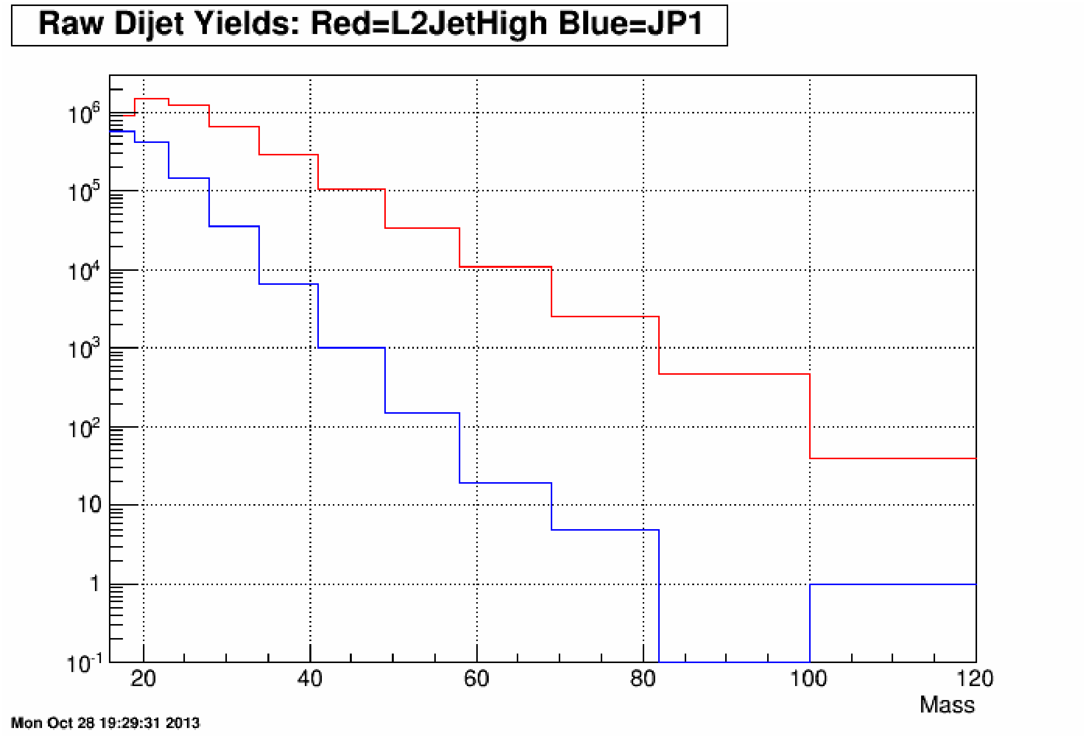

Figure 5.14: Comparison of the raw (no unfolding, normalization, or phase space factors) di-jet yields for the L2JetHigh sample (red) and the JP1 sample (blue).

ical predictions. The error on the theoretical calculation was obtained by changing the normalization and factorization scales together by factors of 0.5 and 2.0. Note that an overall (that is, independent of mass) scale uncertainty of 7.7%, due to the uncertainty on the absolute BBC cross section used in the determination of the integrated luminosity, is not shown in the table or figure.

Figure 5.16 shows that our measured di-jet cross section is in good agreement with the NLO pQCD prediction. This agreement gives us confidence that di-jet processes measured at STAR are well understood, and can be used in A_{LL} measurements. The agreement with theoretical predictions also indicates that the NLO pQCD framework can be used to interpret the A_{LL} results.

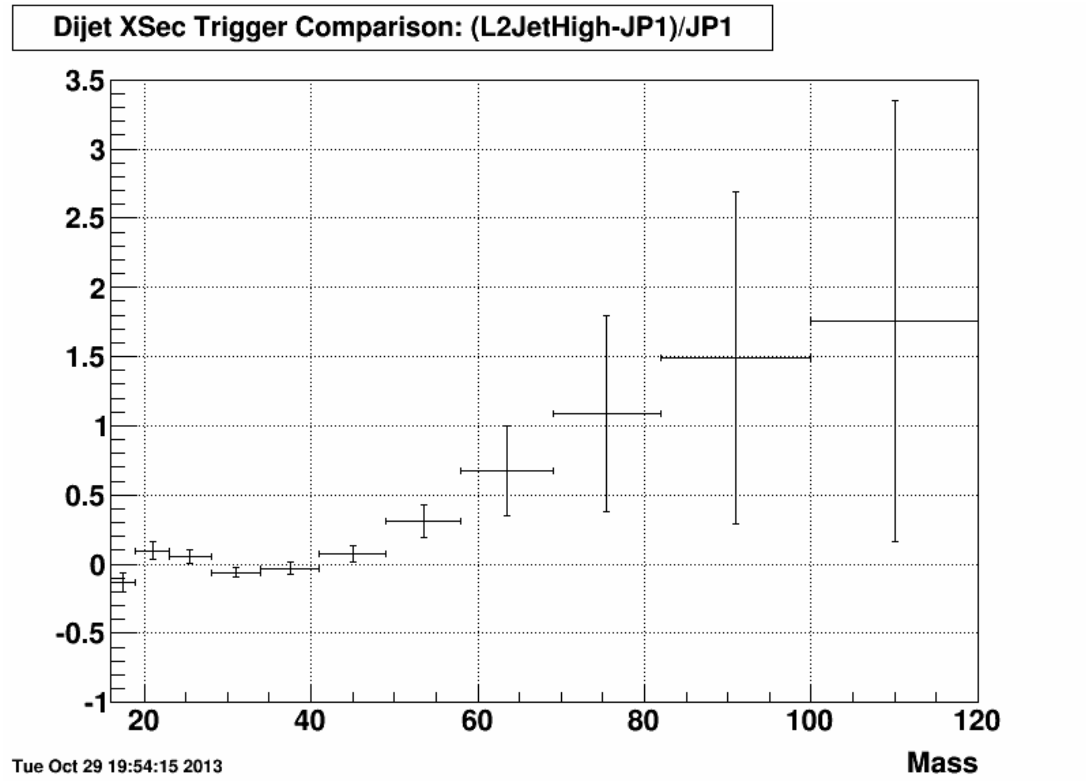

Figure 5.15: Ratio of cross sections obtained using the L2JetHigh and JP1 data samples. Good agreement can be seen between the two cross sections until the JP1 yield dies off at high invariant mass.

Di-jet Invariant Mass [GeV/c^2]	$\sigma \pm$ (stat) $\pm$ (sys)[μb]
19-23	$(2.022 \pm 0.045 \pm 0.426) \times 10^{-1}$
23-28	$(7.263 \pm 0.172 \pm 1.187) \times 10^{-2}$
28-34	$(2.355 \pm 0.053 \pm 0.504) \times 10^{-2}$
34-41	$(6.979 \pm 0.144 \pm 1.103) \times 10^{-3}$
41-49	$(2.275 \pm 0.036 \pm 0.317) \times 10^{-3}$
49-58	$(7.230 \pm 0.108 \pm 1.205) \times 10^{-4}$
58-69	$(1.988 \pm 0.030 \pm 0.448) \times 10^{-4}$
69-82	$(4.680 \pm 0.087 \pm 1.204) \times 10^{-5}$
82-100	$(7.796 \pm 0.183 \pm 2.197) \times 10^{-6}$

Table 5.3: The cross section values (in μb) with statistical and systematic error values for each di-jet invariant mass bin.

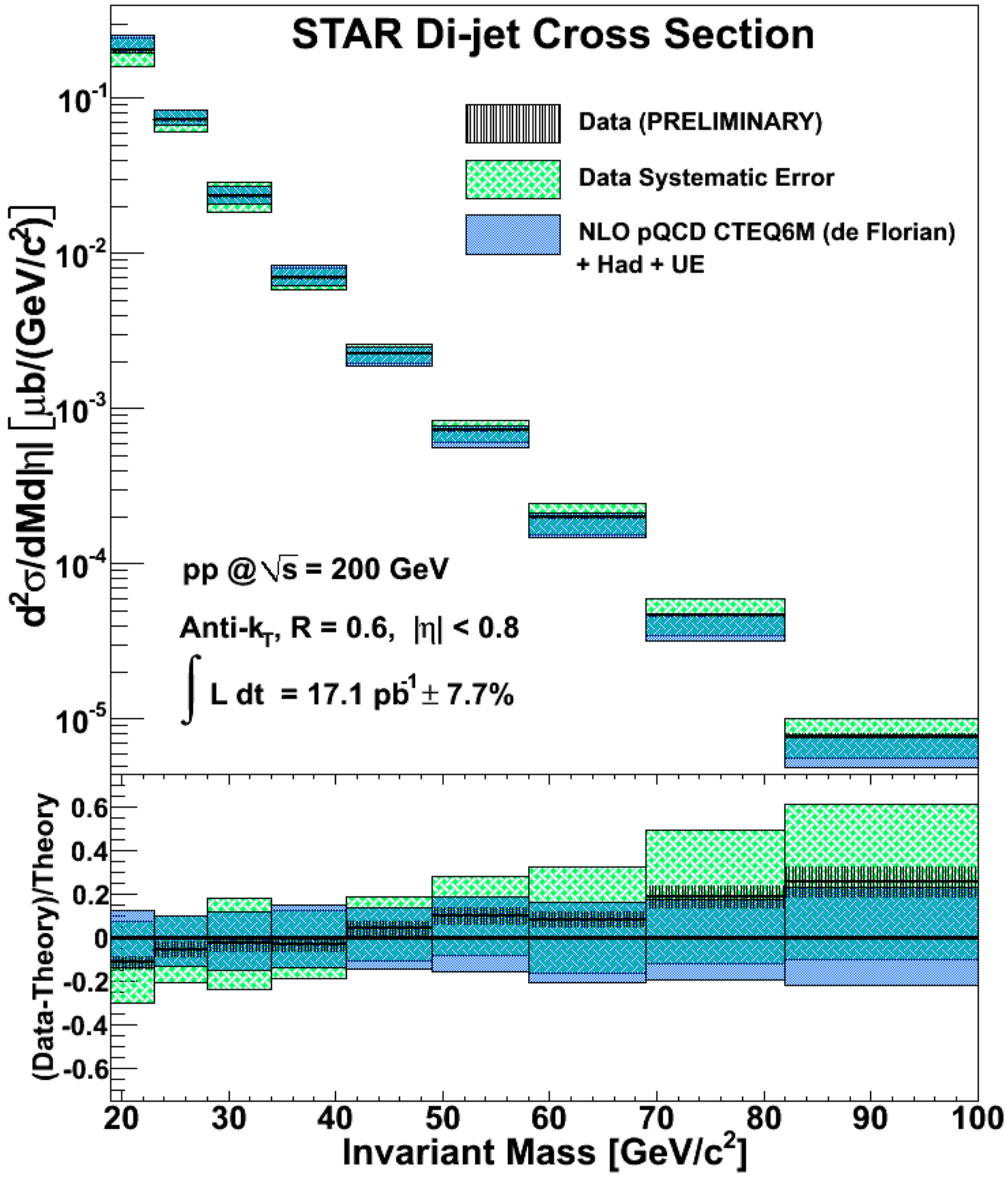

Figure 5.16: The top panel shows the cross section measured in this work (black lines) with the associated systematic error (green hatched box) and theoretical error (purple box). The thickness of the boxes represents the sizes of the respective errors, and the overlap between the two is shown in teal. The bottom panel shows the (Data-Theory)/Theory ratio with the black lines and hatching representing the value and statistical error on the ratio. The green and purple boxes again show the systematic error on the data and theory, respectively.

Chapter 6

Di-jet Helicity Asymmetries

The longitudinal double-spin asymmetry, A_{LL}, is the primary observable used at RHIC to study the gluon spin contribution (ΔG) to the overall spin of the proton. STAR has measured A_{LL} for several final states, including inclusive jet [25] [26] [28] and pion [67] production, and these results have placed strong constraints on ΔG over a range of the gluon momentum fraction x (see section 1.2.1 and references therein). This chapter details the extension of the A_{LL} measurements to di-jet final states which, as described in section 1.2.2, will provide more information about the kinematics of the underlying partonic hard scattering event.

As discussed in section 1.2, the longitudinal double-spin asymmetry is defined in terms of helicity-dependent cross sections:

$$A_{LL} \equiv \frac{\sigma_{++} - \sigma_{+-}}{\sigma_{++} + \sigma_{+-}} \tag{6.1}$$

where σ_{++} (σ_{+-}) is the scattering cross section for partons of the same (opposite) helicity. At STAR, A_{LL} is extracted directly from the helicity-dependent yields of a final state observable, so the expression for the experimentally determined A_{LL} will differ from the above equation. There are also some modifications needed when combining many independent measurements (each run can be considered an independent measurement). Equation 6.2 is the formula for A_{LL} used in this analysis. The derivation of this formula, along with discussion of the relevant assumptions made, can be found in appendix D.

$$A_{LL} = \frac{\sum_i P_{Yi} P_{Bi} \left[\left(N_i^{++} + N_i^{--} \right) - R_{3i} \left(N_i^{+-} + N_i^{-+} \right) \right]}{\sum_i P_{Yi}^2 P_{Bi}^2 \left[\left(N_i^{++} + N_i^{--} \right) + R_{3i} \left(N_i^{+-} + N_i^{-+} \right) \right]} \tag{6.2}$$

The summation is over all runs i in the data set. The factors P_Y and P_B represent the polarization values of the Yellow and Blue beams, respectively (see section 6.1 for more details). $N^{++}, N^{--}, N^{+-},$ and N^{-+} represent the yields for the four possible beam helicity combinations, where the first index denotes the helicity of the yellow beam bunch and the second index denotes that of the blue beam. The helicity combinations and spin patterns are detailed in section 6.2. The term R_3 in equation 6.2 is the relative luminosity factor, which will be discussed in section 6.3.

The statistical error on A_{LL} can be found by standard error propagation techniques and is given by equation 6.3. The derivation of this error is presented in appendix D.

$$\delta A_{LL} = \frac{\left(\sum_i P_{Yi}^2 P_{Bi}^2 \left[\left(N_i^{++} + N_i^{--} \right) + R_{3i}^2 \left(N_i^{+-} + N_i^{-+} \right) \right] \right)^{\frac{1}{2}}}{\sum_i P_{Yi}^2 P_{Bi}^2 \left[\left(N_i^{++} + N_i^{--} \right) + R_{3i} \left(N_i^{+-} + N_i^{-+} \right) \right]} \tag{6.3}$$

6.1 Beam Polarizations

The raw asymmetry observed will depend on the degree of polarization achieved for the protons in each beam: there should be zero asymmetry for unpolarized beams, and the asymmetry should rise to a maximum value of A_{LL} as the beams become completely polarized. Of course, the physical A_{LL} should not depend on how highly the beams are polarized during a specific measurement, so the raw asymmetry must be scaled by the beam polarizations, as shown in equation 6.2. There are two systems which monitor the beam polarizations at RHIC, the proton-carbon polarimeters and the hydrogen gas jet, both of which were described in more detail in section 2.1.5. The pC polarimeter system is used for polarization measurements over the course of a fill, while the H-jet system provides an absolute normalization.

There were 103 fills used in the asymmetry measurement. For these fills, the average polarization values for the blue and yellow beams, respectively, were 56.38% and 56.93%. Figure 6.1 shows a plot of the fill-by-fill polarization values for the two beams.

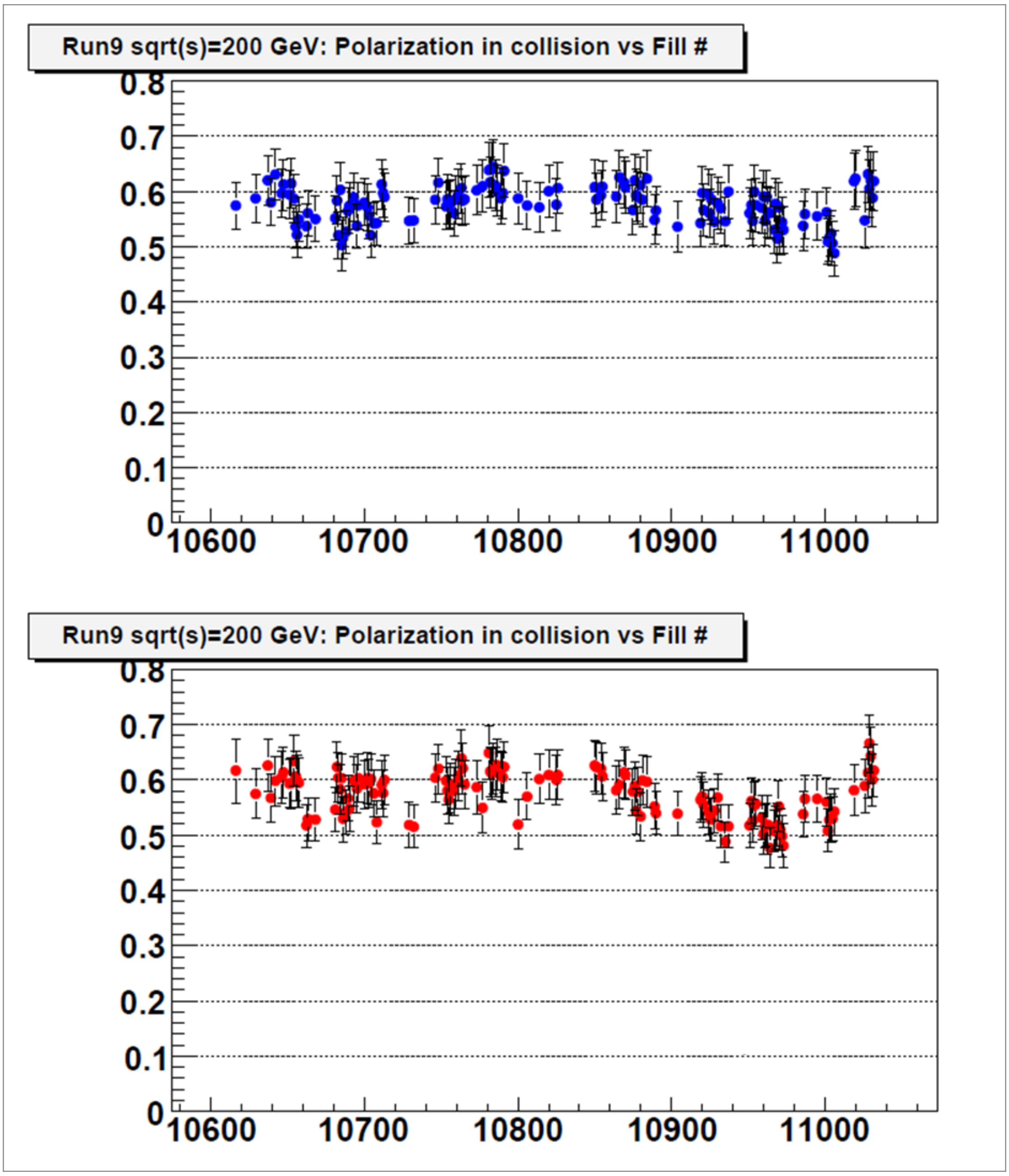

Figure 6.1: Beam polarizations by fill. The top plot shows the polarization of the Blue beam and the bottom plot shows the polarization of the Yellow beam.

6.1.1 Residual Transverse Component

As discussed in section 2.1, the stable proton spin direction in RHIC is transverse (up-down) to the direction of motion. For analyses which require the collision of longitudinally polarized protons, the spin rotators (see section 2.1.3) precess the transverse spin to a longitudinal spin orientation. The spin rotators, however, are not perfect, and there can be residual transverse components in the beams. The beam polarization values discussed

	Before Rotator Change	After Rotator Change
Yellow Beam	$t = 0.15 \pm 0.02$	$t = 0.13 \pm 0.02$
Blue Beam	$t = 0.25 \pm 0.02$	$t = 0.10 \pm 0.03$

Table 6.1: The t values ($t \equiv P_T/P_L$) for the yellow and blue beams before and after the spin rotator tune, which occurred after run 1017050.

above are for the total polarization, $P = \sqrt{P_L^2 + P_T^2}$. The quantity of interest for an A_{LL} measurement is P_L, so any residual transverse component will act as a dilution on the quoted beam polarization values. In this analysis, the beam polarization values returned by the proton-carbon and hydrogen jet polarimeters are scaled by a factor F (equation 6.4) to return only the longitudinal polarization component ($P_L = P \times F$).

$$F \equiv \frac{1}{\sqrt{1+t^2}}, \quad t \equiv \frac{P_T}{P_L} \tag{6.4}$$

During most of Run IX, the beams had a somewhat large transverse component. On June 22, 2009 the rotator currents at STAR were tuned to reduce the size of these residual transverse components (see table 6.1). The values of t listed in the table were used to correct the beam polarizations used in the calculation of A_{LL}.

6.1.2 Polarization Decay

Because of the short time needed to sample the beam polarization using the pC polarimeters, a fill will typically contain several of these measurements. In this way, the change in the polarization of the beam over the course of a fill could be monitored. In addition to a luminosity-weighted average polarization, an initial polarization value and a value for the change in polarization over time was reported for each fill. This information was used to estimate the beam polarizations at the time of each event in the analysis.

The average polarization value reported by the polarimetry group for each fill was weighted by the luminosity over the course of that fill. This means that as long as the number of events sampled scales proportionally with the luminosity, the average polarization would be the correct value to use. This proportionality roughly holds for the L2JetHigh events,

Pattern	Blue Beam Pattern	Yellow Beam Pattern
P1	+ − + − − + − +	+ + − − + + − −
P2	− + − + + − + −	+ + − − + + − −
P3	+ − + − − + − +	− − + + − − + +
P4	− + − + + − + −	− − + + − − + +

Table 6.2: The four spin patterns used in Run IX. The '+' symbol indicates positive helicity, and the '−' indicates negative helicity. The patterns repeat for the remaining bunches in the fill.

as that trigger was take-all throughout the run, so its event rate should scale with instantaneous luminosity. The JP1 trigger, however, was prescaled and the prescale value was chosen in proportion to the instantaneous luminosity at the beginning of each run. This means that JP1 events are taken at a higher rate at the end of fills, when the luminosity is lower. Thus, using the average polarization value for the JP1 sample would tend to overestimate the beam polarizations appropriate for this sample. Calculating A_{LL} using the beam polarizations found as a function of event time alleviates this problem.

6.2 Spin Patterns

During a typical fill, each beam will contain 109 proton bunches (see section 2.1), and each bunch can have an independent polarization direction. The polarization direction of each bunch as a function of bunch number in each beam (the spin pattern) is carefully chosen to ensure that each helicity combination collides in each fill, and that no combination is sampled significantly more than any other. In a given fill, the polarization direction of each bunch in the two beams matched one of four spin patterns (see table 6.2). These four spin patterns were cycled through fill-by-fill over the course of Run IX.

6.2.1 Spin Database

The calculation of A_{LL} requires knowing the four helicity-sorted di-jet yields (N^{++}, N^{--}, N^{+-}, and N^{-+}). To split the di-jet yield in this way, the helicities of the two bunches giving rise to each individual collision must be known. At STAR, this information is stored in the spin database.

As mentioned above, the spin orientation of each bunch is loaded according to one of four patterns for each fill. The BNL Collider and Accelerator Department (C-AD), which is responsible for the operation of RHIC, broadcasts the intended spin orientation for each bunch in each beam, as well as many other pieces of information via an interface known as CDEV [75]. This information is collected every five minutes by STAR, and stored in an offline database. At the end of Run IX, this information underwent a series of quality checks to ensure consistency, and was then used to define the exact times that a particular spin pattern was loaded.

The last piece of information needed to translate the spin pattern obtained from CDEV into a helicity combination for each collision at STAR is the beam cogging index, *i.e.*, which bunch from the yellow beam collided with which bunch from the blue beam in the STAR interaction region. During Run IX, the beams were cogged such that the first blue bunch collided with the first yellow bunch at the 8 o'clock interaction region (PHENIX). This means that at STAR, the first blue bunch will collide with the 80th yellow bunch, the second blue bunch will collide with the 81st yellow bunch, and so forth. Knowing the spin pattern for the fill, and which bunches are colliding for each event, means the helicity combination for each event is known.

At STAR, the colliding bunch helicity combination is encoded as a 'Spin-4' value (see table 6.3). The information on spin pattern and beam cogging is stored in an offline spin database which is accessed during an analysis, so that the Spin-4 value for any bunch crossing can be found. For a given spin pattern, each bunch crossing will have a set Spin-4 value. The Spin-4 values vs. bunch crossing number for all four spin patterns can

Spin-4	Yellow Beam Helicity	Blue Beam Helicity
5	$-$	$-$
6	$+$	$-$
9	$-$	$+$
10	$+$	$+$

Table 6.3: The four ‘Spin-4’ values used to label the helicities of the colliding bunches for each event.

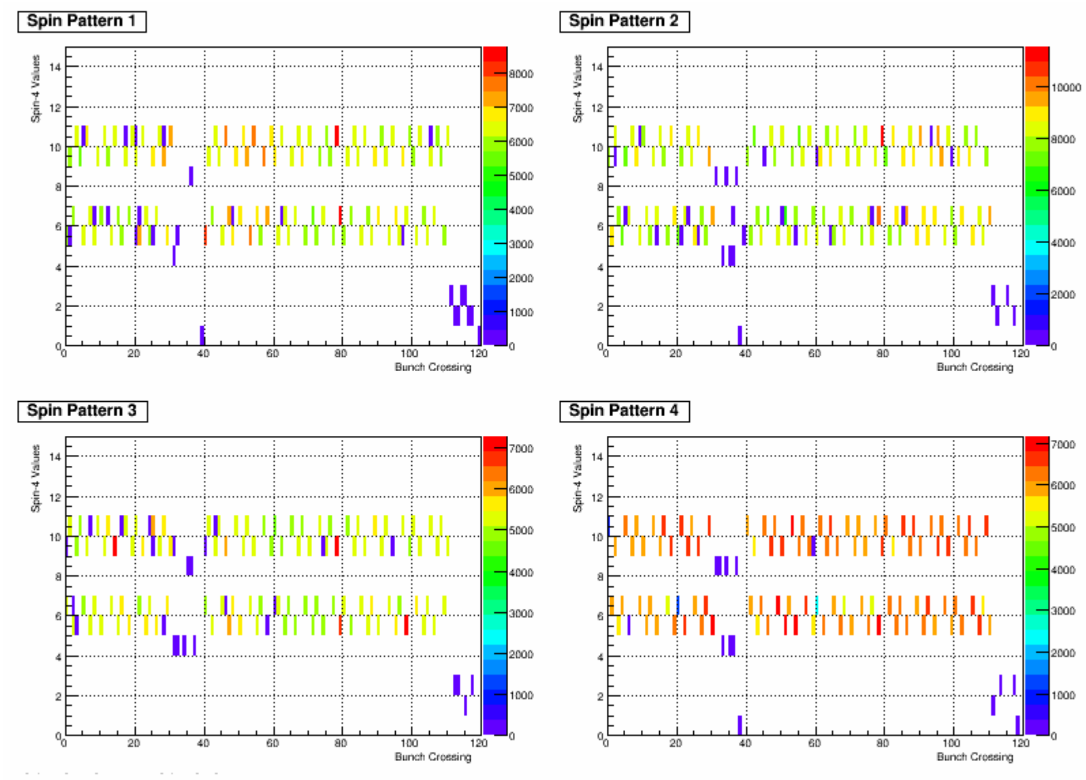

Figure 6.2: Map of which bunch crossings are tagged with which Spin-4 value for each of the four spin patterns shown in table 6.2.

be seen in figure 6.2.

6.3 Relative Luminosity

The final term in equation 6.2 which has not been discussed is the relative luminosity ratio, R_3. As mentioned above, when accessing A_{LL} experimentally, the helicity-dependent yields are used as a surrogate for the helicity-dependent cross sections, and the asymmetry is measured as the difference in the number of di-jets from colliding bunches with $++$ and $--$ helicity combinations versus the number seen from bunches with $+-$ and $-+$ combinations. This is valid as long as all four helicity combinations sample the same luminosity. If one helicity combination saw a higher luminosity, for example, there would be more di-jets arising from that combination producing an unphysical or false asymmetry.

Because RHIC is a real system, there will be variations in intensity between individual bunches, resulting in different helicity combinations sampling different luminosities. The relative luminosity factors are ratios of helicity-combination luminosities, constructed in such a way as to cancel out false asymmetries which would arise from the different combinations sampling different luminosities. Often, the unphysical asymmetries introduced because of different helicity-combination luminosities are larger than the expected signal asymmetry, so getting the relative luminosities correct is an essential ingredient in the extraction of A_{LL}.

During Run IX, the relative luminosities were measured at STAR by looking at the spin-sorted BBC coincidence rates. This observable is advantageous because it has a very high rate, meaning that the statistical uncertainty on the relative luminosity values will be small compared to those of the di-jet yields. Another advantage to using the BBC for the relative luminosity is that the BBC is independent of the detectors used to measure the actual di-jet yields. Relative luminosities were also calculated using the ZDC system (see section 2.1.4) and the differences observed between the BBC and ZDC were used to estimate the systematic error on the quoted relative luminosity values. A detailed account of the extraction of the relative luminosities from the BBCs and ZDCs can be found here: [76].

There are six relative luminosity ratios which are germane to the asymmetry analysis, as defined in equations 6.5. The ratio R_3 is obviously the quantity needed to properly normalize the helicity-sorted yields in an A_{LL} measurement. The other relative luminosities will enter into the calculation of various false asymmetries which will be discussed in section 6.5.

$$R_1 = \frac{\mathcal{L}^{--} + \mathcal{L}^{-+}}{\mathcal{L}^{++} + \mathcal{L}^{+-}} \tag{6.5a}$$

$$R_2 = \frac{\mathcal{L}^{++} + \mathcal{L}^{+-}}{\mathcal{L}^{--} + \mathcal{L}^{-+}} \tag{6.5b}$$

$$R_3 = \frac{\mathcal{L}^{++} + \mathcal{L}^{--}}{\mathcal{L}^{+-} + \mathcal{L}^{-+}} \tag{6.5c}$$

$$R_4 = \frac{\mathcal{L}^{--}}{\mathcal{L}^{++}} \tag{6.5d}$$

$$R_5 = \frac{\mathcal{L}^{-+}}{\mathcal{L}^{++}} \tag{6.5e}$$

$$R_6 = \frac{\mathcal{L}^{+-}}{\mathcal{L}^{++}} \tag{6.5f}$$

During the course of the relative luminosity investigation, it was found that certain bunch crossings had anomalous behavior. Figure 6.3 shows a typical event spectrum versus bunch crossing number. Due to this behavior, several bunches were not used when determining the relative luminosity values, and di-jet events from these bunches have also been removed from this asymmetry analysis. The bunch crossings removed were: 20, 60, 78, 79, and 80. In addition, the bunch crossings corresponding to the times when one of the abort gaps was passing through STAR have also been removed. These are bunches 31-39 and 111-119.

6.4 Trigger Selection and Binning

The di-jet events used in the asymmetry analysis were sorted into the same L2JetHigh and JP1 trigger categories as defined for the cross section analysis (see section 5.1). The JP1 sample contains substantially fewer counts than the L2JetHigh sample, and was only used as a consistency check in the cross section measurement. The asymmetry measurement, unlike the cross section, is statistics limited so both the L2JetHigh and JP1 samples were used in order to get as many counts as possible.

As with the cross section, the A_{LL} values are presented as a function of the di-jet invariant mass. The mass bins retain the same boundaries as were used in the cross section analysis

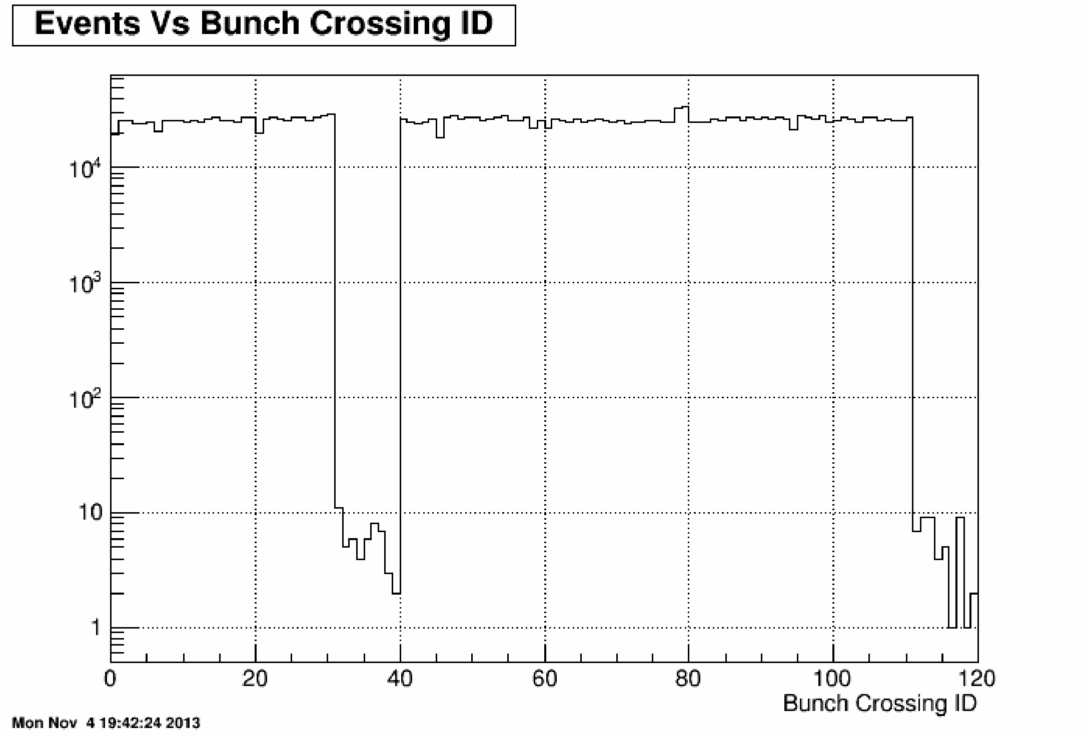

Figure 6.3: Number of events in each bunch crossing for a sample of data. The abort gaps at indices 31-39 and 111-119 are clearly seen.

Bin	Mass Range (GeV)
1	16-19
2	19-23
3	23-28
4	28-34
5	34-41
6	41-58
7	58-82
8*	82-120

Table 6.4: The mass ranges for each bin used in the A_{LL} analysis. Bin 8 was excluded from the final results due to a lack of statistics.

(see table 5.1), but several bins have been combined to reduce the statistical error on the high mass points. Table 6.4 shows the mass binning used for the A_{LL} measurement.

In addition to the full data sample, A_{LL} was determined for di-jets with two jet topologies. The first subsample contains di-jets in which both jets are either in the East half of the BEMC ($-0.8 \leq \eta \leq 0.0$) or the West half of the BEMC ($0.0 \leq \eta \leq 0.8$). The second subsample contains di-jets with one jet in the East half of the BEMC and the other in the West. As described in section 1.2.2, selecting di-jets by where each jet points in the detector will enhance certain initial state kinematics. The East-East plus West-West sample should contain more asymmetric partonic collisions than the East-West sample, for which the partonic momentum fractions should be roughly equal.

6.5 Additional Asymmetries

In addition to the longitudinal double-spin asymmetry (equation 6.2), four other useful asymmetries can be calculated (see equation 6.6). These additional asymmetries are the yellow and blue beam single-spin asymmetries (A_L^Y and A_L^B) and the like and unlike sign double spin asymmetries (A_{LL}^{ls} and A_{LL}^{us}). These four quantities provide checks on the analysis scheme because they are expected to be zero. The A_L^Y, A_L^B, and A_{LL}^{ls} asymmetries all measure parity-violating effects, and are therefore expected to be negligible in this data set. The A_{LL}^{us} asymmetry should be zero as collisions in which the yellow beam has positive helicity and the blue beam has negative helicity should be the same as the reverse case.

These four asymmetry measurements provide crucial cross checks on the A_{LL} measurement because the values for these asymmetries should be very small. Significant deviation from zero for any of the four asymmetries could indicate a problem with the relative luminosity values, or a bug in the asymmetry calculation. Figures 6.4, 6.5, and 6.6 show the four additional asymmetries for the full sample, East-West sample, and East-East+West-West sample, respectively. The additional asymmetries agree, with reasonable χ^2 values, with constant functions and all the fits are consistent with an asymmetry of zero.

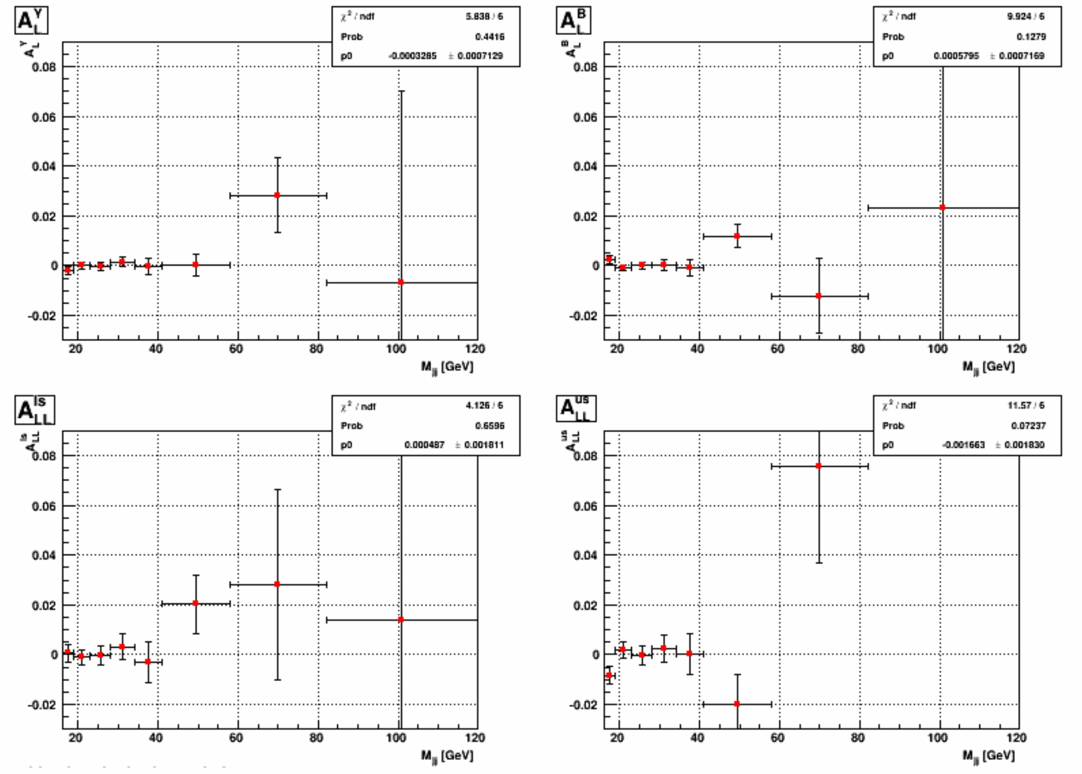

Figure 6.4: The four false asymmetries for the full topological sample. The first 7 data points are fit with a 0th order polynomial, and fit results can be seen in the legend. Note that the points are plotted at bin center and that the horizontal error bars span the width of the bin.

$$A_L^Y = \frac{\sum P_Y \left[(N^{--} + N^{-+}) - R_1 (N^{++} + N^{+-}) \right]}{\sum P_Y^2 \left[(N^{--} + N^{-+}) + R_1 (N^{++} + N^{+-}) \right]} \tag{6.6a}$$

$$A_L^B = \frac{\sum P_B \left[(N^{--} + N^{+-}) - R_2 (N^{++} + N^{-+}) \right]}{\sum P_B^2 \left[(N^{--} + N^{+-}) + R_2 (N^{++} + N^{-+}) \right]} \tag{6.6b}$$

$$A_{LL}^{ls} = \frac{\sum P_Y P_B \left(N^{--} - R_4 N^{++} \right)}{\sum P_Y^2 P_B^2 \left(N^{--} + R_4 N^{++} \right)} \tag{6.6c}$$

$$A_{LL}^{us} = \frac{\sum P_Y P_B \left(R_6 N^{-+} - R_5 N^{+-} \right)}{\sum P_Y^2 P_B^2 \left(R_6 N^{-+} + R_5 N^{+-} \right)} \tag{6.6d}$$

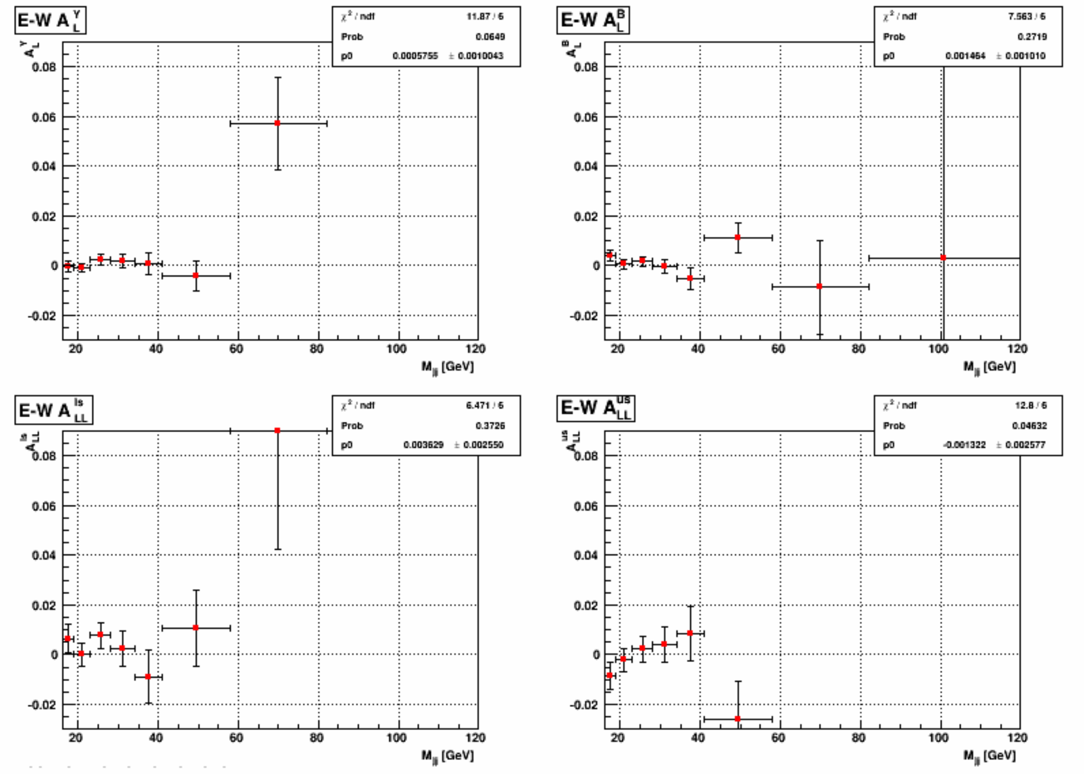

Figure 6.5: The four false asymmetries for the East-West topological sample. Details are presented in the caption of figure 6.4.

6.6 Invariant Mass Shift

Unlike the cross section which drops rapidly, the di-jet A_{LL} is expected to be a slowly varying function of the invariant mass. Because of this, the full unfolding procedure used in the cross section analysis was not used in the extraction of the asymmetry. The determination of the particle or parton level mass of each data point was made by applying a simple mass shift to each point.

The mass shifts were found by comparing the detector level di-jet masses to the masses of matching particle or parton level di-jets in simulation. The procedure for finding particle and parton level di-jets which match to detector level di-jets is described in section 5.2.1. The mass shift for a given bin was calculated by finding the difference between the particle or parton level di-jet mass and the detector level di-jet mass on an event-by-event basis for all di-jets which fall into that given mass bin. Once this difference has been found for each event, the mass shift in a bin is just the mean value of the distribution. Figure 6.7

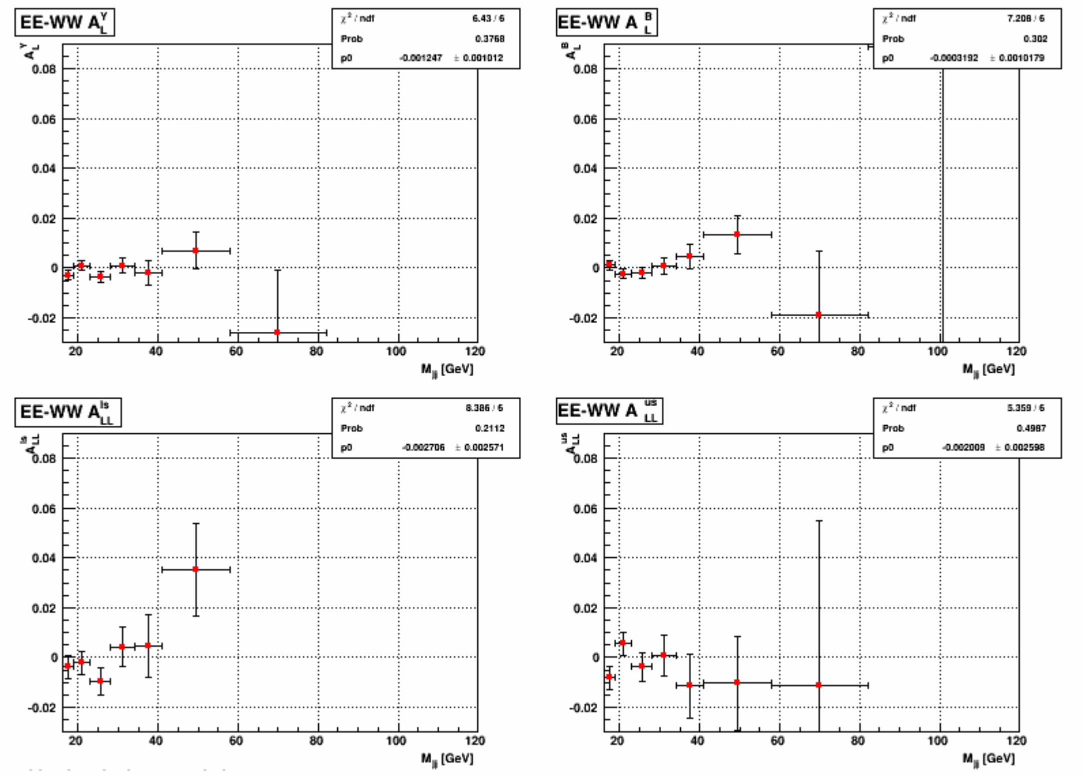

Figure 6.6: The four false asymmetries for the East-East+West-West topological sample. Details are presented in the caption of figure 6.4.

shows a 2-D plot of the L2JetHigh particle minus detector level di-jet mass, versus the latter, along with the mean for each invariant mass bin used in the A_{LL} analysis.

The mass shifts were calculated separately for the L2JetHigh and JP1 trigger samples, for the East-West, East-East+West-West, and combined di-jet topologies, and for the particle and parton levels. To gage the effect that the track finding efficiency has on the mass shifts, the shifts were also calculated using the simulation samples that had 4% and 7% of the reconstructed tracks removed before the jet finder was run (see section 5.3.1). Figures 6.8, 6.9, and 6.10 show the mass shifts for the full, East-West, and East-East+West-West topological divisions, respectively.

The calculated mass shifts were applied to the data points as follows. First, the mass-weighted average position, as well as the number of events which are L2JetHigh and JP1 in each A_{LL} data bin, were found. The mass shift applied to the data was the average of

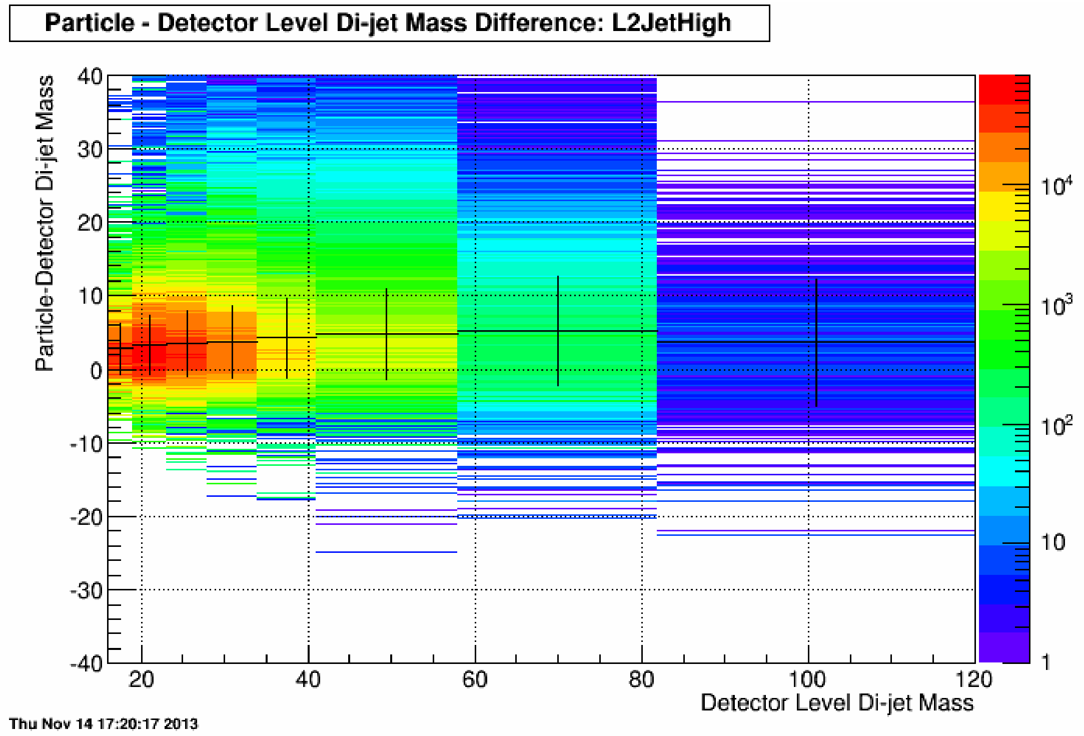

Figure 6.7: Scatter plot showing the event-by-event particle level minus detector level di-jet invariant mass for each A_{LL} mass bin. The data points are placed at the mean Y value and represent the value of the mass shift. Note that the vertical bars on the data points represent the RMS of the distribution, not the error on the mean.

the L2JetHigh and JP1 mass shifts, weighted by the numbers of those types of events seen in the data. This combined mass shift was added to the mass-weighted average position to obtain the corrected position of each data point. This was done independently for the three topological groupings. The particle level mass shifts with no track loss were used in the final analysis, and the difference between the no track loss and 4% track loss shifts was used as a systematic error.

6.7 Results

The di-jet A_{LL} is presented as a function of invariant mass for two independent topological configurations, as well as the combination of the two. The result was obtained using 19.5 pb^{-1} of polarized pp data taken at $\sqrt{s} = 200$ GeV from Run IX. The anti-k$_t$ jet algorithm with a radius of 0.6 was used to reconstruct jets. The two topological configurations are

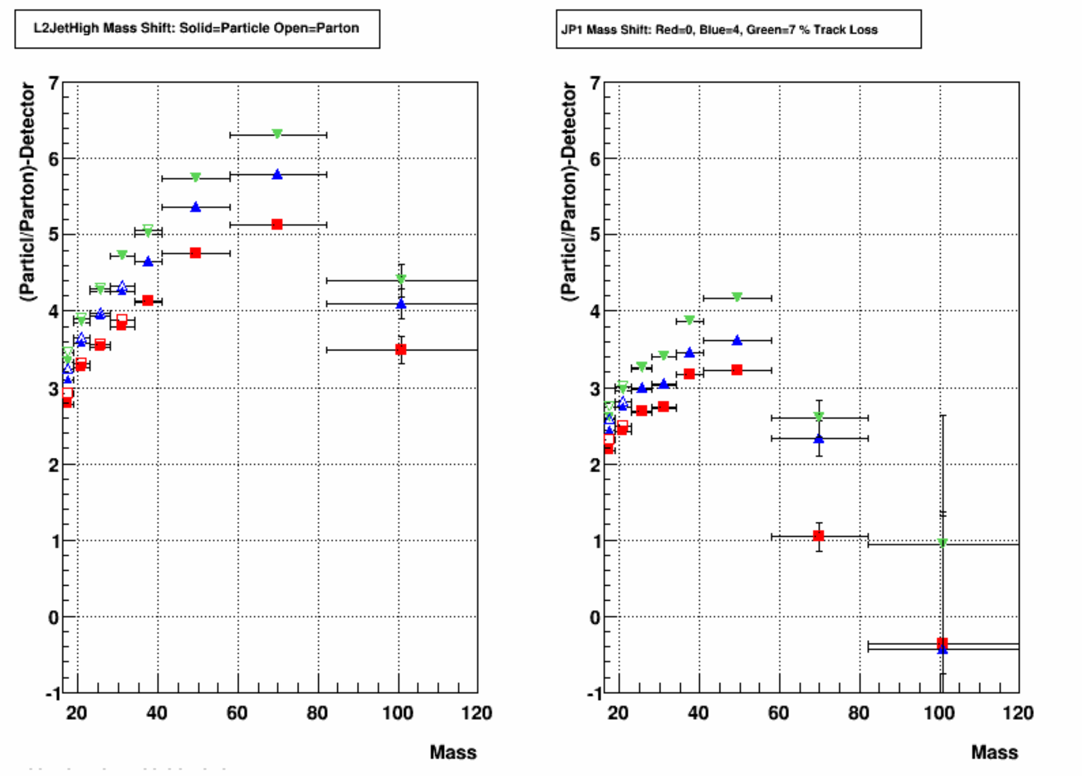

Figure 6.8: Summary of all mass shifts calculated for the full topological sample. The solid shapes represent the particle level shifts and the open shapes represent the parton level shifts. The red squares represent the 0% track-loss shifts, the blue triangles represent the 4% track-loss shifts, and the green inverted triangles represent the 7% track-loss shifts.

East-West and East-East+West-West. The East-West configuration contains those di-jets which have one jet in the East half of the BEMC and one jet in the West, while the East-East+West-West configuration contains those di-jets which have both jets in either the East or West halves of the BEMC. The full topological configuration is simply the sum of the two independent topological samples. Table 6.6 shows the raw number of events in each helicity combination for the East-West and East-East+West-West topologies. A_{LL} is calculated using events from two trigger samples, L2JetHigh and JP1. The raw number of events in each helicity combination for both trigger samples for the full topological configuration can be seen in Table 6.7.

The A_{LL} points were plotted at the mass-weighted average position of each bin. A mass shift was then applied to these average positions, which was determined by taking the

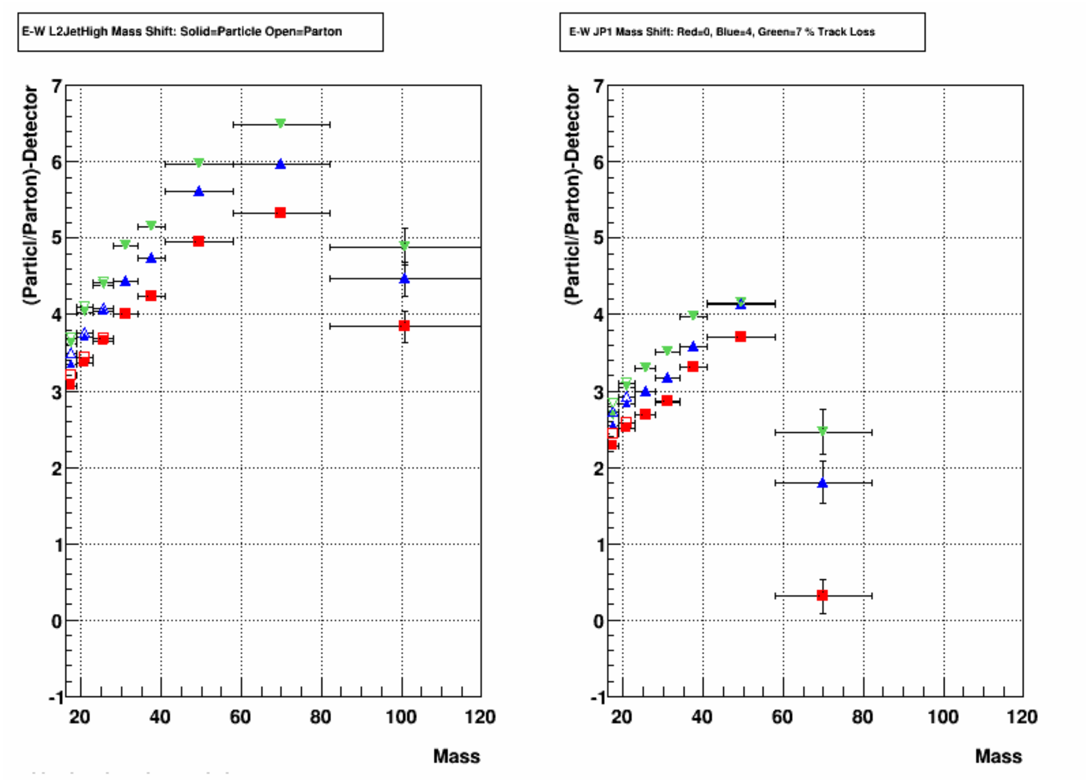

Figure 6.9: Summary of all mass shifts calculated for the East-West topological sample. See caption of figure 6.8 for explanation of symbols.

Bin	Combined		East-West		East-East+West-West	
	L2JetHigh	JP1	L2JetHigh	JP1	L2JetHigh	JP1
1	2.77 ± 0.33	2.17 ± 0.27	3.06 ± 0.28	2.27 ± 0.28	2.60 ± 0.36	2.08 ± 0.26
2	3.25 ± 0.33	2.43 ± 0.31	3.37 ± 0.34	2.51 ± 0.31	3.14 ± 0.32	2.32 ± 0.30
3	3.53 ± 0.41	2.68 ± 0.30	3.65 ± 0.40	2.70 ± 0.30	3.40 ± 0.43	2.65 ± 0.30
4	3.80 ± 0.45	2.73 ± 0.31	4.00 ± 0.43	2.85 ± 0.31	3.56 ± 0.47	2.52 ± 0.30
5	4.11 ± 0.55	3.16 ± 0.29	4.23 ± 0.51	3.32 ± 0.26	3.93 ± 0.59	2.88 ± 0.37
6	4.76 ± 0.61	3.22 ± 0.39	4.96 ± 0.65	3.71 ± 0.42	4.45 ± 0.56	2.29 ± 0.32
7	5.13 ± 0.66	1.04 ± 1.29	5.33 ± 0.65	0.31 ± 1.49	4.75 ± 0.67	2.90 ± 0.52
8	3.49 ± 0.61	-0.4 ± 0.08	3.84 ± 0.62	-2.7 ± 0.31	2.39 ± 0.56	6.55 ± 0.05

Table 6.5: Mass shift values and errors used in the A_{LL} results for each trigger sample in each of the three topological groupings.

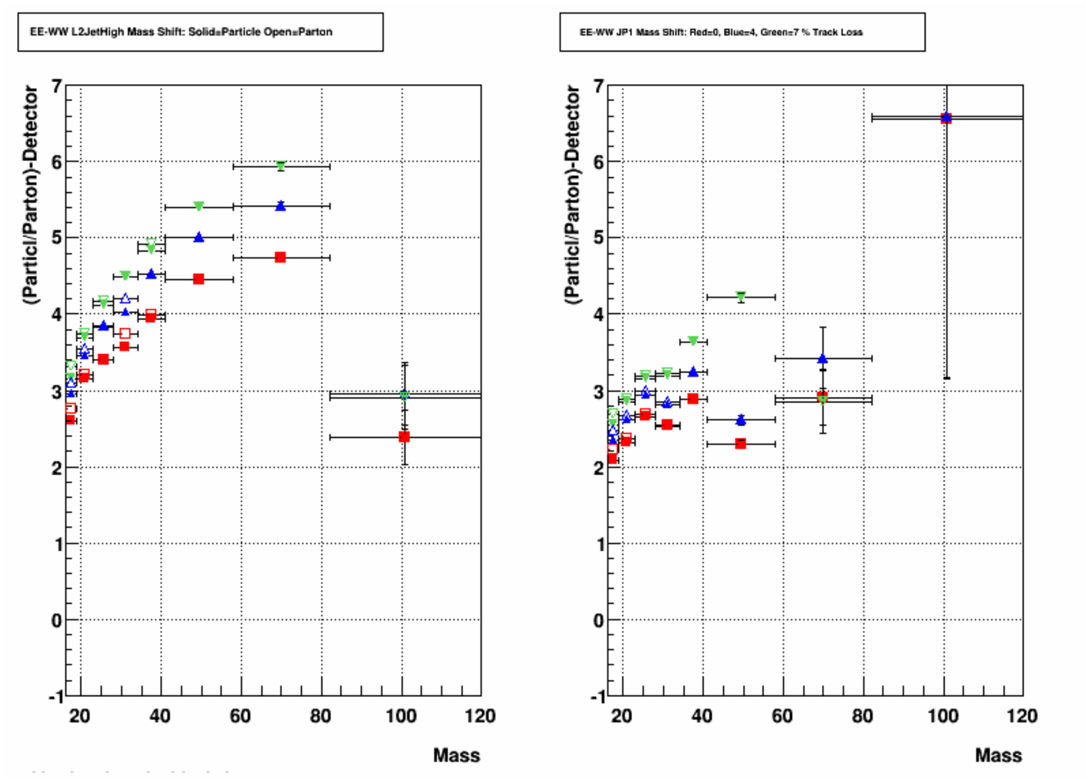

Figure 6.10: Summary of all mass shifts calculated for the East-East+West-West topological sample. See caption of figure 6.8 for explanation of symbols.

Bin	East-West				East-East+West-West			
	N_5	N_6	N_9	N_{10}	N_5	N_6	N_9	N_{10}
1	170417	166968	167888	169011	231915	227451	228962	231486
2	261252	254861	257319	260277	259716	253216	257010	259152
3	199947	194919	197313	198247	171368	167148	168716	171732
4	107479	104039	105538	106861	83672	81756	82762	83189
5	46054	44809	45605	46087	33459	32665	32792	33261
6	23254	22719	22604	22961	15398	14686	14745	15005
7	2404	2241	2433	2266	1261	1215	1218	1317
8	108	98	88	118	39	29	36	26

Table 6.6: Number of events in each helicity combination (see table 6.3) for the two topological configurations.

Bin	L2JetHigh				JP1			
	N_5	N_6	N_9	N_{10}	N_5	N_6	N_9	N_{10}
1	243814	238985	240386	243221	158518	155434	156464	157276
2	410975	399963	405062	408724	109993	108114	109267	110705
3	332052	323607	327226	330897	39263	38460	38803	39082
4	181479	176349	178875	180477	9672	9446	9425	9573
5	77718	75667	76718	77545	1795	1807	1679	1803
6	38322	37107	37023	37634	330	298	326	332
7	3662	3449	3646	3575	3	7	5	8
8	147	127	124	143	0	0	0	1

Table 6.7: Number of events in each helicity combination (see table 6.3) for the two trigger samples. The full topological sample is used.

Bin	Mass Range [GeV/c^2]	Average Mass [GeV/c^2]	Shifted Mass [GeV/c^2]	δ Shift	A_{LL}	δA_{LL}
1	16-19	17.09	19.62	0.43	0.00667	0.00256
2	19-23	20.38	23.46	0.45	0.01051	0.00226
3	23-28	24.71	28.15	0.51	0.01086	0.00268
4	28-34	30.04	33.79	0.54	0.01103	0.00374
5	34-41	36.38	40.47	0.62	0.01283	0.00580
6	41-58	45.79	50.54	0.73	0.02150	0.00836
7	58-82	63.85	68.97	1.45	0.01508	0.02713
8	82-120	88.63	92.11	0.62	0.22785	0.13914

Table 6.8: A_{LL} results for the full topological sample. Shown for each bin are the mass range, mass-weighted average, mass-weighted average plus mass shift, systematic error on mass shift, A_{LL} value, and the statistical error on A_{LL}.

event-weighted average of the L2JetHigh and JP1 mass shifts listed in Table 6.5. The original average bin position and the mass shifts were calculated independently for the three topological samples. The A_{LL} results, along with the original and shifted average masses, can be found in Tables 6.8, 6.9, and 6.10 for the full, East-West, and East-East+West-West topological configurations, respectively.

Bin	Mass Range [GeV/c^2]	Average Mass [GeV/c^2]	Shifted Mass [GeV/c^2]	δ Shift	A_{LL}	δA_{LL}
1	16-19	17.16	19.88	0.40	0.00548	0.00394
2	19-23	20.41	23.57	0.46	0.01189	0.00319
3	23-28	24.72	28.26	0.50	0.00654	0.00365
4	28-34	30.06	34.00	0.53	0.01646	0.00499
5	34-41	36.40	40.61	0.57	0.01215	0.00762
6	41-58	45.86	50.81	0.77	0.01188	0.01075
7	58-82	64.00	69.32	1.62	-0.01797	0.03363
8	82-120	88.64	92.46	0.69	0.29403	0.15923

Table 6.9: A_{LL} results for the East-West topological sample. This table is in the same format as Table 6.8.

Bin	Mass Range [GeV/c^2]	Average Mass [GeV/c^2]	Shifted Mass [GeV/c^2]	δ Shift	A_{LL}	δA_{LL}
1	16-19	17.04	19.45	0.44	0.00753	0.00338
2	19-23	20.35	23.34	0.44	0.00912	0.00320
3	23-28	24.68	28.01	0.53	0.01590	0.00394
4	28-34	30.02	33.54	0.56	0.00408	0.00565
5	34-41	36.36	40.27	0.70	0.01377	0.00895
6	41-58	45.67	50.10	0.64	0.03623	0.01331
7	58-82	63.58	68.33	0.85	0.07671	0.04590
8	82-120	88.61	91.00	0.57	0.01289	0.28613

Table 6.10: A_{LL} results for the East-East+West-West topological sample. This table is in the same format as Table 6.8.

The A_{LL} results for the three topological groups are shown in Figures 6.11, 6.12, 6.13, respectively. Note that an overall scale uncertainty of 6.8% due to uncertainty in the beam polarization measurements is not shown.

As can be seen in figure 6.11, the di-jet A_{LL} lies above zero for the entire measured range in invariant mass (the last point is consistent with zero). Although theory curves are not shown on the plot, the data sit between the 2008 DSSV best fit curve [29] and the older GRSV standard curve [27]. This behavior is qualitatively similar to the inclusive

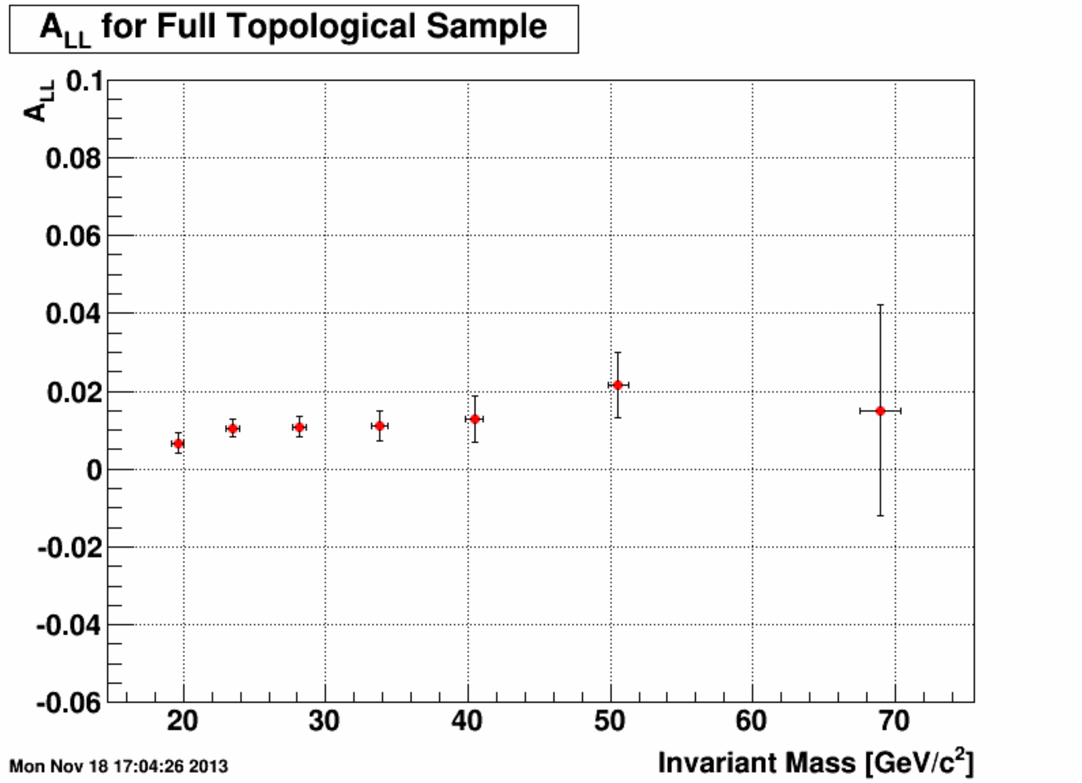

Figure 6.11: The di-jet A_{LL} for the full topological sample.

jet results from 2009 1.7 discussed in section 1.2.1 and thus provides a good consistency check on this result. When analyzed in the DSSV framework like the inclusive jet result, this di-jet A_{LL} result should further strengthen the case for a non-zero gluon polarization in the accessible gluon momentum fraction range while providing better constraints on the shape of $\Delta g(x, Q^2)$ as a function of x.

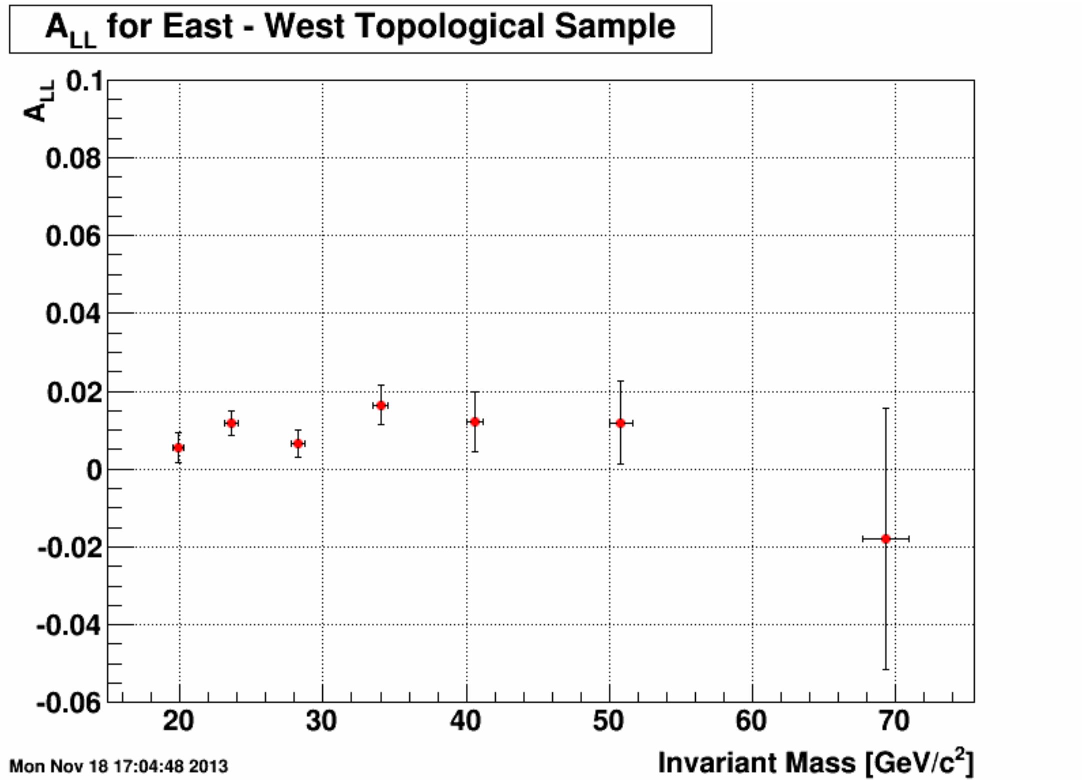

Figure 6.12: The di-jet A_{LL} for the East-West topological sample.

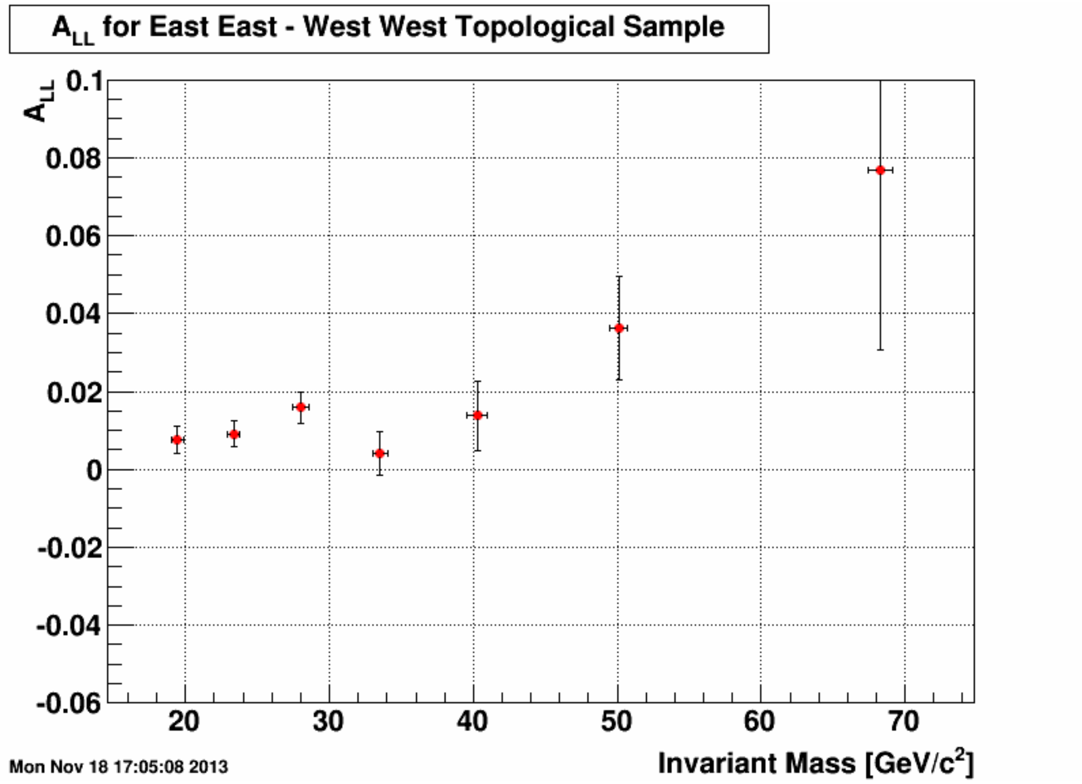

Figure 6.13: The di-jet A_{LL} for the East-East+West-West topological sample.

Chapter 7

Summary and Outlook

The question of how the constituents of the proton contribute to its observed spin is one of the most important outstanding issues in hadronic physics. Polarized DIS measurements have shown that the quark and anti-quark spins can only account for roughly 30% of the proton spin, yet they provide little information on the contributions of gluon spin or orbital angular momentum. Polarized *pp* collisions at RHIC provide a unique probe of the gluon spin contribution, and inclusive jet and pion asymmetry measurements have provided evidence that this contribution may be non-zero over a limited range in gluon momentum fraction. The extension of inclusive jet measurements to di-jet correlation measurements can provide more information on the initial partonic collision kinematics, which will lead to more precise extractions of $\Delta g(x, Q^2)$.

The di-jet cross section and A_{LL} presented above are based on longitudinally polarized *pp* collisions at $\sqrt{s} = 200$ GeV recorded by the STAR detector in 2009. The cross section analysis used 17.1 pb^{-1} of data, and the asymmetry analysis utilized 19.5 pb^{-1}. The measured cross section was found to be in good agreement with established NLO pQCD theoretical predictions, which serves as confirmation that the asymmetry results can be trusted. The di-jet A_{LL} is presented as a function of invariant mass for two independent jet topologies, as well as their combination. The East-West result is derived from di-jet events in which one jet has pseudorapidity $-0.8 \leq \eta < 0.0$ and the other jet has $0.0 \leq \eta < 0.8$. The East-East+West-West sample comes from di-jets where either both jets have $-0.8 \leq \eta < 0.0$ or both jets have $0.0 \leq \eta < 0.8$. The full sample is the combination of the two previous samples. The di-jet A_{LL} appears to be in very good agreement with the results seen from the preliminary 2009 inclusive jet A_{LL}. This agreement provides further evidence for a significant gluon polarization in the x region between 0.05 and 0.2.

The event selection, jet cuts, and di-jet selection criteria used in the analyses presented here were chosen so as to facilitate the future extension of the 2009 cross section and asymmetry measurements into the EEMC. Measurements of the di-jet A_{LL} at more forward rapidities will sample gluons with lower momentum fractions, and thus help constrain $\Delta g(x, Q^2)$ for x values below 0.02 where there is currently very little experimental data. In addition to the data taken in 2009, large longitudinally-polarized pp data-sets were taken in 2012 and 2013, which will be essential for future high precision di-jet A_{LL} analyses that will help to better constrain ΔG.

Appendix A

Detector Calibrations

The analyses presented in this thesis rely primarily on data from three sub-components of the STAR detector, the TPC, BEMC, and EEMC. These sub-systems must all be calibrated in order to yield useful data.

A.1 TPC Calibration

There are a number of calibrations the TPC must undergo in order for it to realize its full capability. The most important calibrations for these analyses are those which affect the p_Ts of reconstructed tracks. Two calibrations which can affect the track p_T are the corrections for Space Charge and Grid Leak (SC&GL) [77]. The SC&GL calibrations correct for the electromagnetic distortion caused by drifting charges from the ionized gas. As part of the SC&GL calibration, the orientations of the inner and outer TPC sectors with respect to each other are allowed to vary. Misalignment of the sectors can change the curvature, and therefore the p_T, of tracks. See A.1 for a cartoon showing how this could be possible.

The SC&GL calibration is performed for each of the 24 TPC sectors for both the Reverse Full Field (RFF) and Full Field (FF) magnetic field configurations. The original production (in library P10ic) exhibited an excess of very high p_T tracks in an isolated region of the TPC in the FF runs but not in the RFF runs (see figure A.2). The region in question is sector 20, which has had calibration problems in the past.

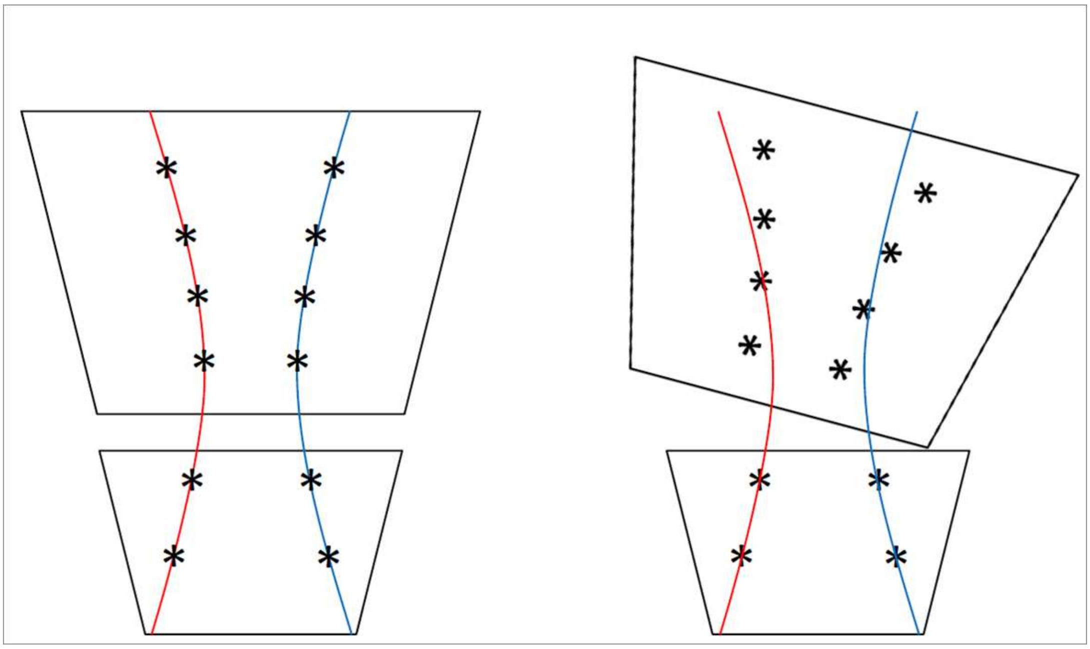

Figure A.1: Cartoon showing how TPC sector misalignment could affect track p_T. The left side of the figure shows properly aligned TPC inner and outer sectors with positively and negatively curved particle trajectories (red and blue curves). The black stars represent padrow hits caused by the particles. The right side of the figure shows an improperly aligned TPC sector. The particle trajectories and padrow hits are in the same position, but the misaligned sectors make the track reconstruction think the padrow hits have more / less curvature.

It was decided that the best way to remedy this issue was to redo the TPC calibrations and reproduce both the RFF and FF data. For the new calibrations (P11id) the TPC geometry was fixed to the values from the year 2000. When the SC&GL calibration was performed, the TPC alignments were no longer free parameters. The new calibration and production removed the excess of high p_T tracks in sector 20 in the FF data A.2.

A.2 BEMC Calibration

The BEMC is a lead-scintillator sampling calorimeter and is used to measure the transverse energy of electromagnetically showering particles (primarily neutral pions). As particles deposit energy in the scintillator, light is produced, detected by a photo mul-

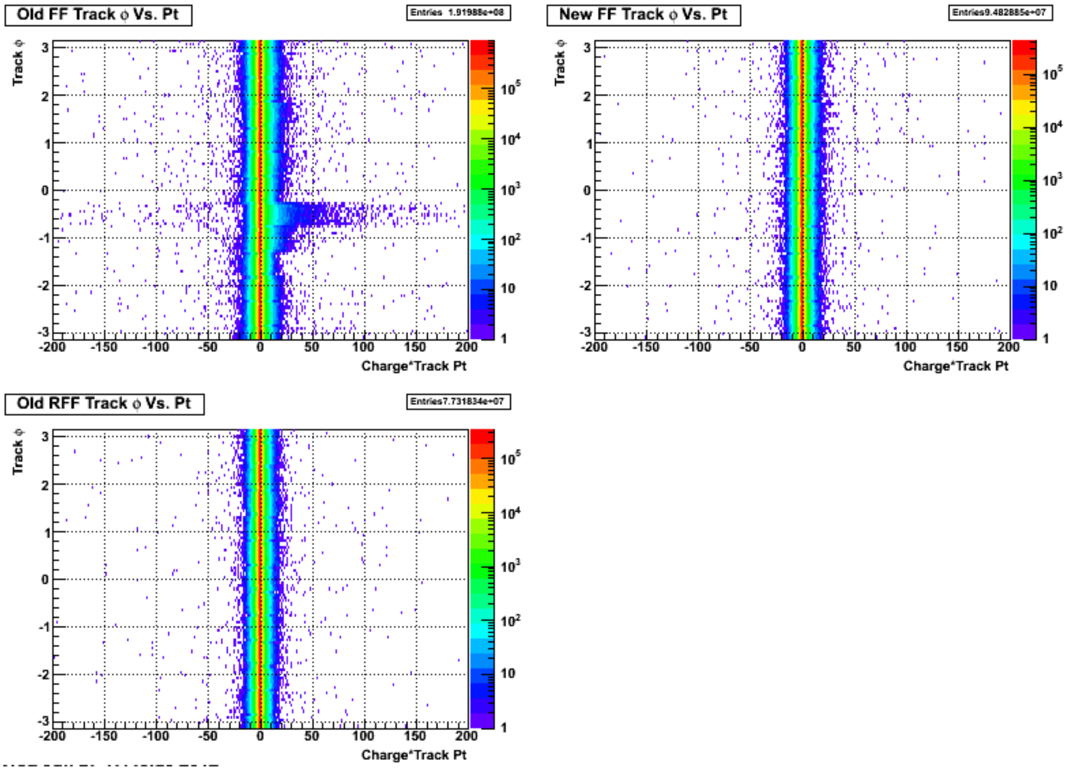

Figure A.2: This figure shows the track phi vs the charge signed transverse momentum. The upper left panel shows the FF tracks from the P10ic production and a large excess of high p_T positively charged tracks can be seen at $\phi = -0.5$. For comparison, the bottom left panel shows the RFF tracks from the same production and the high p_T excess is clearly not present. The upper right panel shows the FF tracks from the P11id production which behave much more like the P10ic RFF tracks.

tiplier tube, and converted into a digital signal. The calibration is used to determine a gain factor which relates the size of the digital signal to the amount of transverse energy which was deposited in the calorimeter. The calibration was set such that a transverse energy deposit of 60 GeV would appear in channel 4096, that is it would saturate a 12-bit ADC.

A two step process is used to calibrate the BEMC (details on the calibration can be found in [78] [79]). First, a relative calibration for each tower was found using the response from minimum ionizing particles (MIPs). MIPs are hadrons (mostly charged pions) which do not shower in the calorimeter. The amount of energy a MIP deposits in the calorimeter is roughly independent of particle species or momentum and was found from test beam data and simulation to have the functional form [80]:

$$\text{MIP} = (264 \pm 4_{stat} \pm 13_{sys}\text{MeV}) \times \left(1 + 0.056\eta^2\right) / \sin\theta \tag{A.1}$$

where η and θ are the pseudorapidity and polar angle, respectively, of a given tower. MIPs are copiously produced in *pp* collisions, so nearly all towers see enough MIP hits to form a useful spectrum.

The second step in the process is the determination of the absolute calibration, which is done using electrons. Electron tracks are selected using $\mathrm{d}E/\mathrm{d}x$ measurements from the TPC and only those tracks which enter and exit the same tower are used in the calibration. The number of electrons identified for the calibration is much lower than the number of MIPs, so an absolute calibration can not be done for each tower using electrons. To aggregate sufficient statistics, the electrons which strike towers read out by the same electronics crate at a given pseudorapidity (there are 8 towers at a given η which are read out by the same crate and there are 40 η rings) are grouped together and the ratio of the energy deposited in a calorimeter tower by an electron to the momentum of the electron as measured by the TPC is formed. The distribution of this ratio for a given crate-pseudorapidity group is then fit with a Gaussian and the offset of the mean from unity is used as the correction to the absolute scale for that particular crate-pseudorapidity grouping. Using the absolute corrections from the electrons and the relative corrections from the MIPs, the gain factors for each tower were found.

The overall uncertainty on the tower energy scale of 3.7% was reached by combining the error quoted in the calibration note [79] due to observed differences in charge sign and TPC field direction with several other sources of uncertainty such as tower edge effects and the linearity of the calorimeter response with respect to energy (private communication with Will Jacobs). The uncertainty on the tower energy scale was also determined as part of the 2009 STAR W cross section analysis [81]. In that analysis, the BEMC calibration was determined by comparing the measured lepton E_T spectrum in the W signal region with a series of 'template' distributions which were generated from GEANT particle level lepton energies multiplied by different energy scale factors. The energy scale factor corresponding to the template which best described the data, as determined by the maximum likelihood method, was used as a correction factor in the W cross section analysis. The quoted uncertainty on the BEMC calibration from this method was 3.6%.

A.3 EEMC Calibration

Like the BEMC, the EEMC must be calibrated in order to relate an observed ADC signal to the actual transverse energy deposited in the calorimeter. Because of the falling TPC tracking efficiency in the EEMC region, calibration methods which rely on the TPC, such as the electron E/p method used in the BEMC, are of limited use. In addition, an absolute calibration based on the reconstruction of the neutral pion invariant mass was not practical before 2009 due to problems with the simulation of the EEMC. Given these issues, the MIP method was chosen for the calibration of the EEMC.

The lack of particle identification from the TPC over a significant amount of the EEMC means that charged hadron tracks could not be tagged as possible MIP candidates, so a calorimeter based MIP identification / calibration scheme was developed. A MIP is identified by requiring an isolated amount of energy, consistent with the expected MIP response, in all layers of a given calorimeter tower. Isolation is enforced by requiring energy deposits in two neighboring SMD strips in each plane while demanding several empty strips on either side. The coincidence between the fired SMD strips in the two layers can also be used to place fiducial cuts on the MIP candidate. With MIP candidates selected, the calibration of a given layer (preshower layers 1 and 2, SMD layers U and V, the postshower layer, and the entire tower) in a given EEMC tower proceeds by requiring an energy deposit consistent with a MIP be present in all other layers. This is done for each layer in the tower and then the entire process is iterated until the gains for each layer converge.

The gains initially used in the 2009 analyses were based on a MIP calibration done using

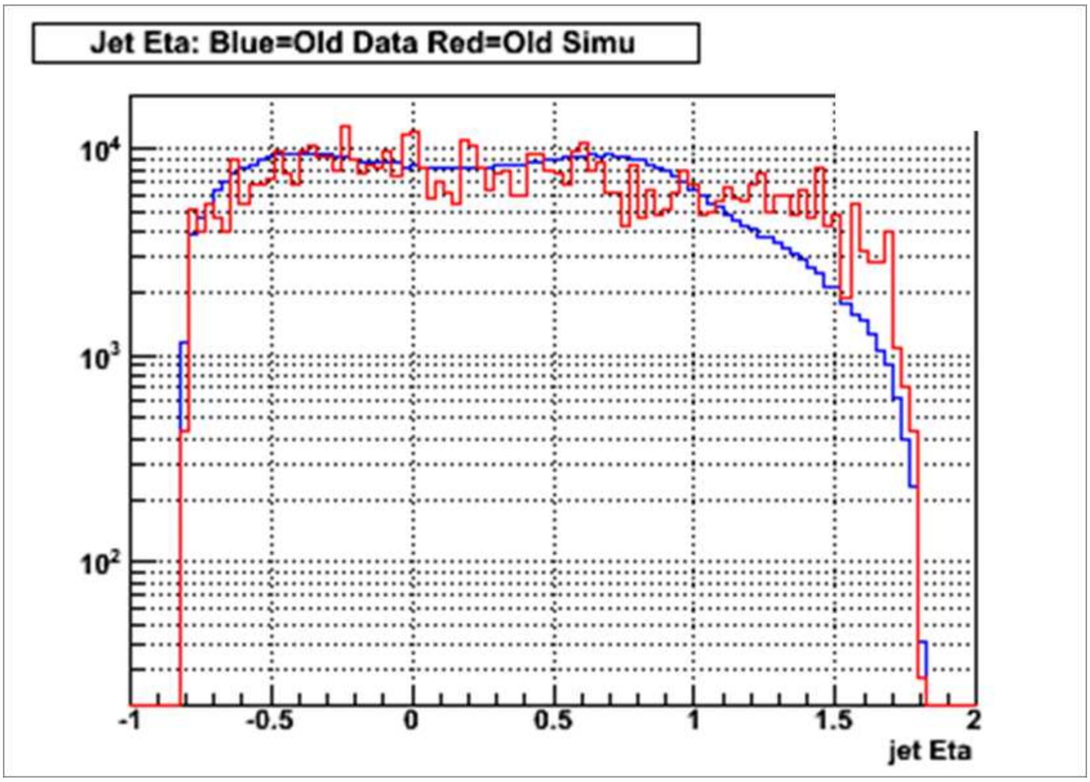

Figure A.3: Data (blue) and simulation (red) comparison for the jet η spectrum using the initial gain values from 2009. Note that this comparison includes all jets found, not just those which are identified as a di-jet.

pp data taken in 2006 (these 2006 gains were adjusted to take into account changes in the PMT high voltages which were made at the end of the 2007 run). Preliminary investigations of neutral pions in the EEMC showed that the reconstructed pion mass from the 2009 data was roughly 8% lower than the pion mass reconstructed using the 2006 data, which matched the PDG value of 135 MeV. In addition, the simulation sample created for the 2009 inclusive jet analysis, which used the initial 2009 gains, showed a large excess of events as compared to the data in the EEMC region (see figure A.3). Both of these observations were qualitatively consistent with a drop of the physical gain of the calorimeter of roughly 7% to 10% as compared to 2006.

Based on the above observations, the EEMC gains initially used for the 2009 analyses were lowered by 7.7% for each tower. The inclusive jet simulation was rerun using the lower gains and the agreement with data became much better (see figure A.4). This

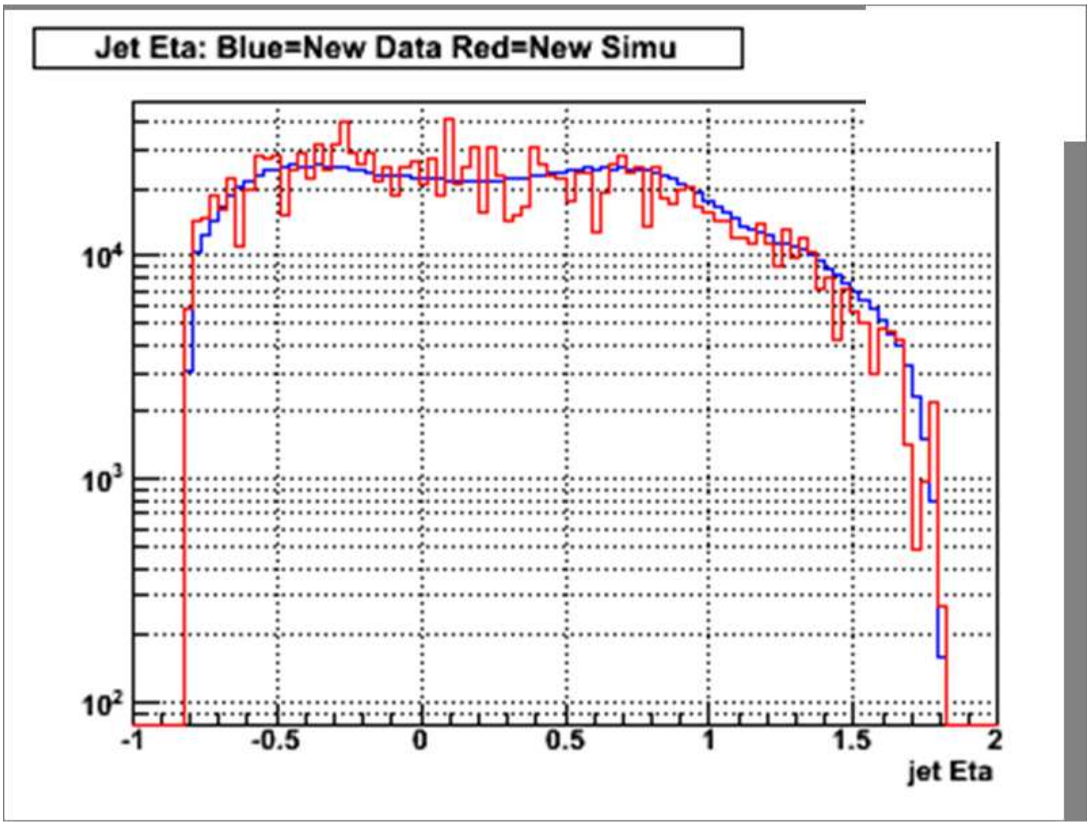

Figure A.4: Data (blue) and simulation (red) comparison for the jet η spectrum using the 2009 EEMC gains which were lowered by 7.7%. Note that this comparison includes all jets found, not just those which are identified as a di-jet.

simulation, which used the lowered EEMC gains, was used in the results presented in the body of this thesis.

The EEMC gain drift between 2006 and 2009 does not greatly effect the mid-rapidity results presented in this thesis as the jet thrust axes were restricted to the BEMC region, however, it will be of primary importance for the future extension of the di-jet cross section and A_{LL} into the EEMC. The data / simulation agreement shown in figure A.4 is for a limited statistics sample and does not take into account issues such as trigger grouping. In addition, there may be pseudorapidity and azimuthal dependencies to the tower gain changes which were not represented in the overall gain shift of 7.7%. More work will need to be done to quantify and mitigate the effect of this gain shift for future EEMC analyses.

Appendix B

List of Runs and Fills

B.1 Cross Section Runs

This is the list of runs used in the cross section analysis.

10120063
10120065
10120078
10120079
10120082
10120085
10120086
10120093
10120097
10120100
10121001
10121017
10121020
10121022
10121029
10121039
10121040
10121043
10121044
10122006
10122007
10122010
10122013
10122014
10122015
10122016
10122017
10122019
10122022
10122023
10122024
10122047
10122048
10122049
10122050
10122054
10122055
10122060
10122061
10122065
10122067
10122071
10122086
10122087
10122095
10122099
10123004
10123007
10123010
10123086
10123087
10123090
10124013
10124014
10124037
10124038
10124044
10124045
10124046
10124049
10124050
10124053
10124110
10124111
10124113
10125001
10125008
10125009
10125010
10125014
10125015
10125016
10125017
10125022
10125023
10125075
10125076
10125080
10125083
10125091
10126003
10126004
10126005
10126012
10126017
10126018
10126019
10126024
10126025
10126026
10126083
10126084
10126087
10126088
10126089
10126090
10127008
10127009
10127011
10128041
10128043
10128046
10128047
10128048
10128049
10128050
10128052
10128053
10128054
10128055
10128056
10128059
10128060
10128061
10128063
10128065
10128066
10128070
10128072
10128094
10128098
10128099
10128100
10128101
10128102
10129003
10129005
10129006

10129007
10129008
10129011
10131039
10131040
10131041
10131042
10131043
10131045
10131047
10131052
10134021
10134024
10134025
10134026
10134027
10134028
10134030
10134035
10134036
10134037
10134044
10134085
10134086
10134101
10134102
10134103
10135001
10135002
10135005
10135006
10135007
10135008
10135009
10135011
10135016
10135017
10135018
10135058
10135059
10135063
10135064
10135065
10135066
10135070
10135072
10135076
10135077
10135081
10135082
10135083
10136001
10136011
10136012
10136017
10136019
10136020
10136021
10136024
10136025
10136026
10136027
10136028
10136030
10136031
10136035
10136036
10136037
10136061
10136063
10136069
10136070
10136071
10136073
10136074
10136077
10136078
10136079
10136092
10136096
10136097
10136099
10136100
10137003
10137004
10137006
10137008
10137045
10137046
10137048
10137049
10138047
10138049
10138052
10138053
10138054
10138055
10138098
10138099
10138100
10139002
10139003
10139007
10139008
10139009
10139010
10139014
10139015
10139017
10139018
10141018
10141019
10141020
10141023
10141025
10141026
10141027
10141030
10141031
10141032
10142029
10142031
10142034
10142035
10142036
10142041
10142042
10142043
10142044
10142047
10142050
10142056
10142057
10142058
10143007
10143008
10143009
10143014
10143015
10143018
10143023
10143025
10143026
10143027
10143029
10143043
10143044
10143045
10143047
10143051
10143052
10143053
10143054
10143058
10143062
10143063
10143064
10143065
10143076
10143077
10143078
10143082
10143083
10143086
10143090
10143092
10143095
10143098
10143099
10143102
10143103
10143104
10143106
10144001
10144002
10144003
10144022
10144026
10144027
10144028
10144029
10144030
10144034
10144035
10144036
10144037
10144044
10144045
10144046
10144072
10144074
10144075
10144076
10144083
10144085
10144087
10144090
10144091
10144092
10144093
10144098
10145011
10145012
10145013
10145016
10145018
10145027
10145030
10145032
10145034
10145036
10145038
10145042
10145046
10145047
10145070
10145072
10145073
10145076
10145078
10145079
10145081
10145082
10146040
10146047
10146048
10146049
10146050
10146051
10146052
10146054
10146055
10146073
10146084
10146086
10146087
10146091
10148002
10148005
10148006

10148021
10148025
10148026
10148027
10148028
10148033
10148034
10148035
10149008
10149012
10149023
10149024
10149025
10149026
10149028
10149031
10149032
10149033
10149034
10149035
10150005
10150008
10150009
10150010
10150011
10150012
10150013
10150018
10150021
10150022
10150024
10150025
10150052
10150053
10150056
10150057
10151001
10151002
10151003
10151004
10151005
10151006
10151034
10151035
10151039
10151040
10151041
10151042
10151043
10151044
10151045
10151047
10152001
10152004
10152005
10152006
10152007
10152008
10152009
10152010
10154060
10154061
10154064
10154065
10154066
10154067
10154083
10155001
10155010
10155014
10155015
10155016
10155019
10155020
10155022
10156031
10156034
10156037
10156038
10156039
10156040
10156058
10156086
10156087
10156090
10156092
10156093
10156095
10156096
10157001
10157004
10157005
10157015
10157016
10157019
10157020
10157021
10157022
10157023
10157027
10157051
10157052
10157056
10157057
10157058
10158001
10158004
10158010
10158013
10158014
10158015
10158016
10158017
10158018
10158021
10158042
10158043
10158047
10158048
10158049
10158050
10158051
10158054
10158055
10158074
10158075
10158076
10158079
10158080
10158082
10158083
10158086
10158087
10158089
10158090
10159006
10159039
10159040
10159044
10159045
10159046
10159048
10159049
10160005
10160006
10160009
10160010
10160011
10160012
10160013
10160014
10160016
10160017
10160071
10160072
10160075
10160077
10160078
10160079
10160081
10160084
10161005
10161006
10161010
10161011
10161014
10161015
10161016
10161019
10161020
10161021
10161025
10161026
10161027
10161030
10162024
10162025
10162029
10162030
10162031
10162032
10162033
10162034
10162035
10162036
10162037
10162038
10162040
10163048
10163051
10163052
10163053
10163054
10163055
10163056
10163059
10164002
10164009
10164010
10164011
10164013
10164016
10164017
10164018
10164025
10164026
10164029
10164030
10164031
10164034
10166061
10166067
10167007
10167008
10167009
10167012
10167013
10167014
10167015
10167016
10167017
10167020
10167048
10167049
10167050
10167053
10167054
10167056
10167057
10167058
10167059
10169005
10169006
10169009
10169010
10169012
10169013
10169014
10169021
10169030

10169031
10169032
10169033
10169041
10169042
10169043
10169044
10169047
10169048
10169049
10169065
10169070
10169074
10169075
10169076
10169077
10169078
10169080
10170003
10170011
10170012
10170013
10170016
10170017
10170018
10170019
10170023
10170024
10170025
10170026
10170029
10170045
10170046
10170047
10170050
10170052
10170053
10170054
10170060
10170061
10170064
10170065
10171011
10171014
10171015
10171016
10171019
10171021
10171022
10171025
10171034
10171036
10171041
10171042
10171043
10171044
10171045
10171048
10171060
10171061
10171069
10171070
10171071
10171078
10172001
10172002
10172003
10172007
10172060
10172061
10172064
10172082
10172083
10172085
10172089
10172090
10172094
10173007
10173008
10173009
10173012
10173013
10173015
10173016
10173017
10173031
10173032
10173033
10173039
10173048
10173051
10173053
10173055
10174012
10174013
10174016
10174023
10174025
10174026
10174027
10174028
10174031
10174044
10174045
10174048
10174049
10174050
10174051
10174052
10174094
10175005
10175008
10175009
10175010
10175011
10175012
10175013
10175014
10175019
10175038
10176001
10176008
10176016
10176017
10176018
10176020
10176022
10176025
10176028
10178022
10178023
10178026
10178029
10178036
10179005
10179006
10179007
10179008
10179009
10179010
10179018
10179019
10179022
10179031
10179032
10179033
10179042
10179043
10179044
10179045
10179085
10179086
10179088
10179096
10179097
10179098
10180003
10180004
10180007
10180021
10180022
10180027
10180028
10180029
10180030

B.2 A_{LL} Runs

The additional runs that were included for the A_{LL} analysis are listed here.

10124062
10124066
10124071
10124072
10124075
10124076
10129048
10129050
10130011
10130012
10130014
10130015
10131009
10131012
10131029
10131075
10131076
10135030
10137051
10137052
10137055
10137059
10137060
10137061
10137063
10137064
10137065
10137066
10137067
10138008
10138011
10138012

10138013
10138014
10138016
10138021
10138022
10138023
10138024
10138025
10138026
10138027
10138030
10138032
10139038
10139040
10139044
10139067
10139068
10139069
10139070
10139073
10139074
10139076
10139077
10139102
10139107
10140002
10140005
10140006
10140007
10140010
10140011
10141010
10141013
10142086
10142093
10142098
10143085
10149087
10150001
10151046
10154068
10155095
10155097
10156004
10156007
10156008
10156009
10156011
10156013
10162006
10162007
10162010
10164057
10164060
10164061
10164062
10164067
10164078
10164079
10164082
10165007
10165008
10165015
10165016
10165017
10165018
10165019
10165022
10165023
10165024
10165027
10170075
10170078
10170081
10170089
10171037
10172077
10172079
10177055
10177056
10177057
10177060
10177061

B.3 Cross Section Fills

The runs used in the cross section analysis come from the following fills.

10682
10683
10684
10685
10688
10689
10690
10695
10696
10700
10703
10704
10706
10708
10712
10713
10729
10746
10748
10753
10754
10755
10756
10758
10761
10763
10773
10777
10781
10782
10783
10784
10785
10786
10789
10790
10791
10800
10806
10814
10820
10825
10826
10854
10855
10866
10869
10870
10875
10876
10877
10878
10880
10881
10884
10889
10890
10904
10919
10920
10921
10932
10935
10937
10951
10952
10953
10954
10955
10959
10960
10961
10963
10964
10967
10968
10970
10971
10973
10986
10987
11001
11002
11003
11005
11006

B.4 A_{LL} Fills

The additional runs used in the A_{LL} analysis come from the following unique fills.

10717
10720
10727
10730
10749
10759
10764
10765
10778
10813
10864
10902
10924
10925
10956
10957
10998

Appendix C

Di-jet Kinematics

In this appendix, the derivation of the invariant mass formula 1.11 as well as the leading order relationships between the initial partonic kinematics and final state di-jets will be presented.

C.1 Invariant Mass Formula

The invariant mass formula used in the cross section and asymmetry analyses is simply the invariant mass of a relativistic system represented by two 4-vectors: $M^2 = (\mathcal{P}_3 + \mathcal{P}_4)^2$. Here $\mathcal{P}_3$ and $\mathcal{P}_4$ are the momentum 4-vectors of the two outgoing jets. For our purposes, it is more convenient to express the 4-vector in terms of the transverse mass, rapidity, transverse momentum, and azimuthal angle as in equation C.1.

$$\mathcal{P} = \begin{bmatrix} m_T \cosh y \\ p_T \cos\phi \\ p_T \sin\phi \\ m_T \sinh y \end{bmatrix} \tag{C.1}$$

Here $m_T \equiv \sqrt{m^2 + p_x^2 + p_y^2}$ is the transverse mass and $y \equiv \frac{1}{2}\ln\left(\frac{E+p_z}{E-p_z}\right)$ is the rapidity. Using the definitions for the transverse mass and rapidity, it is easy to show that $m_T \cosh y = E$ and $m_T \sinh y = p_z$.

There are three terms which need to be evaluated when calculating the mass: $\mathcal{P}_3^2$, $\mathcal{P}_4^2$, and $2\mathcal{P}_3 \cdot \mathcal{P}_4$. The first two terms are the masses of the two outgoing jets:

$$\begin{aligned}
\mathcal{P}^2 &= m_T^2 \cosh^2 y - p_T^2 \cos^2 \phi - p_T^2 \sin^2 \phi - m_T^2 \sinh^2 y \\
&= m_T^2 \left(\cosh^2 y - \sinh^2 y\right) - p_T^2 \left(\cos^2 \phi + \sin^2 \phi\right) \\
&= m^2 + p_x^2 + p_y^2 - p_x^2 - p_y^2 \\
&= m^2
\end{aligned}$$

The last term is the combination of $\mathcal{P}_3$ and $\mathcal{P}_4$:

$$\begin{aligned}
2\mathcal{P}_3 \cdot \mathcal{P}_4 &= 2\left[m_{T3} m_{T4} \left(\cosh y_3 \cosh y_4 - \sinh y_3 \sinh y_4\right)\right] \\
&\quad - 2\left[p_{T3} p_{T4} \left(\cos \phi_3 \cos \phi_4 + \sin \phi_3 \sin \phi_4\right)\right] \\
&= 2\left[\sqrt{m_3^2 + p_{T3}^2}\sqrt{m_4^2 + p_{T4}^2} \cosh\left(y_3 - y_4\right) - p_{T3} p_{T4} \cos\left(\phi_3 - \phi_4\right)\right]
\end{aligned}$$

Putting the above expressions together, we get the invariant mass formula:

$$M = \left[m_3^2 + m_4^2 + 2\sqrt{m_3^2 + p_{T3}^2}\sqrt{m_4^2 + p_{T4}^2} \cosh\left(y_3 - y_4\right) - 2 p_{T3} p_{T4} \cos\left(\phi_3 - \phi_4\right)\right]^{\frac{1}{2}} \tag{C.4}$$

C.2 Leading Order Kinematics

This section discusses the kinematics of relativistic 2 → 2 scattering and derives the results shown in equation 1.10. There are two relevant reference frames in the problem: the lab frame (which is also the center of momentum frame of the proton - proton system), and the center of momentum frame of the colliding partons. First, the kinematics of the colliding partons will be found in the lab-frame, then they will be found in the COM frame. Next, the kinematics of the scattered partons will be found in the COM and lab frames.

Assuming no intrinsic transverse motion and massless partons, the initial state in the lab frame can be expressed as:

$$\mathcal{P}_1 = \frac{\sqrt{s}}{2}\begin{bmatrix} x_1 \\ 0 \\ 0 \\ x_1 \end{bmatrix} \qquad \mathcal{P}_2 = \frac{\sqrt{s}}{2}\begin{bmatrix} x_2 \\ 0 \\ 0 \\ -x_2 \end{bmatrix} \tag{C.5}$$

We define the total 4-momentum of the initial system as $q \equiv \mathcal{P}_1 + \mathcal{P}_2$:

$$q = \frac{\sqrt{s}}{2} \begin{bmatrix} x_1 + x_2 \\ 0 \\ 0 \\ x_1 - x_2 \end{bmatrix} \tag{C.6}$$

The invariant mass of the system is then given by the square root of q^2:

$$M = \sqrt{q^2} = \sqrt{\frac{s}{4}\left[\left(x_1 + x_2\right)^2 - \left(x_1 - x_2\right)^2\right]} = \sqrt{s x_1 x_2} \tag{C.7}$$

A relationship between the rapidity of the system and the partonic momentum fractions can be found by using the fact that the hyperbolic sine and cosine of the rapidity can be expressed in terms of the 0th and 3rd components of q:

$$\cosh y = \frac{q^0}{\sqrt{\left(q^0\right)^2 - \left(q^3\right)^2}} = \frac{E}{\sqrt{E^2 - p_z^2}} = \frac{1}{2}\frac{x_1 + x_2}{\sqrt{x_1 x_2}} \tag{C.8a}$$

$$\sinh y = \frac{\left(q^3\right)^2}{\sqrt{\left(q^0\right)^2 - \left(q^3\right)^2}} = \frac{p_z}{\sqrt{E^2 - p_z^2}} = \frac{1}{2}\frac{x_1 - x_2}{\sqrt{x_1 x_2}} \tag{C.8b}$$

The rapidity can be isolated by using the identity $\mathrm{e}^y = \sinh y + \cosh y$:

$$\mathrm{e}^y = \frac{1}{2}\frac{x_1 + x_2}{\sqrt{x_1 x_2}} + \frac{1}{2}\frac{x_1 - x_2}{\sqrt{x_1 x_2}} = \left(\frac{x_1}{x_2}\right)^{\frac{1}{2}}$$

$$y = \ln\left(\frac{x_1}{x_2}\right)^{\frac{1}{2}} = \frac{1}{2}\ln\left(\frac{x_1}{x_2}\right) \tag{C.9a}$$

With the initial state determined in the lab frame, the next step is to explore the initial state in the center of momentum frame. The COM frame is obtained by applying a Lorentz transformation with the rapidity factor y to the lab frame expressions. The Lorentz transformation is given by:

$$\Lambda\left(-y\right) = \begin{bmatrix} \cosh y & 0 & 0 & -\sinh y \\ 0 & 1 & 0 & 0 \\ 0 & 0 & 1 & 0 \\ -\sinh y & 0 & 0 & \cosh y \end{bmatrix} = \frac{1}{2\sqrt{x_1 x_2}} \begin{bmatrix} x_1 + x_2 & 0 & 0 & -x_1 + x_2 \\ 0 & 1 & 0 & 0 \\ 0 & 0 & 1 & 0 \\ -x_1 + x_2 & 0 & 0 & x_1 + x_2 \end{bmatrix} \tag{C.10}$$

The transformation above can be checked by applying it to the total 4-momentum q of the lab system and ensuring that the resulting system is at rest:

$$q^* = \Lambda\left(-y\right) q = \frac{\sqrt{s}}{4\sqrt{x_1 x_2}} \begin{bmatrix} x_1+x_2 & 0 & 0 & -x_1+x_2 \\ 0 & 1 & 0 & 0 \\ 0 & 0 & 1 & 0 \\ -x_1+x_2 & 0 & 0 & x_1+x_2 \end{bmatrix} \begin{bmatrix} x_1+x_2 \\ 0 \\ 0 \\ x_1-x_2 \end{bmatrix} = \begin{bmatrix} \sqrt{s x_1 x_2} \\ 0 \\ 0 \\ 0 \end{bmatrix} \tag{C.11}$$

We see that the total 4-momentum in the COM frame, q^*, has no 3-momentum component and the energy term is just the invariant mass of the system. This indicates that the transformation $\Lambda(-y)$ has the effect expected. The COM expressions for the individual parton 4-momenta are found by applying the same Lorentz transformation to the lab frame 4-momenta $\mathcal{P}_1$ and $\mathcal{P}_2$. The COM expressions are:

$$\mathcal{P}_1^* = \Lambda\left(-y\right)\mathcal{P}_1 = \frac{\sqrt{s x_1 x_2}}{2} \begin{bmatrix} 1 \\ 0 \\ 0 \\ 1 \end{bmatrix} \qquad \mathcal{P}_2^* = \Lambda\left(-y\right)\mathcal{P}_2 = \frac{\sqrt{s x_1 x_2}}{2} \begin{bmatrix} 1 \\ 0 \\ 0 \\ -1 \end{bmatrix} \tag{C.12}$$

When describing the final state, it is easier to start in the COM frame so that symmetry arguments can be used to relate the 4-momenta of the scattered partons. The 4-momenta of the outgoing partons can be expressed in terms of transverse momentum, rapidity, and azimuthal angle as in equation C.1 (we assume that the partons are massless so $m_T = p_T$):

$$\mathcal{P}_3^* = p_T \begin{bmatrix} \cosh y^* \\ \cos\phi \\ \sin\phi \\ \sinh y^* \end{bmatrix} \qquad \mathcal{P}_4^* = p_T \begin{bmatrix} \cosh y^* \\ -\cos\phi \\ -\sin\phi \\ -\sinh y^* \end{bmatrix} \tag{C.13}$$

Again, the transverse momenta and rapidities of the two scattered partons are equal in magnitude and opposite in direction due to the symmetry of the system in the COM frame. Just as the initial state was transformed from the lab frame to the COM frame by the Lorentz transformation $\Lambda\left(-y\right)$, the final state COM expressions above can be expressed in the lab frame by the application of the inverse transformation:

$$\Lambda\left(y\right)=\begin{bmatrix}\cosh y & 0 & 0 & \sinh y\\ 0 & 1 & 0 & 0\\ 0 & 0 & 1 & 0\\ \sinh y & 0 & 0 & \cosh y\end{bmatrix} \tag{C.14}$$

Applying $\Lambda\left(y\right)$ to $\mathcal{P}_3^*$ and $\mathcal{P}_4^*$ gives:

$$\mathcal{P}_3=\Lambda\left(y\right)\mathcal{P}_3^*=p_T\begin{bmatrix}\cosh y & 0 & 0 & \sinh y\\ 0 & 1 & 0 & 0\\ 0 & 0 & 1 & 0\\ \sinh y & 0 & 0 & \cosh y\end{bmatrix}\begin{bmatrix}\cosh y^*\\ \cos\phi\\ \sin\phi\\ \sinh y^*\end{bmatrix}=p_T\begin{bmatrix}\cosh\left(y+y^*\right)\\ \cos\phi\\ \sin\phi\\ \sinh\left(y+y^*\right)\end{bmatrix} \tag{C.15a}$$

$$\mathcal{P}_4=\Lambda\left(y\right)\mathcal{P}_4^*=p_T\begin{bmatrix}\cosh y & 0 & 0 & \sinh y\\ 0 & 1 & 0 & 0\\ 0 & 0 & 1 & 0\\ \sinh y & 0 & 0 & \cosh y\end{bmatrix}\begin{bmatrix}\cosh y^*\\ -\cos\phi\\ -\sin\phi\\ -\sinh y^*\end{bmatrix}=p_T\begin{bmatrix}\cosh\left(y-y^*\right)\\ -\cos\phi\\ -\sin\phi\\ \sinh\left(y-y^*\right)\end{bmatrix} \tag{C.15b}$$

The above expressions for $\mathcal{P}_3$ and $\mathcal{P}_4$ show that the expressions for the rapidities of the of the outgoing particles are:

$$y_3=y+y^* \tag{C.16a}$$

$$y_4=y-y^* \tag{C.16b}$$

With expressions for the incoming and outgoing partons in both the lab and COM frames, the next step is to relate the initial kinematics in the lab frame to the outgoing kinematics measured in the lab frame. First, the incoming parton momenta will be expressed in terms of final state parameters, then, it will be seen that the rapidity of the system can be expressed in terms of the rapidities of the outgoing particles, and finally, the COM scattering angle will be determined.

The first step of in finding the initial momenta fractions is to express the initial 4-momenta in the COM frame in terms of p_T and the COM rapidity. The invariant mass can be related to p_T and y^* by equating the total momentum in the initial and final states in the COM frame:

$$\mathcal{P}_1^* + \mathcal{P}_2^* = q^* = \mathcal{P}_3^* + \mathcal{P}_4^* \rightarrow M = 2p_T \cosh y^* \tag{C.17}$$

As before, the COM expressions are transformed to the lab frame by the $\Lambda(y)$ term:

$$\mathcal{P}_1 = \Lambda(y)\,\mathcal{P}_1^* = p_T \cosh y^* \mathrm{e}^{y} \begin{bmatrix} 1 \\ 0 \\ 0 \\ 1 \end{bmatrix} \qquad \mathcal{P}_2 = \Lambda(y)\,\mathcal{P}_2^* = p_T \cosh y^* \mathrm{e}^{-y} \begin{bmatrix} 1 \\ 0 \\ 0 \\ -1 \end{bmatrix} \tag{C.18}$$

Comparing the above expressions to those in C.5, it is seen that:

$$x_1 = \frac{p_T}{\sqrt{s}} 2 \cosh y^* \mathrm{e}^{y} \tag{C.19a}$$

$$x_2 = \frac{p_T}{\sqrt{s}} 2 \cosh y^* \mathrm{e}^{-y} \tag{C.19b}$$

Using equations C.16, the right hand sides of the above expressions can be expressed purely in terms of the final state lab frame rapidities:

$$2\cosh y^* \mathrm{e}^{y} = \left(\mathrm{e}^{y^*} + \mathrm{e}^{-y^*}\right)\mathrm{e}^{y} = \left(\mathrm{e}^{y+y^*} + \mathrm{e}^{y-y^*}\right) = \left(\mathrm{e}^{y_3} + \mathrm{e}^{y_4}\right)$$

$$2\cosh y^* \mathrm{e}^{y} = \left(\mathrm{e}^{y^*} + \mathrm{e}^{-y^*}\right)\mathrm{e}^{-y} = \left(\mathrm{e}^{-y+y^*} + \mathrm{e}^{-y-y^*}\right) = \left(\mathrm{e}^{-y_3} + \mathrm{e}^{-y_4}\right)$$

This leads to the final expressions for x_1 and x_2 in terms of measurable quantities (note that in equations 1.10, $y = \eta$ and the transverse momenta which should strictly be equal are allowed to depend on the jet):

$$x_1 = \frac{p_T}{\sqrt{s}} \left(\mathrm{e}^{y_3} + \mathrm{e}^{y_4}\right) \tag{C.21a}$$

$$x_2 = \frac{p_T}{\sqrt{s}} \left(\mathrm{e}^{-y_3} + \mathrm{e}^{-y_4}\right) \tag{C.21b}$$

With expressions for x_1 and x_2, the rapidity of the system as shown in equation C.9 can be expressed in terms of the rapidities of the outgoing partons in the lab frame:

$$y = \frac{1}{2}\ln\left(\frac{x_1}{x_2}\right) = \frac{1}{2}\ln\left(\frac{\mathrm{e}^{y_3} + \mathrm{e}^{y_4}}{\mathrm{e}^{-y_3} + \mathrm{e}^{-y_4}}\right) = \frac{y_3 + y_4}{2} \tag{C.22}$$

The final relation shown in equation 1.10 equates the final state rapidities and the COM scattering angle θ^*. θ^* is the angle the outgoing particle makes with the beam. The cosine of the COM scattering angle can be expressed in terms of the third component and magnitude of the vector part of the final state COM 4-momentum C.13:

$$\cos\theta^* = \frac{\sinh y^*}{\sqrt{\cos^2\phi + \sin^2\phi + \sinh^2 y^*}} = \tanh y^* \tag{C.23}$$

Solving equations C.16 simultaneously for y^* yields: $y^* = (y_3 - y_4)/2$. Using this, the final relation is recovered:

$$\cos\theta^* = \tanh\left(\frac{y_3 - y_4}{2}\right) \tag{C.24}$$

Appendix D

A_{LL} Formula and Error Derivation

The first section of this appendix details the derivation of the A_{LL} formula presented in equation 6.2 which is appropriate for the combination of many individual measurements. The second section outlines the derivation of the statistical error formula for A_{LL}. In both cases, the assumptions inherent in the formulas will be made explicit. The derivation of the A_{LL} formula is closely based on arguments laid out by Scott Wissink in private communication and the derivation of the A_{LL} error formula is based on standard error propagation techniques which can be found in most books on statistical methods, such as [82].

D.1 Asymmetry Formula Derivation

The final A_{LL} values shown in this dissertation are the result of the combination of many individual measurements (each run is considered and independent measurement). The asymmetry for an individual measurement can be expressed schematically as:

$$A_i = \frac{1}{P_i} \frac{N_i^+ - R_i N_i^+}{N_i^+ + R_i N_i^+} \tag{D.1}$$

where P, $N^{+/-}$, and R are the appropriate polarizations, spin-sorted yields, and relative luminosity factors, respectively. The best value for the asymmetry (denoted $\bar{A}$) based on multiple measurements of A can be found using the maximum likelihood method, which requires the minimization of the function:

$$\chi^2 \equiv \sum_{i=1}^{N} \left(\frac{x_i - \bar{x}}{\sigma_i} \right)^2 \tag{D.2}$$

with respect to $\bar{x}$. Here, σ_i is the error on an individual measurement x_i. Doing the minimization yields the following expression for $\bar{x}$:

$$\bar{x} = \frac{\sum_i \left(x_i/\sigma_i^2\right)}{\sum_i \left(1/\sigma_i^2\right)} \tag{D.3}$$

Plugging equation D.1 into D.3 gives an expression for the best value of the asymmetry using a number of independent measurements:

$$\bar{A} = \frac{\sum_i \left(A_i/\sigma_{A_i}^2\right)}{\sum_i \left(1/\sigma_{A_i}^2\right)} \tag{D.4}$$

The exact uncertainty on A_i is a messy function and finding the uncertainty can be difficult when the yields are small. Things can be simplified immensely if it is assumed that the fractional errors on the polarization and relative luminosity terms are small compared to the fractional error on the yield asymmetry itself. With these assumptions, it is easy to show, using standard error propagation techniques, that the uncertainty on an A_i can be expressed (with the run index i dropped for clarity):

$$\sigma_A^2 = \frac{1}{P^2\left(N^+ + RN^-\right)} \left[(1-\epsilon)^2 \sigma_{N^+}^2 + (1+\epsilon)^2 R^2 \sigma_{N^-}^2 \right] \tag{D.5}$$

where $\epsilon \equiv P \times A$. So as long as the size of the yield asymmetry is small, the ϵ term in the above equation can be neglected. In addition, if the relative luminosity R is close to unity, the numerator and denominator have equivalent form. Finally, the error on the yield is assumed to be the square root of the yield, such that $\sigma_N^2 = N$. Using the above assumptions, equation D.5 for the error on the asymmetry can be expressed as:

$$\sigma_A^2 \approx \frac{1}{P^2\left(N^+ + RN^-\right)} \tag{D.6}$$

Plugging equation D.6 into the expression for the asymmetry, equation D.4, yields:

$$\bar{A} = \frac{\sum_i P_i \left(N_i^+ - R_i N_i^-\right)}{\sum_i P_i^2 \left(N_i^+ + R_i N_i^-\right)} \tag{D.7}$$

Substituting the polarization, yield, and relative luminosity terms appropriate for A_{LL} into the above equation yields the expression for A_{LL} shown in section 6:

$$A_{LL} = \frac{\sum_i P_{Yi} P_{Bi} \left[\left(N_i^{++} + N_i^{--}\right) - R_{3i} \left(N_i^{+-} + N_i^{-+}\right) \right]}{\sum_i P_{Yi}^2 P_{Bi}^2 \left[\left(N_i^{++} + N_i^{--}\right) + R_{3i} \left(N_i^{+-} + N_i^{-+}\right) \right]} \tag{D.8}$$

So it is seen that the above expression for the A_{LL} is valid so long as the fractional uncertainties on the polarizations and relative luminosities are small compared to the fractional uncertainty on the yield asymmetry, the relative luminosity values are close to unity, and finally that the asymmetry itself is small. All of these conditions are satisfied to a good degree by the data used in the asymmetry measurements.

D.2 Asymmetry Error Formula Derivation

With the expression for A_{LL} determined, the next step is to find the expression for the statistical uncertainty. As in the derivation of the asymmetry formula, it is assumed that the errors on the polarization and relative luminosity can be neglected. The asymmetry formula has the following basic form:

$$X = \frac{\sum_i \left[P_i\left(A_i - R_i B_i\right)\right]}{\sum_i \left[P_i^2\left(A_i + R_i B_i\right)\right]} = \frac{P_1\left(A_1 - R_1 B_1\right) + P_2\left(A_2 - R_2 B_2\right) + \cdots}{P_1^2\left(A_1 + R_1 B_1\right) + P_2^2\left(A_2 + R_2 B_2\right) + \cdots} \tag{D.9}$$

where the summation has been explicitly expanded for to two places. The P, R, A, and B terms represent the beam polarization, relative luminosity, and spin-dependent yields, respectively. The statistical uncertainty on the above formula is given by:

$$\sigma_X^2 = \sigma_{A_1}^2\left(\frac{\partial X}{\partial A_1}\right)^2 + \sigma_{A_2}^2\left(\frac{\partial X}{\partial A_2}\right)^2 + \sigma_{B_1}^2\left(\frac{\partial X}{\partial B_1}\right)^2 + \sigma_{B_2}^2\left(\frac{\partial X}{\partial B_2}\right)^2 \tag{D.10}$$

where the σ terms are the statistical errors on the indicated yields ($\sigma_N^2 = N$). After some algebra, the partial derivative terms can be expressed as:

$$\frac{\partial X}{\partial A_1} = \frac{2P_1^3 R_1 B_1 + P_1 P_2^2\left(A_2 + R_2 B_2\right) - P_1^2 P_2\left(A_2 - R_2 B_2\right)}{\left[P_1^2\left(A_1 + R_1 B_1\right) + P_2^2\left(A_2 + R_2 B_2\right)\right]^2} \tag{D.11a}$$

$$\frac{\partial X}{\partial A_2} = \frac{2P_2^3 R_2 B_2 + P_2 P_1^2\left(A_1 + R_1 B_1\right) - P_2^2 P_1\left(A_1 - R_1 B_1\right)}{\left[P_1^2\left(A_1 + R_1 B_1\right) + P_2^2\left(A_2 + R_2 B_2\right)\right]^2} \tag{D.11b}$$

$$\frac{\partial X}{\partial B_1} = \frac{-2P_1^3 R_1 A_1 - P_1^2 P_2 R_1\left(A_2 - R_2 B_2\right) - P_1 P_2^2 R_1\left(A_2 + R_2 B_2\right)}{\left[P_1^2\left(A_1 + R_1 B_1\right) + P_2^2\left(A_2 + R_2 B_2\right)\right]^2} \tag{D.11c}$$

$$\frac{\partial X}{\partial B_2} = \frac{-2P_2^3 R_2 A_2 - P_2^2 P_1 R_2\left(A_1 - R_1 B_1\right) - P_2 P_1^2 R_2\left(A_1 + R_1 B_1\right)}{\left[P_1^2\left(A_1 + R_1 B_1\right) + P_2^2\left(A_2 + R_2 B_2\right)\right]^2} \tag{D.11d}$$

The above expressions for the partial derivative terms look messy, but they can be written quite succinctly in terms of the asymmetry itself (equation D.9). Using the asymmetry expression, the partial derivative terms above can be written as:

$$\frac{\partial X}{\partial A_1} = \frac{P_1 \left(1 - P_1 X\right)}{\left[P_1^2 \left(A_1 + R_1 B_1\right) + P_2^2 \left(A_2 + R_2 B_2\right)\right]^2} \tag{D.12a}$$

$$\frac{\partial X}{\partial A_2} = \frac{P_2 \left(1 - P_2 X\right)}{\left[P_1^2 \left(A_1 + R_1 B_1\right) + P_2^2 \left(A_2 + R_2 B_2\right)\right]^2} \tag{D.12b}$$

$$\frac{\partial X}{\partial B_1} = \frac{-P_1 R_1 \left(1 + P_1 X\right)}{\left[P_1^2 \left(A_1 + R_1 B_1\right) + P_2^2 \left(A_2 + R_2 B_2\right)\right]^2} \tag{D.12c}$$

$$\frac{\partial X}{\partial B_2} = \frac{-P_2 R_2 \left(1 + P_2 X\right)}{\left[P_1^2 \left(A_1 + R_1 B_1\right) + P_2^2 \left(A_2 + R_2 B_2\right)\right]^2} \tag{D.12d}$$

Again, if the asymmetry X itself is small, that term can be neglected in the above expressions. Plugging equations D.12 into the general expression for the uncertainty on the asymmetry (equation D.10), and remembering that the squared uncertainty on a yield is just the yield itself, gives the following formula for the statistical error on the uncertainty:

$$\sigma_X^2 = \frac{P_1^2 A_1 + P_2^2 A_2 + P_1^2 R_1^2 B_1 + P_2^2 R_2^2 B_2}{\left[P_1^2 \left(A_1 + R_1 B_1\right) + P_2^2 \left(A_2 + R_2 B_2\right)\right]^2} \tag{D.13}$$

The formula above was worked out explicitly for the case of two measurements, but can easily be extended to N. The form of the error expression is evident and the summation can be reintroduced to give:

$$\sigma_X^2 = \frac{\sum_i \left[P_i^2 \left(A_i + R_i^2 B_i\right)\right]}{\left[\sum_i P_i^2 \left(A_i + R_i B_i\right)\right]^2} \tag{D.14}$$

Placing the proper beam polarization, relative luminosity, and yield factors into the above equation (and using δ to signify the uncertainty), the expression for the statistical error on A_{LL} presented in section 6 is recovered:

$$\delta A_{LL} = \frac{\left(\sum_i P_{Yi}^2 P_{Bi}^2 \left[\left(N_i^{++} + N_i^{--}\right) + R_{3i}^2 \left(N_i^{+-} + N_i^{-+}\right)\right]\right)^{\frac{1}{2}}}{\sum_i P_{Yi}^2 P_{Bi}^2 \left[\left(N_i^{++} + N_i^{--}\right) + R_{3i} \left(N_i^{+-} + N_i^{-+}\right)\right]} \tag{D.15}$$

As a final exercise, a very simple expression for the statistical error can be found by assuming the beam polarizations are constant and that the relative luminosity is unity. With these assumptions, it is easy to see that the statistical uncertainty can be approximated as:

$$\delta A_{LL} = \frac{1}{P_Y P_B} \frac{1}{\sqrt{N}} \tag{D.16}$$

where P_Y and P_B are the average yellow and blue beam polarizations, respectively, and N is the total di-jet yield. Large discrepancies between this approximation and the errors given by equation D.15 are an indication of a mistake in the calculation of the statistical uncertainties.

Bibliography

[1] F. Halzen and A.D. Martin, *Quarks and Leptons: An Introductory Course in Modern Particle Physics*. John Wiley and Sons, Inc., (1984).

[2] E. Leader and E. Predazzi, *An Introduction to Gauge Theories and Modern Particle Physics*, vol. 1. Cambridge University Press, (1996).

[3] R.E. Taylor, "Deep inelastic scattering: The early years," *Rev. Mod. Phys.*, vol. 63, pp. 573–595, (1991).

[4] H.W. Kendall, "Deep inelastic scattering: Experiments on the proton and the observation of scaling," *Rev. Mod. Phys.*, vol. 63, pp. 597–614, (1991).

[5] J.I. Friedman, "Deep inelastic scattering: Comparisons with the quark model," *Rev. Mod. Phys.*, vol. 63, pp. 615–627, (1991).

[6] R. Hofstadter, "Nuclear and nucleon scattering of high-energy electrons," *Annu. Rev. Nucl. Sci.*, vol. 7, pp. 231–316, (1957).

[7] W.K.H. Panofsky in *Proceedings of the 14th International Conference on High Energy Physics*, (1968).

[8] J. Bjorken, "Asymptotic sum rules at infinite momentum," *Phys. Rev.*, vol. 179, pp. 1547–1553, (1969).

[9] R.P. Feynman, "Very high-energy collisions of hadrons," *Phys. Rev. Lett.*, vol. 23, pp. 1415–1417, (1069).

[10] M. Gell-Mann, "A schematic model of baryons and mesons," *Physics Letters*, vol. 8, pp. 214–215, (1964).

[11] G. Zweig, “An su(3) model for strong interaction symmetry and its breaking.” CERN-8182/Th.401, (1964).

[12] J. Kuti, V.F. Weisskopf, “Inelastic lepton-nucleon scattering and lepton pair production in the relativistic quark-parton model,” *Phys. Rev. D*, vol. 4, p. 3418, (1971).

[13] J. Beringer et al. (Particle Data Group), “Review of particle physics,” *Phys. Rev. D*, vol. 86, p. 010001, (2012).

[14] S.D. Bass, “The proton spin puzzle: Where are we today?,” *Modern Physics Letters A*, vol. 24, pp. 1087–1101, (2009).

[15] S.D. Bass, “The spin structure of the proton,” *Rev. Mod. Phys.*, vol. 77, pp. 1257–1302, (2005).

[16] M. Anselmino, A. Efremov, E. Leader, “The theory and phenomenology of polarized deep inelastic scattering,” *Physics Reports*, vol. 261, pp. 1–124, (1995).

[17] S.E. Kuhn, J.P. Chen, E. Leader, “Spin structure of the nucleon - status and recent results,” *Prog. Part. and Nucl. Phys.*, vol. 63, pp. 1–50, (2009).

[18] E. Leader, *Spin in Particle Physics.* Cambridge University Press, (2005).

[19] J. Ashman et al. (European Muon Collaboration), “A measurement of the spin asymmetry and determination of the structure function g1 in deep inelastic muon-proton scattering,” *Phys. Lett. B*, vol. 206, pp. 364–370, (1988).

[20] J. Ashman et al. (European Muon Collaboration), “An investigation of the spin structure of the proton in deep inelastic scattering of polarised muons on polarised protons,” *Nucl. Phys. B*, vol. 328, pp. 1–35, (1988).

[21] J.R. Ellis and R.L. Jaffe, “A sum rule fof deep inelastic electroproduction from polarized protons,” *Phys. Rev. D*, vol. 9, pp. 1444–1446, (1974).

[22] R.L Jaffe and A. Manohar, “The g1 problem: Deep inelastic electron scattering and the spin of the proton,” *Nucl. Phys. B*, vol. 337, pp. 509–546, (1990).

[23] E. Leader, A.V. Sidorov, D.B. Stamenov, "Impact of CLAS and COMPASS data on polarized parton densities and higher twist," *Phys. Rev. D*, vol. 75, p. 074027, (2007).

[24] E.C. Aschenauer et al., "The RHIC SPIN Program." www.bnl.gov/npp/docs/RHIC-Spin-WriteUp-121105.pdf, (2012).

[25] B.I. Abelev et al. (STAR Collaboration), "Longitudinal double-spin asymmetry and cross section for inclusive jet production in polarized proton collisions at $\sqrt{s} = 200$ GeV," *Phys. Rev. Lett.*, vol. 97, p. 252001, (2006).

[26] B.I. Abelev et al. (STAR Collaboration), "Longitudinal double-spin asymmetry for inclusive jet production in $vecp + \vec{p}$ collisions at $\sqrt{s} = 200$ gev," *Phys. Rev. Lett.*, vol. 100, p. 232003, (2008).

[27] M. Gluck, E. Reya, M. Stratmann, W. Vogelsang, "Models for the polarized parton distributions of the nucleon," *Phys. Rev. D*, vol. 63, p. 094005, (2001).

[28] L. Adamczyk et al. (STAR Collaboration), "Longitudinal and transverse spin asymmetries for inclusive jet production at mid-rapidity in polarized $p{+}p$ collisions at $\sqrt{s}$=200 GeV," *Phys. Rev. D*, vol. 86, p. 032006, (2012).

[29] D. de Florian, R. Sassot, M. Stratmann, W. Vogelsang, "Global analysis of helicity parton densities and their uncertainties," *Phys. Rev. Lett.*, vol. 101, p. 072001, (2008).

[30] D. de Florian, R. Sassot, M. Stratmann, W. Vogelsang, "Extraction of spin-dependent parton densities and their uncertainties," *Phys. Rev. D*, vol. 80, p. 034030, (2009).

[31] M.G. Alekseev et al. (COMPASS Collaboration), "The spin-dependent structure function of the proton g_1^p and a test of the bjorken sum rule," *Phys. Lett. B*, vol. 690, pp. 466–472, (2010).

[32] M. Alekseev et al. (COMPASS Collaboration), "Flavour separation of helicity distributions from deep inelastic muon-deuteron scattering," *Phys. Lett. B*, vol. 680, pp. 217–224, (2009).

[33] M.G. Alekseev et al. (COMPASS Collaboration), "Quark helicity distributions from longitudinal spin asymmetries in muon-proton and muon-deuteron scattering," *Phys. Lett. B*, vol. 693, pp. 227–235, (2010).

[34] D. de Florian, R. Sassot, M. Stratmann, W. Vogelsang, "QCD Spin Physics: Partonic Spin Structure of the Nucleon," (2011). arXiv:1112.0904.

[35] M. Harrison, T. Ludlam, and S. Ozaki, "RHIC project overview," *Nucl. Instrum. Meth A.*, vol. 499, pp. 235–244, (2003).

[36] H. Hahn, E. Forsyth, H. Foelsche, et al., "The RHIC design overview," *Nucl. Instrum. Meth A.*, vol. 499, pp. 245–263, (2003).

[37] I. Alekseev, C. Allgower, M. Bai, et al., "Polarized proton collider at RHIC," *Nucl. Instrum. Meth A.*, vol. 499, pp. 392–414, (2003).

[38] A. Zelenski, J.Allessi, B. Briscoe, et al., "Optically pumped polarized H- ion source for RHIC spin physics," *Rev. Sci. Instrum.*, vol. 73, pp. 888–891, (2002).

[39] C. Adler, A. Denisov, E. Garcia, et al., "The RHIC zero-degree calorimeters," *Nucl. Instrum. Meth A.*, vol. 499, pp. 433–436, (2002).

[40] N.H. Buttimore, B.Z. Kopeliovich, E. Leader, et al., "Spin dependence of high energy proton scattering," *Phys. Rev. D*, vol. 59, p. 114010, (1999).

[41] H. Okada, I.G. Alekseev, A. Bravar, et al., "Measurement of the analyzing power a_N in pp elastic scattering in the CNI region with a polarized atomic hydrogen gas jet target," *Phys. Lett. B*, vol. 638, pp. 450–454, (2006).

[42] A. Bravar, I. Alekseev, G. Bunce, et al., "Spin dependence in polarized $pp \to pp$ and $pc \to pc$ elastic scattering at very low momentum transfer t at RHIC," *Nucl. Phys. B*, vol. 146, pp. 77–81, (2005).

[43] A. Zelenski, A. Bravar, D. Graham, W. Haeberli, et al., "Absolute polarized H-jet polarimeter development, for RHIC," *Nucl. Instrum. Meth A.*, vol. 536, pp. 248–254, (2005).

[44] K.H. Ackermann, N. Adams, C. Adler, et al., "STAR detector overview," *Nucl. Instrum. Meth A.*, vol. 499, pp. 624–632, (2003).

[45] K. Adcox, S.S. Adler, M. Aizama, et al., "PHENIX detector overview," *Nucl. Instrum. Meth A.*, vol. 499, pp. 469–479, (2003).

[46] M. Adamczyk, L. Antvorskov, K. Ashktorab, et al., "The BRAHMS experiment at RHIC," *Nucl. Instrum. Meth A.*, vol. 499, pp. 437–468, (2003).

[47] B.B. Back, M.D. Baker, D.S. Barton, et al., "The PHOBOS detector at RHIC," *Nucl. Instrum. Meth A.*, vol. 499, pp. 603–623, (2003).

[48] M. Anderson, J. Berkovitz, W. Betts, et al., "The STAR time projection chamber: a unique tool for studying high multiplicity events at RHIC," *Nucl. Instrum. Meth A.*, vol. 499, pp. 659–678, (2003).

[49] F. Bergsma, C.O. Blyth, R.L. Brown, et al., "The STAR detector magnet subsystem," *Nucl. Instrum. Meth A.*, vol. 499, pp. 633–639, (2003).

[50] J. Abele, J. Berkovitz, J. Boehm, et al., "The laser system for the STAR time projection chamber," *Nucl. Instrum. Meth A.*, vol. 499, pp. 692–702, (2003).

[51] M. Beddo, E. Bielick, T. Fornek, et al., "The STAR barrel electromagnetic calorimeter," *Nucl. Instrum. Meth A.*, vol. 499, pp. 725–739, (2003).

[52] C.E. Allgower, B.D. Anderson, A.R. Baldwin, et al., "The STAR endcap electromagnetic calorimeter," *Nucl. Instrum. Meth A.*, vol. 499, pp. 740–750, (2003).

[53] C.A. Whitten, "The Beam-Beam Counter: A Local Polarimeter at STAR," in *Polarized Ion Sources, Targest and Polarimetry* (A. Kponou, Y. Makdisi, A. Zelenski, ed.), vol. 980 of *American Institute of Physics Conference Series*, pp. 390–396, feb (2008).

[54] F.S. Bieser, H.J. Crawford, J. Engelage, et al., "The STAR trigger," *Nucl. Instrum. Meth A.*, vol. 499, pp. 766–777, (2003).

[55] J. Beringer et al., "Review of Particle Physics," *Phys. Rev. D.*, vol. 86, p. 010001, (2012).

[56] A. Drees, Z. Xu in *Proceedings of the Particle Accelerator Conference, Chicago*, p. 3120, (2001).

[57] J. Adams et al. (STAR Collaboration), "Transverse-momentum and collision-energy dependence of high-p_T hadron suppression in au+au collisions at ultrarelativistic energies," *Phys. Rev. Lett*, vol. 91, p. 172302, (2003).

[58] T. Sjostrand, S. Mrenna, P. Skands, "PYTHIA 6.4 physics and manual," *JHEP*, vol. 05, p. 026, (2006).

[59] P. Skands, "Tuning monte carlo generators: The perugia tunes," *Phys. Rev. D*, vol. 82, p. 074018, (2010).

[60] "GEANT 3.21, CERN Program Library."

[61] E. Leader, E. Predazzi, *An Introduction to Gauge Theories and Modern Particle Physics*, vol. 2. Cambridge University Press, 1996.

[62] S.D. Ellis, J. Huston, K. Hatakeyama, et al., "Jets in hadron-hadron collisions," *Prog. Part. Nucl. Phys.*, vol. 60, p. 484, (2008).

[63] G.P. Salam, "Towards jetography," *Eur. Phys. J. C*, vol. 67, p. 637, (2010).

[64] A. Ali, G. Kramer, "Jets and QCD: A historical review of the discovery of the quark and gluon jets and its impact on QCD," *Eur. Phys. J. H*, vol. 36, pp. 245–326, (2011).

[65] M. Cacciari, G.P. Salam, G. Soyez, "The anti-kt jet clustering algorithm," *J. High Energy Phys.*, vol. 2008, no. 04, p. 063, (2008).

[66] M. Cacciari, G.P. Salam, G. Soyez, "FastJet user manual," (2011).

[67] B.I. Abelev et al. (STAR Collaboration), "Longitudinal double-spin asymmetry and cross section for inclusive neutral pion production at midrapidity in polarized proton collisions at $\sqrt{s} = 200$ gev," *Phys. Rev. D.*, vol. 80, p. 111108, (2009).

[68] J. Adams et al. (STAR Collaboration), "Identified hadron spectra at large transverse momentum in $p+p$ and $d+$Au collisions at $\sqrt{s_{\mathrm{NN}}} = 200$ gev," *Phys. Lett. B*, vol. 637, pp. 161–169, (2006).

[69] G. Cowan, *Statistical Data Analysis.* Oxford University Press, 1998.

[70] T. Adye in *Proceedings of the PHYSTAT 2011 Workshop on Statistical Issues Related to Discovery Claims in Search Experiments and Unfolding, CERN, Geneva*, pp. 313–318, (2011). hepunx.rl.ac.uk/ adye/software/unfold/RooUnfold.html.

[71] "http://root.cern.ch/drupal."

[72] G. D'Agostini, "A multidimensional unfolding method based on bayes' theorem," *Nucl. Instrum. Meth A.*, vol. 362, pp. 487–498, (1995).

[73] A. Hoecker, V. Kartvelishvili, "SVD Approach to Data Unfolding," *Nucl. Instrum. Meth A*, vol. 372, pp. 469–481, (1996).

[74] J. Pumplin et al., "New generation of parton distributions with uncertainties from global QCD analysis," *JHEP*, vol. 0207, p. 012, (2002).

[75] "www.jlab.org/cdev/."

[76] J. Hayes-Wehle, J. Seele, H. Spinka, B. Surrow, "Relative luminosity analysis for run9 pp 200 GeV running." Internal STAR Note: http://drupal.star.bnl.gov/STAR/starnotes/private/psn0570, (2012).

[77] G. Van Buren et al., "Correcting for distortions due to ionization in the STAR TPC." arXiv:physics/0512157, (2005).

[78] Michael Betancourt et al., "2006 BEMC tower calibration report." Internal STAR Document: https://drupal.star.bnl.gov/STAR/system/files/2006-Calibration-Report_3.pdf, (2009).

[79] Matthew Walker and Michael Betancourt, “2009 BEMC tower calibration report.” Internal STAR Document: https://drupal.star.bnl.gov/STAR/system/files/2009-Calibration-Report.pdf, (2010).

[80] M. Cormier et al., “STAR Barrel Electromagnetic Calorimeter Absolute Calibration Using Minimum Ionizing Particles from Collisions at RHIC.” Internal STAR Note: https://drupal.star.bnl.gov/STAR/starnotes/public/sn0436, (2001).

[81] J. Stevens, “Measurement of the W and Z production Cross Sections at Mid-rapidity in Proton-Proton Collisions at $\sqrt{s}$ = 500 GeV in Run 9.” Internal STAR Note: https://drupal.star.bnl.gov/STAR/starnotes/private/psn0546, (2011).

[82] P.R. Bevington and D.K. Robinson, *Data Reduction and Error Analysis for the Physical Sciences.* McGraw-Hill, 3 ed., (2003).

Brian S. Page

Department of Physics
Center for the Exploration of Energy and Matter
Indiana University
2401 N Milo B. Sampson Lane Bloomington, IN 47408
(812) 855-7881 pagebs@indiana.edu

Education

Ph.D.: Physics, Indiana University, December 2013
Dissertation: Dijet Cross Section and Double Spin Asymmetry at Mid-Rapidity from Polarized p+p Collisions at $\sqrt{s} = 200$ GeV at RHIC
Adviser: Scott Wissink

M.S.: Physics, Indiana University, April 2008

B.S.: Physics and Astronomy, University of Wisconsin, May 2006

Research Experience

Research Assistant: Indiana University Nuclear Physics Group (2007 - Present)
- Leading role in the analysis of forward dijet cross section and double spin asymmetry from polarized proton-proton collisions at $\sqrt{s} = 200$ GeV obtained using the STAR detector at RHIC
- Responsible for the population and monitoring of the STAR CDEV database
- Responsible for offline fill-by-fill spin pattern QA
- Performed initial QA and run list creation for STAR 2009 data set
- Developed and monitored an improved jet algorithm for the STAR L2 trigger system
- Take shifts at STAR as a trained Detector Operator
- Serve as an on-call expert for the Endcap Electromagnetic Calorimeter subsystem

Laboratory Assistant: University of Wisconsin Physics Department (2003 - 2006)
- Leading role in the construction of a new beam line for a ^{8}B beta decay experiment
- Participated in the fabrication of mechanical and electrical components for an ^{14}O beta decay experiment

Conference Presentations

“Di-jet Measurements at Mid and Intermediate Rapidities ($-0.8 < \eta < 1.8$) at the STAR Detector”, APS DNP Fall Meeting (Newport News, VA), October 2013

“STAR ΔG: Results and Prospects”, STAR Analysis Meeting, UCLA, November 2012 (Invited)

“Dijet Measurements at Forward Rapidity Utilizing the Endcap Electromagnetic Calorimeter (EEMC) at the STAR Detector”, APS DNP Fall Meeting (Newport Beach, Ca), October 2012

“The STAR ΔG Program at RHIC”, RHIC/AGS Users Meeting, Brookhaven National Lab, June 2011 (Invited)

“Toward a Dijet Measurement at Forward Rapidity Utilizing the STAR Endcap Electromagnetic Calorimeter”, APS DNP Fall Meeting (Santa Fe, NM), November 2010

“Status of Neutral Dijet Analysis on Data from 200 GeV Proton Proton Collisions Using the STAR Detector at RHIC”, APS April Meeting (Washington, DC), February 2010

“Simulations of Lepton-Hadron Discrimination in pp Collisions at Forward Rapidity with the STAR Detector at RHIC”, APS DNP Fall Meeting (Oakland, CA), October 2008

Teaching Experience

Teaching Assistant: Introductory Physics Lab, Indiana University (Summer 2010)

Graduate Volunteer: Undergraduate Physics Forum (introductory course homework help), Indiana University (2006 - 2008)

Honors and Distinctions

Accepted to the 24th Annual National Nuclear Physics Summer School (Santa Fe, NM 2012)

NSF Fellowship to attend the 58th Annual Lindau Conference of Nobel Laureates (Lindau Germany, 2008)

Technical Skills

Computational:

Proficient: C/C++, ROOT, LaTeX, Tcl, Linux/Unix and Windows OS
Familiar: MySQL, Bash, Python, HTML

Mechanical:

Familiar: Metal Lathe, Milling Machine, General Metal Shop Techniques, Soldering, General Electrical Work